

Fall 2014

A Theoretical Calculation of the Polarization of Scattered Light and a Comparison with AERONET Measurements: Possible Applications to Aerosol Discrimination

Patricio German Piedra
San Jose State University

Follow this and additional works at: https://scholarworks.sjsu.edu/etd_theses

Recommended Citation

Piedra, Patricio German, "A Theoretical Calculation of the Polarization of Scattered Light and a Comparison with AERONET Measurements: Possible Applications to Aerosol Discrimination" (2014). *Master's Theses*. 4510.
DOI: <https://doi.org/10.31979/etd.a4mh-6h2f>
https://scholarworks.sjsu.edu/etd_theses/4510

This Thesis is brought to you for free and open access by the Master's Theses and Graduate Research at SJSU ScholarWorks. It has been accepted for inclusion in Master's Theses by an authorized administrator of SJSU ScholarWorks. For more information, please contact scholarworks@sjsu.edu.

A THEORETICAL CALCULATION OF THE POLARIZATION OF SCATTERED
LIGHT AND A COMPARISON WITH AERONET MEASUREMENTS:
POSSIBLE APPLICATIONS TO AEROSOL DISCRIMINATION

A Thesis

Presented to

The Faculty of the Department of Physics and Astronomy

San José State University

In Partial Fulfillment

of the Requirements for the Degree

Master of Science

by

Patricio G. Piedra

December 2014

© 2014

Patricio G. Piedra

ALL RIGHTS RESERVED

The Designated Thesis Committee Approves the Thesis Titled

A THEORETICAL CALCULATION OF THE POLARIZATION OF SCATTERED
LIGHT AND A COMPARISON WITH AERONET MEASUREMENTS:
POSSIBLE APPLICATIONS TO AEROSOL DISCRIMINATION

by

Patricio G. Piedra

APPROVED FOR THE DEPARTMENT OF PHYSICS AND ASTRONOMY

SAN JOSÉ STATE UNIVERSITY

December 2014

Dr. Patrick Hamill	Department of Physics and Astronomy
Dr. Ramen Bahuguna	Department of Physics and Astronomy
Dr. Kirk Knobelspiesse	NASA Ames Research Center

ABSTRACT

A THEORETICAL CALCULATION OF THE POLARIZATION OF SCATTERED LIGHT AND A COMPARISON WITH AERONET MEASUREMENTS: POSSIBLE APPLICATIONS TO AEROSOL DISCRIMINATION

by Patricio G. Piedra

Despite considerable efforts by many atmospheric scientists, the identification and classification of aerosols remain a big challenge. On the atmospheric scale, large surveys of aerosols rely heavily on light scattering. The degree of linear polarization (DLP) is sensitive to the size and index of refraction of the aerosol particles and may provide an accurate method for discriminating aerosol types. In this thesis, Mie scattering was implemented to yield both the parallel and perpendicular components of the scattered electric field. In a first set of results, the calculated DLP was used to reproduce measurements of DLP along a principal plane for several sites taken by the robotic network of sun-photometers, AERONET. The agreement of theory and experiment is excellent. Having verified this agreement, we calculated the DLP of the particle size distributions from four sites whose aerosols belong to four different types: urban-industrial, biomass, dust and mixed aerosol. The DLP of these types of aerosols was obtained and might constitute a basis for discrimination between aerosols. However, we did not find significant distinctions in the polarization curves of these sites, suggesting it would be difficult to discriminate aerosol types by polarization measurements alone. As a final analysis, we explored the sensitivity of the DLP to changes in the volume concentration distribution and the index of refraction.

DEDICATION

To my four grandparents, Luis, German, America and Olimpia, and to both of my parents, German and Glenda, who have always believed in me. To my lovely wife, Carissa, who has been very helpful through the process of research and writing this thesis. To my motherland, Ecuador and to my adoptive motherland, the U.S.

ACKNOWLEDGEMENTS

Infinite thanks to my research supervisor Dr. Patrick Hamill whose wise and directed mentorship allowed this work to be possible. Thanks to the AERONET network for providing the data necessary to produce the analyses of this thesis.

TABLE OF CONTENTS

CHAPTER

1	INTRODUCTION AND MOTIVATION	1
1.1	Motivation for Aerosol Physical Characterization	1
1.2	Overview of this Thesis	3
2	THEORETICAL BACKGROUND	5
2.1	Mathematical Characterization of Polarization	5
2.1.1	Introduction to the Polarization Amplitude Vector	5
2.1.2	Polarization as a Vector Space	6
2.1.3	Stokes Parameters	7
2.2	Matrix Treatment of Aerosol Light Scattering	8
2.2.1	The Far Scattering Field	10
2.2.2	The Complex Phase Function	11
2.2.3	Mie Scattering	13
2.2.4	Calculation of the Degree of Linear Polarization	17
2.2.5	The Phase Function for Multiple Particles	20
3	IMPLEMENTATION AND RESULTS	22
3.1	Validation: Comparison of Calculation with Previous Results	22
3.2	Obtaining Data of Particle Size Distributions	23
3.3	Curve-fitting the Particle Size Distribution	26
3.4	Polarization: Data versus Theory	27
3.4.1	Definition of a Coincidence and Evaluation of Agreement	28

3.4.2	Beijing, China	37
3.4.3	Djougou, Benin	41
3.4.4	Ras Al-Khaimah, United Arab Emirates	45
3.4.5	Barcelona, Spain	49
3.4.6	Osaka, Japan	53
3.5	Data Analysis of Representative Aerosol Sites	57
3.5.1	Site: Goddard Space Flight Center (GSFC)	58
3.5.2	Site: Solar Village	62
3.5.3	Site: Mongu	66
3.5.4	Site: Beijing	70
3.5.5	All Combined	74
3.6	Sensitivity of the DLP to the PSD and the Index of Refraction	74
3.6.1	Effect on DLP of Changing the Fine Median Radius of the VCD	75
3.6.2	Effect on DLP of Changing the Coarse Mean Radius of VCD .	76
3.6.3	Effect on DLP of Changing the Index of Refraction	76
4	CONCLUSIONS	82
4.1	Final Comment	84
	BIBLIOGRAPHY	85
	APPENDIX	
A	PYTHON SUBROUTINE TO CALCULATE THE DEGREE OF POLAR- IZATION	88
B	PYTHON CODE USED TO IMPLEMENT MIE SCATTERING	90

C	PYTHON SUBROUTINES USED FOR DATA ANALYSIS: “LINPOLTOOLS.PY”	97
D	PYTHON PROGRAM TO FIND AND EVALUATE COINCIDENCES	100

LIST OF FIGURES

Figure

- 2.1 Frame of reference used for spherical EM wave Mie scattering. Here \hat{r}^{inc} is a unit vector along Z , the direction of the incident wave. \hat{E}^{inc} is the incident field. 15

- 3.1 DLP vs. scattering angle published by Hansen and Travis (1974) for a theoretical PSD given by $n(x) = x^6 \exp(\frac{-9x}{x_{eff}})$, the effective size parameter is given by $x_{eff} = 37.5, 150, 600$. Figure reprinted by courtesy of J. Hansen. 24

- 3.2 Reproduction of the results of figure 3.1 for $x_{eff} = 150$. This calculation was performed by Mie scattering routine used for this thesis. The DLP as a function of the phase angle is shown accompanied by its respective PSD given by $n(x) = x^6 \exp(\frac{-9x}{x_{eff}})$ 29

- 3.3 Reproduction of the results of Figure 3.1 for $x_{eff} = 37.5$. This calculation was performed by Mie scattering routine used for this thesis. The DLP as a function of the phase angle is shown accompanied by its respective PSD given by $n(x) = x^6 \exp(\frac{-9x}{x_{eff}})$ 30

- 3.4 Contour figure published by Hansen and Hovenier (1974) for $n = 1.33$ and for values of effective size parameter x_{eff} ranging from 0 – 35, where $x_{eff} = \frac{2\pi R_{eff}}{\lambda}$ is given in terms of an effective radius R_{eff} . The PSD was given by the equation $n(R) = \text{constant} \times R^{17} \exp(\frac{-R}{.05R_{eff}})$. For consistency, in the notation of this thesis $a = R_{eff}$. Reprinted by courtesy of J. Hansen. 31

3.5	Reproduction of contour plot published by Hansen and Hovenier (1974) as shown in figure 3.4. The zero contour has been darkened for clarity. This figure has been calculated by the python code used to implement equation (2.62) in this thesis.	32
3.6	Three dimensional representation of the contour plot of Figure 3.5. .	33
3.7	Comparison of data of VCD taken from AERONET against analytic log-normal curve. This sample VCD was taken from a data set from a photometer located at the Goddard Space Flight Center (GSFC) near Washington DC.	34
3.8	Illustration of the DLP measured by AERONET in the principal plane. The plane contains the zenith, the sun's angle with respect to the zenith and the instrument's position. The sun's position traces an angle α with respect to the zenith. The photometer points at the angle β from the zenith.	35
3.9	The orientation of forward scattering is in the direction of the incoming sunlight. The scattering angle is traced from the direction of forward scattering towards the position of the detector. The scattering angle is given by $\theta = \beta - \alpha $	36
3.10	Coincidence found in Beijing. The date, time and $\chi^2 = 0.003$ values of the coincidence are shown in the figure. The calculated DLP versus the photometer zenith angle is displayed as a solid line. The measurements are shown as small circles. The DLP measurement was taken a few minutes later. The evaluation of χ^2 is done by equation (3.13).	38

3.11	Coincidence found in Beijing. The calculated DLP versus the photometer zenith angle is displayed as a solid line. The measurements are shown as small circles. The agreement is indicated by the value $\chi^2 = 0.006$ displayed on top.	39
3.12	The occurrence of both a measurement of DLP and a combined measurement of index of refraction and PSD within ninety minutes at the same location is defined as a “coincidence.” The DLP is calculated using the index of refraction, solar angle, and PSD. The comparison of theory and measurement yields the χ^2 value described by equation (3.13). Although some anomalous coincidences have values of $\chi^2 > 0.3$, the bulk of the comparisons falls within $0.01 \lesssim \chi^2 \lesssim 0.1$ which are similar to the χ^2 values of Figure 3.10 and Figure 3.11.	40
3.13	Djougou, the predicted DLP is displayed as a solid line. DLP actual measurements which are displayed as small circles were taken within a few minutes of PSD measurement. The evaluation of the agreement is given by its value of $\chi^2 = 0.005$	42
3.14	Coincidence found in Djougou. The date, time, and $\chi^2 = 0.005$ are displayed in the figure.	43
3.15	The χ^2 values of all the coincidences found in AERONET data from Djougou have been evaluated. A large number of coincidences fall within the range $0.001 \lesssim \chi^2 \lesssim 0.01$ which encloses the χ^2 values of Figure 3.13 and Figure 3.14.	44
3.16	AERONET Photometer denoted “Smart” near Dubai. The predicted DLP versus detector zenith angle is shown. The DLP actual measurements were taken within a few minutes.	46

3.17	AERONET Photometer near Dubai. The predicted DLP versus detector zenith angle is shown. The DLP actual measurements were taken within 90 minutes. The χ^2 value is displayed at the top and the agreement is seen to be lower than that of Figure 3.16.	47
3.18	The analysis of all the coincidences found in AERONET data for Ras Al-Khaimah is displayed. Most coincidences are found to have values of $0.001 \lesssim \chi^2 \lesssim 0.008$ which are values similar to those of Figure 3.16. Notice the χ^2 value of Figure 3.17 is 0.012 which does not correspond to the majority. This means that the poor agreement of Figure 3.17 is an anomaly for this particular site.	48
3.19	AERONET Photometer in Barcelona, Spain. The predicted DLP for a given solar zenith angle is shown. The actual measurements of DLP were taken within ninety minutes of PSD. The χ^2 value of this coincidence is displayed on top of the figure.	50
3.20	AERONET Photometer in Barcelona, Spain. The predicted DLP for a given solar zenith angle is shown. The actual measurements of DLP were taken within a few minutes of PSD. The χ^2 value of this coincidence is displayed on top of the figure.	51
3.21	All found coincidences from AERONET data have been evaluated by the χ^2 value given by equation (3.13). The values are displayed as a scatter plot and it is noticeable that the greatest concentration of χ^2 values from this site fall within $0.001 \lesssim \chi^2 \lesssim 0.01$. This range corresponds to the χ^2 values found in Figure 3.19 and Figure 3.20. . .	52

3.22	AERONET Photometer in Osaka, Japan. The predicted DLP for a given sun zenith angle is shown. DLP actual measurements were taken within a few minutes of PSD. The χ^2 displayed on top evaluates the agreement of measurement with calculation.	54
3.23	AERONET Photometer in Osaka, Japan. The predicted DLP for a given solar zenith angle α is shown. DLP actual measurements were taken within a few minutes of PSD. The evaluation of the agreement is stated on top by the figure's χ^2 value.	55
3.24	All found coincidences of data provided by AERONET have been evaluated by the χ^2 value given by equation 3.13. The values have been represented as a scatter plot and it is easy to see that majority of the coincidences fall within $0.001 \lesssim \chi^2 \lesssim 0.008$. This range corresponds to the χ^2 values displayed in Figure 3.22 and Figure 3.23, demonstrating that their agreement is typical and not anomalous.	56
3.25	Top: all PSD's from GSFC whose index of refraction was available were curve-fit using equation (3.11). Each fit yielded a value for χ^2 by the use of equation (3.14). The scatter plot displays the χ^2 value of all the available VCD that were curve-fitted. Bottom: illustration of a VCD from GSFC chosen at random. The AERONET data is shown as a set of 21 circles. The curve-fit is shown as a solid line.	59
3.26	Top: Overview of sixty randomly chosen PSD from GSFC whose index of refraction was known. The $DLP(\theta)$ has been calculated by equation (2.62). Bottom: average $DLP(\theta)$ the sixty calculated from GSFC . . .	60
3.27	Histogram of all the AERONET available index of refraction measurements taken from GSFC between May 1993 and July 2012.	61

3.28	Top: all curve-fitted VCD's from Solar Village have been evaluated by equation (3.14). The χ^2 value of all data set has been plotted and its average value is displayed as a solid line. Sixty of those curve-fits have been selected at random to calculate the DLP of Figure 3.29. Bottom: sample of a VCD from Solar Village curve-fit by equation (3.11). . . .	63
3.29	Top: overview of sixty randomly selected PSD's from Solar Village whose DLP has been calculated. The index of refraction was given in the data set. Bottom: average DLP for all sixty selected PSD. The error bars represent the standard deviation.	64
3.30	Histogram of all the AERONET available index of refraction measurements taken from Solar Village from February 1999 to December 2012.	65
3.31	Top: all the curve-fitted VCD's from Mongu whose index of refraction was given in the data set have been evaluated by equation (3.14). The χ^2 values of this data set have been plotted as a scatter figure and its average value is displayed as a solid line. Bottom: a sample of Mongu's VCD data fitted by equation (3.11).	67
3.32	Top: overview of sixty Monte-Carlo selected PSD whose DLP has been calculated. The index of refraction was given by AERONET. Bottom: average DLP for all sixty selected PSD's. The error bars represent the standard deviation.	68
3.33	Histogram of all the AERONET available index of refraction measurements taken from Mongu from June 1995 to December 2009.	69
3.34	Top: all fitted VCD's from Beijing whose index of refraction was retrieved were evaluated by equation (3.14). The χ^2 value of all data set has been plotted and its average value is displayed as a solid line. Bottom: sample of a Beijing's VCD fitted by equation (3.11).	71

3.35	Top: overview of sixty randomly selected PSD's from Beijing. The index of refraction of each VCD was included in the data and the DLP has been calculated. Bottom: average DLP for all sixty selected VCD's. The error bars represent the standard deviation.	72
3.36	Histogram of all the AERONET available index of refraction measurements taken from Beijing from March 2001 to August 2012.	73
3.37	DLP for all four sites which are considered to be composed of different types of aerosols.	75
3.38	Top: histogram of solar zenith angle for all AERONET polarization measurements taken at Barcelona from December 2004 to April 2014. Bottom: histogram of solar zenith angle for Beijing from April 2002 to March 2014.	77
3.39	Illustration of the distribution of fine and coarse mean radii for the AERONET measured VCD's of Barcelona from 2004 to 2014	78
3.40	Variation in calculated polarization for the fixed parameters: $m = 1.44$, $R_c = 2.46\mu m$ and $\alpha = 65^\circ$. The mean fine mode radius R_f is allowed to change from $0.1\mu m$ to $0.25\mu m$. It is observed that the maximum DLP decreases from 0.8 to 0.4.	79
3.41	Variations in predicted DLP for fixed values of fine mean radius $R_f = 0.18\mu m$, index of refraction $m = 1.44$ and solar angle $\alpha = 65^\circ$. The mean coarse mode radius R_c is changed from $1.5\mu m$ to $3.5\mu m$	80
3.42	DLP for a range of values of index of refraction between $1.3 < m < 1.7$. The mean fine and coarse radii have been fixed to $R_f = 0.18\mu m$ and $R_c = 2.46\mu m$ respectively. It can be seen that the maximum DLP decreases with increasing index of refraction.	81

CHAPTER 1

INTRODUCTION AND MOTIVATION

1.1 Motivation for Aerosol Physical Characterization

An aerosol consists of particles suspended in the air. The suspended particles interact with solar radiation reflecting energy away or absorbing energy into the atmosphere. Distinguishing between different aerosol types in our planet's atmosphere is very important for understanding essential aspects of climate, such as radiation transfer and thermal dynamics, among other important processes.

One of the most important properties of aerosols is their climate forcing effects; that is, the capacity of aerosols to affect atmospheric energy transfer through absorption or reflection of solar radiation. The forcing effects of aerosols in climate dynamics depends on the properties of aerosols and illustrates the importance of aerosol identification as a vital ingredient of global climate studies.

In recent years, a growing number of scientists (ecologists, biologists, atmospheric scientists, environmental engineers, etc.) have become preoccupied about the global effects of the massive amounts of carbon dioxide being transferred to the atmosphere. One of the most worrying aspects of this atmospheric pollution is the effect it may have on global warming (Cox et al., 2000). These concerns have led many notable atmospheric scientists to emphasize the urgency of monitoring the impacts of aerosols on radiative transfer studies. There exist a generalized lack of information about the climate modifications that are due to aerosols (Mishchenko et al., 2004; Hansen et al., 2005). Their concerns have motivated atmospheric studies to identify and classify aerosols in order to understand their optical

properties. A number of scientists have noted that in order to take preventive action, it is urgent to understand the forcing effects of aerosols in the atmosphere (Charlson et al., 1992).

Despite the efforts of many scientists, estimating the effects of aerosols on the energy budget of atmosphere remains one the greatest uncertainties (Anderson et al., 2003). It is very difficult to establish with precision if anthropogenic aerosols are absorbing or reflecting the sun's energy in the atmosphere. A large portion of this difficulty is because accurate methods of aerosol identification that permit a better understanding of aerosol physics are lacking (Anderson et al., 2003; Schwartz and Andreae, 1996). Despite considerable efforts by many atmospheric scientists, accurate aerosol identification remains a significant problem.

Because of the scope of large scale atmospheric surveys, light-scattering detectors, such as lidars or photometers, are the only practical means for such an extensive analysis. For this reason, electromagnetic (EM) wave detectors have become a standard tools for global climate studies.

Several statistical methods for aerosol classification have been considered (Omar et al., 2009; Gobbi et al., 2007; Burton et al., 2012). The method of Hamill et al. (2014) relies on obtaining a set of basic aerosol types. Then, a clustering computation assigns a probability that a measurement is due to a specific type of aerosol. The application of statistical methods allows one to circumvent the complexity of the actual physics of aerosol light scattering, and to focus our attention on parameters of scattering that are simpler to obtain and calculate. One such parameter is the degree of linear polarization (DLP), and the study of the DLP is the subject matter of this thesis.

1.2 Overview of this Thesis

A summary of the structure of this thesis is given as follows. Section 2 introduces a mathematical framework to treat aerosol light scattering as a matrix operation. The matrix that permits such an operation is known as the scattering matrix. In order to carry out a matrix treatment of aerosol scattering, a vector characterization of the state of polarization of an EM wave is developed in Section 2.1 and Section 2.1.3. Then, section 2.2.1 describes how to find the elements of the scattering matrix from the strength of the EM field at a distance far from the particle. In section, 2.2.1, it is shown that the elements of the scattering matrix depend on the distribution of EM amplitude around the scattered particle. Section 2.2.3 focuses on describing the solution to Maxwell's equations for spherical particles. This solution, known as Mie theory, determines the parameters of the scattering matrix by assuming that the aerosol particles are spheres. Section 2.2.4 and section 2.2.5 describe the method for obtaining the degree of linear polarization for a single particle and for a distribution of particles of different radii.

Having developed a method to calculate the degree of linear polarization, we found that two parameters, namely the index of refraction and the particle size distribution, allow us to approximate the horizontal and vertical scattered electric fields using Mie theory. Chapter 3 presents the results of the code used to perform Mie scattering calculations in this thesis, and appendix A displays the code. We present a numerical calculation of the DLP for the two theoretical particle size distributions given by Hansen and Travis (1974) and Hansen and Hovenier (1974). These size distributions assume a fixed index of refraction. Our results are compared with theirs for validation. Then, in Section 3.2, we describe how data for the index of refraction and particle size distribution is obtained from a network of photometers

called AERONET. In Section 3.4, the theoretical analysis of the DLP using Mie theory is compared against actual measurements of DLP. A significant agreement is shown. Having obtained agreement between calculation and measurement, Section 3.5 presents the analysis of DLP of sixty randomly chosen data samples from four sites whose aerosols are consistently composed of urban-industrial, biomass, dust and mixed aerosol. Section 3.6 explores the variation of the DLP by changing the parameters of the index of refraction and particle size distribution one at a time while keeping the remaining parameters fixed. Finally, Section 4 states the conclusions learned from this analysis and presents a final comment regarding the importance of aerosol monitoring in climate studies.

CHAPTER 2

THEORETICAL BACKGROUND

2.1 Mathematical Characterization of Polarization

2.1.1 Introduction to the Polarization Amplitude Vector

The electric components of a plane EM wave traveling in the z direction can be represented mathematically by

$$\tilde{E} = \tilde{E}_0 e^{i(\tilde{k}z - \omega t)}, \quad (2.1)$$

where \tilde{E} is the complex electric field, \tilde{k} is the complex wave number, and ω is the angular frequency. It is convenient to define the amplitude vector \tilde{E}_0 . This quantity is a 2-D vector, that allow us to manipulate in compact form both the phase difference and the amplitude of the wave components. The amplitude vector is defined by

$$\tilde{E}_0 = \begin{pmatrix} E_{0l} e^{i\phi_l} \\ E_{0r} e^{i\phi_r} \end{pmatrix}, \quad (2.2)$$

where the amplitude of each wave component is given by the real electric field amplitude E_{0j} , where $j = l, r$. The phase of E_{0j} is expressed by the phase constant ϕ_j . In this expression, we are adopting the notation of Mischenko et al. (1991), where l and r represent two perpendicular directions in perpendicular to the direction of wave propagation, z .

2.1.2 Polarization as a Vector Space

As summarized by Pedrotti (1993), the states of polarization given by (2.2) can be written in the form

$$\tilde{E}_0 = \begin{bmatrix} E_{0l}(A + iB) \\ E_{0r}(C + iD) \end{bmatrix}, \quad (2.3)$$

where A, B, C and D are real coefficients. Careful analysis of this expression allows one to identify four main states of polarization. Let us consider an electric field amplitude vector such as the one given by equation (2.2), but for convenience, we set $E_{0r} = E_{0l} = K$, where K is a positive constant. Then, the vector amplitude is given by

$$K \begin{bmatrix} e^{i\phi_l} \\ e^{i\phi_r} \end{bmatrix} = K \begin{bmatrix} \alpha + i\beta \\ \gamma + i\delta \end{bmatrix}, \quad (2.4)$$

where $\alpha, \beta, \delta, \gamma$ are real constants. The vector on the right of equation (2.4) can be written as linear combination of four vectors. They are called parallel ϵ_l , perpendicular ϵ_r , right circular ϵ_- , and left circular ϵ_+ . A linear combination of these vectors is sufficient to describe all the states of polarization of an EM wave. In the terminology of linear algebra, these vectors span the polarization space.

Omitting the constant K for clarity, the polarization space unit vectors are given by

$$\epsilon_l = \begin{bmatrix} 1 \\ 0 \end{bmatrix}, \quad \epsilon_r = \begin{bmatrix} 0 \\ 1 \end{bmatrix}, \quad \epsilon_- = \frac{1}{\sqrt{2}} \begin{bmatrix} 1 \\ -i \end{bmatrix}, \quad \epsilon_+ = \frac{1}{\sqrt{2}} \begin{bmatrix} 1 \\ i \end{bmatrix}. \quad (2.5)$$

The dot product $\epsilon_j \cdot \tilde{E}$ yields the component of the electric field in the ϵ_j direction for $j = l, r, -, +$.

In real applications, intensity is measured by averaging many oscillations of the wave. Therefore, the actual value of the phase constant ϕ_j is unnecessary. Instead, the polarization of the amplitude vector (2.2) is determined by the average

time delay of one field component with respect to the other. As a result, the phase difference $\Delta\phi = \phi_r - \phi_l$ becomes more relevant than the actual value ϕ_j . It is convenient to set $\phi_l = 0$, so that $\Delta\phi = \phi_r$.

As described by Jones (1941), this simplification gives rise to the complex amplitude:

$$\tilde{E}_0 = \begin{bmatrix} E_{0l} \\ E_{0r}e^{i\Delta\phi} \end{bmatrix}. \quad (2.6)$$

Equation (2.6) is known as a Jones vector. Note that the state of polarization is defined by only three elements: the amplitudes E_r and E_l and the phase difference $\Delta\phi$.

2.1.3 Stokes Parameters

Stokes parameters are widely used in the scientific community because they allow one to obtain the state of polarization of a beam of light from measurements of its intensity. Stokes defined a set of four parameters that can be easily determined by measuring the intensity of light through various combinations of polarizers. They are commonly known as the Stokes parameters and are defined by

$$I = |\epsilon_l \cdot \tilde{E}|^2 + |\epsilon_r \cdot \tilde{E}|^2 = a_l^2 + a_r^2 \quad (2.7)$$

$$Q = |\epsilon_l \cdot \tilde{E}|^2 - |\epsilon_r \cdot \tilde{E}|^2 = a_l^2 - a_r^2 \quad (2.8)$$

$$U = 2\text{Re}[(\epsilon_l \cdot \tilde{E})^*(\epsilon_r \cdot \tilde{E})] = 2a_la_r\cos\Delta\phi \quad (2.9)$$

$$V = 2\text{Im}[(\epsilon_l \cdot \tilde{E})^*(\epsilon_r \cdot \tilde{E})] = 2a_la_r\sin\Delta\phi, \quad (2.10)$$

where a_l and a_r are positive amplitudes of the electric field.

Although electric field components are difficult to measure, the Stokes parameters allow one to obtain the state of polarization of light experimentally from measurements of intensity.

A more mathematically compact definition of the Stokes parameters can be obtained by defining the coherency vector

$$\vec{J} = \frac{1}{2} \sqrt{\frac{\epsilon}{\mu}} \begin{bmatrix} \tilde{E}_{0l} \tilde{E}_{0l}^* \\ \tilde{E}_{0l} \tilde{E}_{0r}^* \\ \tilde{E}_{0r} \tilde{E}_{0l}^* \\ \tilde{E}_{0r} \tilde{E}_{0r}^* \end{bmatrix}. \quad (2.11)$$

and the tensor

$$T = \begin{bmatrix} 1 & 0 & 0 & 1 \\ 1 & 0 & 0 & -1 \\ 0 & -1 & -1 & 0 \\ 0 & -i & i & 0 \end{bmatrix}. \quad (2.12)$$

Then, the Stokes parameters can be expressed as the four dimensional vector

$$\vec{I} = [I, Q, U, V]^T, \quad (2.13)$$

defined by the matrix multiplication

$$\vec{I} = T \vec{J} = \frac{1}{2} \sqrt{\frac{\epsilon}{\mu}} \begin{bmatrix} \tilde{E}_{0l} \tilde{E}_{0l}^* + \tilde{E}_{0r} \tilde{E}_{0r}^* \\ \tilde{E}_{0l} \tilde{E}_{0l}^* - \tilde{E}_{0r} \tilde{E}_{0r}^* \\ -\tilde{E}_{0l} \tilde{E}_{0r}^* - \tilde{E}_{0r} \tilde{E}_{0l}^* \\ i(\tilde{E}_{0r} \tilde{E}_{0l}^* - \tilde{E}_{0l} \tilde{E}_{0r}^*) \end{bmatrix}. \quad (2.14)$$

2.2 Matrix Treatment of Aerosol Light Scattering

We have presented two ways of expressing the state of polarization of an EM wave. The first is given by equation (2.2) and the second by (2.13). In both cases, we see that the state of polarization corresponds to a vector. This means that EM wave scattering may be represented mathematically by a matrix multiplication. The

transformation matrix of scattering is often referred to as the scattering matrix. If the EM wave is given by (2.1), such a scattering process is found by

$$\tilde{E}^{\text{sca}} = S\tilde{E} = \begin{bmatrix} s_1 & s_2 \\ s_3 & s_4 \end{bmatrix} \begin{bmatrix} \tilde{E}_{0l}^{\text{inc}} \\ \tilde{E}_{0r}^{\text{inc}} \end{bmatrix}, \quad (2.15)$$

where s_1, s_2, s_3 and s_4 are elements of the scattering matrix S , and the superscripts “inc” and “sca” are used to refer to the incident and scattered waves, respectively. Of particular relevance for this thesis is the case of a sphere since aerosol particles will be modeled in this shape. In this case, it can be shown (van de Hulst, 2012) that the scattering matrix simplifies to

$$S = \frac{1}{-ikr} \begin{bmatrix} s_l & 0 \\ 0 & s_r \end{bmatrix}, \quad (2.16)$$

where s_l and s_r are elements of the scattering matrix that will be derived in Section 2.2.3 with the help of Mie theory. The parameter k is the wave number and r is a distance of observation far from the sphere.

The second way to describe scattering is by a matrix multiplication with a Stokes parameters vector. This particular manipulation of polarization vectors of the form given by equation (2.13) is commonly known as Mueller calculus, and the vector \vec{I} is known as a Mueller vector (Bickel and Bailey, 1985). The scattering process is now given by a 4×4 matrix P , which is known as the phase matrix. This means that

$$\vec{I}^{\text{sca}} = P\vec{I}^{\text{inc}}, \quad (2.17)$$

where the vectors \vec{I}^{sca} and \vec{I}^{inc} refer to scattered and incident Mueller vectors, respectively. A straightforward but rather tedious process of substitution allows one to relate the coefficients of the scattering matrix S with those of P . All the relationships have been fully derived by a few authors (van de Hulst, 2012;

Mischenko et al., 1991). However, for the particular case of spherical symmetry, the phase matrix P simplifies significantly and is expressed by

$$P = \frac{1}{k^2 r^2} \begin{bmatrix} \frac{1}{2}(|s_l|^2 + |s_r|^2) & \frac{1}{2}(|s_l|^2 - |s_r|^2) & 0 & 0 \\ \frac{1}{2}(|s_l|^2 - |s_r|^2) & \frac{1}{2}(|s_l|^2 + |s_r|^2) & 0 & 0 \\ 0 & 0 & \frac{1}{2}(s_l s_r^* + s_r s_l^*) & \frac{-i}{2}(s_l s_r^* - s_r s_l^*) \\ 0 & 0 & \frac{i}{2}(s_l s_r^* - s_r s_l^*) & \frac{1}{2}(s_l s_r^* + s_r s_l^*) \end{bmatrix} \quad (2.18)$$

2.2.1 The Far Scattering Field

We now begin the study of the properties of the scattering matrix and the amplitudes s_l and s_r introduced in equation (2.15). However, EM wave-matter interaction is a very complex process. Even though more than a century has passed since Maxwell's equations first appeared, there are still few geometries whose EM scattering fields have been worked out completely. A simplified far-field spherical model of aerosol scattering has been applied in this thesis.¹

Let us begin by assuming a plane EM wave \tilde{E}_0 traveling in an arbitrary incident direction \hat{r}^{inc} . The representation of such wave is given by equation (2.1) as:

$$\tilde{E}^{\text{inc}} = \tilde{E}_0^{\text{inc}} e^{i(\vec{k}r^{\text{inc}} - \omega t)}. \quad (2.19)$$

If such a wave scatters from an aerosol particle, it induces an oscillating dipole that produces an EM wave of its own. The dipole-generated EM disturbance propagates in all directions as a spherical wave. The behavior of the EM field near the aerosol is complicated. However in the limit where the distance to the particle is much

¹ A vast amount of literature exists in the subject of EM wave scattering. A complete examination of the subject is far beyond the scope of this thesis. For a review of general EM wave scattering, the reader is referred to Jackson (1998). For a more advanced level of applied EM wave scattering the reader is referred to Mischenko et al. (1991).

larger than the wavelength, that is $r \gg \lambda$, the scattered spherical wave once again can be treated as a plane EM wave. Since in terms of intensity, $I^{scat} \propto |E|^2$, and at a distance r far from the scattering point, the distribution of $I^{scat} \propto \frac{1}{r^2}$, we expect the amplitude of such wave to be $|E| \propto \frac{1}{r}$. Furthermore, we expect as usual that the spatial variation of the propagating wave acquires the plane wave factor $|E| \propto e^{ikr}$. The mathematical proof has been worked out by several authors, for example Mischenko et al. (1991) and van de Hulst (2012). The amplitude \tilde{E} of the scattered electric field at a point \vec{r} far from the particle obeys the Fresnel-Huygens relations:

$$\tilde{E}(\vec{r}) = \frac{e^{ikr}}{-ikr} s(\theta, \phi) \tilde{E}_0^{\text{inc}}, \quad (2.20)$$

$$\hat{r} \cdot \tilde{E}(\vec{r}) = 0 \quad (2.21)$$

Equation (2.21) simply tells us that there is not an EM wave component in the \hat{r} direction. The factor $s(\theta, \phi)$ in equation (2.20) introduces a dependence on the angular distribution of amplitude around the particle; this factor is known as the complex phase function (CPF).² The factor $\frac{1}{-ik}$ has been introduced artificially for future convenience. The quantity $\frac{1}{-i} = i$ is helpful in calculations that appear often in matrix scattering of type $|\tilde{E}|^2 = E E^*$, while the factor $\frac{1}{k}$ allows the CPF to be a unitless quantity.

2.2.2 The Complex Phase Function

The equation for far-field EM wave scattering (2.20) introduced the complex phase function (CPF) which is represented by the symbol $s(\theta, \phi)$. The physical interpretation of this term might not be very intuitive in terms of amplitude, but its

² There is lack of convention about the definition of the “phase function.” Some authors refer to the distribution of intensity I^{scat} around the scattered particle as the “phase function” while others call the distribution of amplitude $|\tilde{E}|$ around the scattered particle the “phase function.” In this thesis, the term “phase function” refers to the former, and “complex phase function” refers to the latter case.

square $|s(\theta, \phi)|^2$ can be interpreted as the distribution of scattered intensity at a location r which is far from the particle in the direction θ, ϕ . Here, we assume that the origin is centered inside the particle, and θ and ϕ are the polar and azimuthal angles respectively. As you might imagine, the distribution of energy scattered from the aerosol in a particular direction depends on the characteristics of the particle such as its geometry, index of refraction, size relative to the wavelength, etc.

Accurate determination of the CPF for realistic aerosols, which are likely to be non-spherical, is a difficult obstacle for EM wave polarization calculations. There are very few geometries for which analytical solutions to the Maxwell equations have been found. Among them, there are spheres, cylinders and discs (Gillespie, 1992; Mishchenko and Travis, 1994). By far, the most widely used geometry in atmospheric studies is that of spheres since aerosol particles are often assumed to have this shape. An assumption commonly made is that the orientation of non-spherical aerosols in the atmosphere is random in all directions. The net effect of this randomness is that the tiny discrepancies of the scattered distribution of energy in all directions “averages out” so that the overall phase function resembles that of a collection of spheres. The net effect of this assumption is that the theory of scattering by spheres can be used as a first order approximation (Bohren and Huffman, 2008). The validity of this assumption has yielded some positive results experimentally (West et al., 1997) although there exist few experimental studies that also incorporate polarization. It is expected that as more scientists become stimulated to work with polarization, there will be more experimental work in this particular area.

2.2.3 Mie Scattering

Mie scattering refers to a solution of the Maxwell equations for a sphere which is attributed to Gustav Mie. This solution is applicable to aerosol scattering calculations since one normally approximates the CPF of aerosol-scattered light as that of a collection of spheres.

The scattered EM field has spherical symmetry independent of the initial direction of the incident wave. A careful choice of coordinate system allows one a significant simplification to the solution of the wave equation. In particular, the solution is expressed conveniently in a frame of reference where the incident wave direction \hat{r}^{inc} is aligned with the Z axis of a Cartesian frame of reference X, Y, Z with origin at the center of the sphere (see Figure 2.1).

For time dependent fields, such as an EM wave propagating in a linear, isotropic and homogeneous medium, equation (2.1) and its magnetic analog can be expressed by

$$\tilde{E} = \tilde{E}_0 e^{i(\vec{k}r - \omega t)}, \quad (2.22)$$

$$\tilde{H} = \tilde{H}_0 e^{i(\vec{k}r - \omega t)}. \quad (2.23)$$

It can be shown (Bohren and Huffman, 2008) that these two expressions obey the Helmholtz-wave equation:

$$\nabla^2 \tilde{E} + k^2 \tilde{E} = 0, \quad (2.24)$$

$$\nabla^2 \tilde{H} + k^2 \tilde{H} = 0, \quad (2.25)$$

where $k^2 = \omega^2 \epsilon \mu$. The quantity ϵ is the electric permittivity of the medium and μ its permeability. Equation (2.24) and (2.25) are easily obtained from Maxwell's equations for non-divergent fields:

$$\nabla \cdot \tilde{E} = 0, \quad (2.26)$$

$$\nabla \cdot \tilde{H} = 0, \quad (2.27)$$

$$\nabla \times \tilde{E} = i\omega\mu\tilde{H}, \quad (2.28)$$

$$\nabla \times \tilde{H} = -i\omega\epsilon\tilde{E}. \quad (2.29)$$

The first appearance of a complete analytic solution for a spherical geometry satisfying the conditions (2.24) to (2.29) is attributed to Gustav Mie. Today, the theory is known as Mie scattering theory.

In order to find the Mie scattering solution, we must first derive the scalar wave equation. For this reason, let us introduce a vector field \tilde{M} satisfying the conditions

$$\tilde{M} = \nabla \times (\vec{r}V) \quad (2.30)$$

$$\nabla \cdot \tilde{M} = 0, \quad (2.31)$$

where V is a scalar function. In addition, if the vector identities

$$\nabla \times (A \times B) = A(\nabla \cdot B) - B(\nabla \cdot A) + (B \cdot \nabla)A - (A \cdot \nabla)B, \quad (2.32)$$

and

$$\nabla(A \cdot B) = A \times (\nabla \times B) + B \times (\nabla \times A) + (B \cdot \nabla)A + (A \cdot \nabla)B, \quad (2.33)$$

are used, it is found that the field \tilde{M} satisfies the wave equation

$$\nabla^2 \tilde{M} + k^2 \tilde{M} = \nabla \times [\vec{r}(\nabla^2 V + k^2 V)]. \quad (2.34)$$

This means that the vector field \tilde{M} would comply with the condition of the wave equations (2.24) and (2.25) if

$$\nabla^2 V + k^2 V = 0. \quad (2.35)$$

Equation (2.35) is known as the scalar wave equation. The solution to the scalar wave equation for the particular geometry of a sphere is found by the the

separation of variables technique in which one assumes that

$$V(r, \theta, \phi) = R(r)\Theta(\theta)\Phi(\phi). \quad (2.36)$$

The process of solving equation (2.35) for the boundary conditions inside and

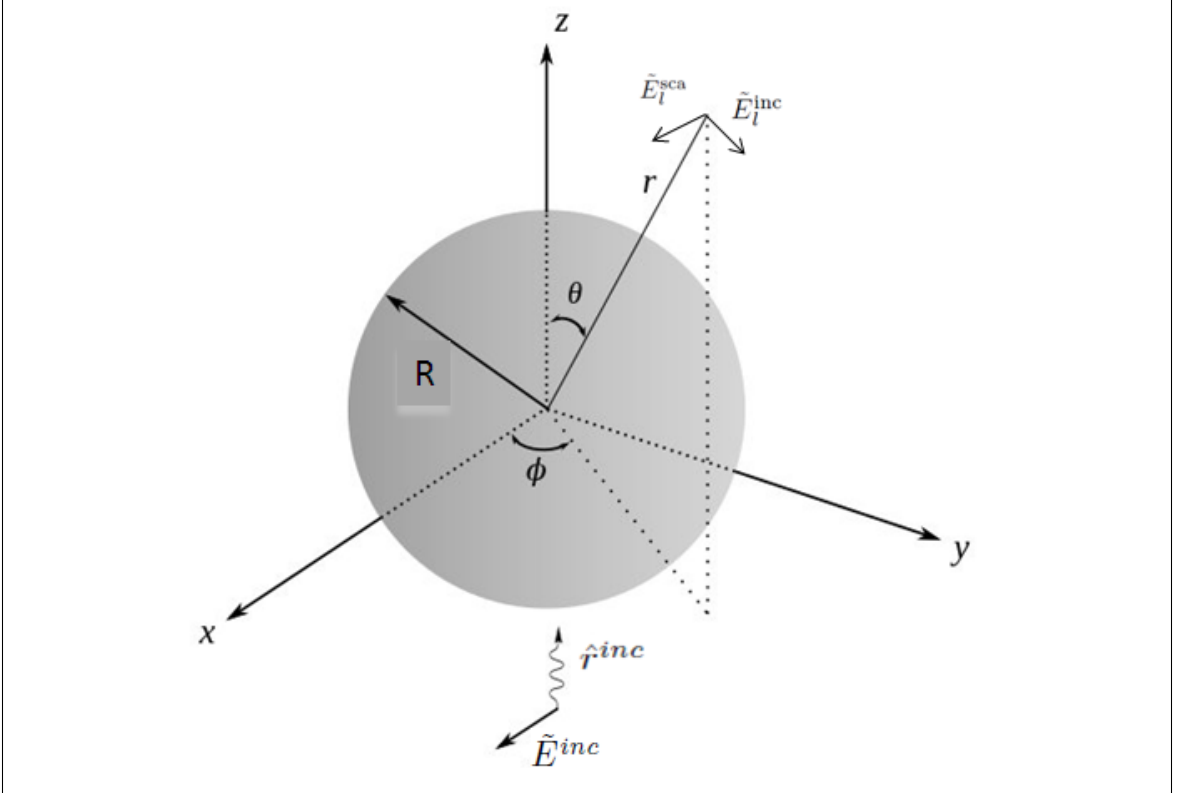


Figure 2.1: Frame of reference used for spherical EM wave Mie scattering. Here \hat{r}^{inc} is a unit vector along Z , the direction of the incident wave. \hat{E}^{inc} is the incident field.

outside the sphere requires a cumbersome amount of mathematics. In particular, it requires an expansion of the incoming plane wave as an infinite sum of spherical harmonics and the use of boundary conditions to find the coefficients of the sum. Nonetheless, the mathematics have been worked out by several authors (Bohren and Huffman, 2008; Jackson, 1998). In this thesis, the notation of van de Hulst (2012) is followed. After solving the scalar wave equation for a sphere, it is found that the field components \tilde{E}_l and \tilde{E}_r of the scattered field can be related to the incident

fields \tilde{E}_l^{inc} and \tilde{E}_r^{inc} by the scattering matrix described in equation (2.16). The matrix equation given by equation (2.15) is described by

$$\tilde{E}_l(\theta, \phi) = s_l(\theta) \frac{e^{ikr}}{-ikr} \tilde{E}_l^{\text{inc}} \quad (2.37)$$

$$\tilde{E}_r(\theta, \phi) = s_r(\theta) \frac{e^{ikr}}{-ikr} \tilde{E}_r^{\text{inc}}, \quad (2.38)$$

where

$$s_l(\theta) = \sum_{n=1}^{\infty} \frac{2n+1}{n(n+1)} [a_n \pi_n + b_n \tau_n] \quad (2.39)$$

$$s_r(\theta) = \sum_{n=1}^{\infty} \frac{2n+1}{n(n+1)} [b_n \pi_n + a_n \tau_n] \quad (2.40)$$

in which

$$\pi_n = \frac{1}{\sin(\theta)} P_n[\cos(\theta)] \quad (2.41)$$

$$\tau_n = \frac{d}{d\theta} P_n[\cos(\theta)]. \quad (2.42)$$

The quantities a_n and b_n are given by

$$a_n = \frac{\psi'_n(mx) \psi_n(x) - m \psi_n(mx) \psi'_n(x)}{m \psi'_n(mx) \zeta_n(x) - m \psi_n(mx) \zeta'_n(x)} \quad (2.43)$$

$$b_n = \frac{m \psi'_n(mx) \psi_n(x) - \psi_n(mx) \psi'_n(x)}{m \psi'_n(mx) \zeta_n(x) - \psi_n(mx) \zeta'_n(x)} \quad (2.44)$$

In equations (2.41) and (2.42), $P_n[\cos(\theta)]$ is the Legendre polynomial of order n . In equations (2.43) and (2.44), m is the complex index of refraction. The quantity x is the relative size of the particle's circumference ($2\pi R$) with respect to the wavelength λ , where R is the particle's radius. This quantity is commonly known as the “size parameter” defined by

$$x \equiv \frac{2\pi R}{\lambda}. \quad (2.45)$$

The quantities $\psi_n(q)$ and $\zeta_n(q)$ are related to the spherical Bessel functions $J_n(q)$ and $H_n(q)$ of the first and second kind, respectively. For some variable q , they are defined by

$$\psi_n(q) = \left(\frac{\pi q}{2}\right)^{1/2} J_{n+\frac{1}{2}}(q), \quad (2.46)$$

$$\zeta_n(q) = \left(\frac{\pi q}{2}\right)^{1/2} H_{n+\frac{1}{2}}(q). \quad (2.47)$$

Though it is difficult to intuitively appreciate the consequences of these complex equations, a major conclusion can be reached from them. As shown from equation (2.39) and (2.40), the CPF for some EM scattering event at a location r which is far from a spherical particle is independent of ϕ if a convenient reference frame is chosen where the incident direction \hat{r}^{inc} is aligned with \hat{z} . Moreover, equations (2.43) and (2.44) show that the CPF depends on the size parameter x and the index of refraction m . In conclusion, this means $s_j(\theta, \phi) = s_j(x, m, \theta)$ for $j = l, r$.

2.2.4 Calculation of the Degree of Linear Polarization

We now show how to apply Mie theory to calculate the degree of linear polarization (DLP) for a single particle. The following convention is used in this section and the next: for a single particle, the lower case dlp , s_l and s_r are used to express the degree of linear polarization and the complex phase functions. The upper case DLP , S_l and S_r are reserved for the degree of linear polarization and complex phase functions that have been integrated with respect to a distribution of particles.

As shown in the previous section, the parallel and perpendicular components of the scattered electric fields are related to the incident fields by equations (2.37)

and (2.38). Written in matrix notation, these two equations are expressed by

$$\tilde{E}(m, x, \theta) = \frac{1}{-ikr} \begin{bmatrix} s_l(m, x, \theta) & 0 \\ 0 & s_r(m, x, \theta) \end{bmatrix} \begin{bmatrix} E_{0l}e^{i\phi_l} \\ E_{0r}e^{i\phi_r} \end{bmatrix} e^{i(\tilde{k}r - \omega t)}. \quad (2.48)$$

To determine the Stokes parameters, we use the phase matrix P defined by equation (2.18), which can be written as

$$\begin{bmatrix} I^{sca} \\ Q^{sca} \\ U^{sca} \\ V^{sca} \end{bmatrix} = \frac{1}{k^2 r^2} \begin{bmatrix} p_{11}(m, x, \theta) & p_{12}(m, x, \theta) & 0 & 0 \\ p_{12}(m, x, \theta) & p_{11}(m, x, \theta) & 0 & 0 \\ 0 & 0 & p_{33}(m, x, \theta) & p_{34}(m, x, \theta) \\ 0 & 0 & -p_{34}(m, x, \theta) & p_{33}(m, x, \theta) \end{bmatrix} \begin{bmatrix} I^{inc} \\ Q^{inc} \\ U^{inc} \\ V^{inc} \end{bmatrix}. \quad (2.49)$$

In the previous equation (2.49), the components $p_{nj}(m, x, \theta)$ for $n = j = 1, 2, 3, 4$ are quadratic combinations of the CPF $s_l(m, x, \theta)$ and $s_r(m, x, \theta)$. They are derived from the expansion of scattering 2×2 matrices into Mueller 4×4 matrices. The components $p_{nj}(m, x, \theta)$ are listed next omitting the dependency of (m, x, θ) for clarity.

$$p_{11} = \frac{1}{2}(|s_r|^2 + |s_l|^2), \quad (2.50)$$

$$p_{12} = \frac{1}{2}(|s_r|^2 - |s_l|^2), \quad (2.51)$$

$$p_{33} = \frac{1}{2}(s_r^* s_l + s_r s_l^*), \quad (2.52)$$

$$p_{34} = \frac{i}{2}(s_l s_r^* - s_r s_l^*). \quad (2.53)$$

Now, recall that any beam of light can be represented by its Stokes parameters as a vector of the form

$$\vec{I} = [I, Q, U, V]^T. \quad (2.54)$$

The definition of the DLP is the negative ratio of the polarized intensity component Q over the total intensity I . Therefore, for a scattered beam of EM radiation, the

DLP can be calculated by the ratio

$$dlp = -\frac{Q^{sca}}{I^{sca}}. \quad (2.55)$$

Now, the mathematical representation of unpolarized light is given by

$$\vec{I}^{inc} = I_0 \begin{bmatrix} 1 \\ 0 \\ 0 \\ 0 \end{bmatrix}. \quad (2.56)$$

The product of the phase matrix of equation (2.49) with the unpolarized incident vector given by (2.56) yields the simple expression for the scattered Mueller vector given by

$$\vec{I}^{sca} = I_0 \begin{bmatrix} p_{11}(m, x, \theta) \\ p_{12}(m, x, \theta) \\ 0 \\ 0 \end{bmatrix}. \quad (2.57)$$

Therefore, the degree of linear polarization $dlp(m, x, \theta)$ for the scattered light is the ratio

$$dlp(m, x, \theta) = -\frac{p_{12}(m, x, \theta)}{p_{11}(m, x, \theta)}. \quad (2.58)$$

Substituting (2.50) and (2.51) into (2.58), we obtain

$$dlp(m, x, \theta) = -\frac{|s_r|^2 - |s_l|^2}{|s_r|^2 + |s_l|^2}. \quad (2.59)$$

Equation (2.59) is an important relation and constitutes the fundamental equation to calculate the DLP from the angular distribution of relative intensity given by the complex phase functions s_r and s_l .

2.2.5 The Phase Function for Multiple Particles

When considering scattering with more than one particle, the actual physics of such a process is extremely complicated. Intuitively, we can expect the scattered light to undergo multiple scattering events with different particles before it reaches the observer. Nonetheless, theoretical studies conducted by Hansen and Hovenier (1974), Hansen and Travis (1974), and more recently Tomasko and Smith (1982) demonstrated that models based on single scattering could be used as a first order approximation. If more accuracy is needed, more complex multiple scattering models can be used.³

When considering single scattering, an assumption is made that most of the photons that reach the observer undergo only one scattering event. The mathematical effect of this assumption in the total phase functions $|S_l(\theta)|^2$ and $|S_r(\theta)|^2$ is that they can be approximated as a sum of the phase functions of each individual spherical particles. This means that the single particle phase function can be integrated over a number density $n(x)dx$; that is, the number of particles per unit volume of air with size parameter between x and $x + dx$. In mathematical terms this means:

$$|S_l(m, \theta)|^2 = \int_{x_1}^{x_2} |s_l(m, x, \theta)|^2 n(x) dx \quad (2.60)$$

$$|S_r(m, \theta)|^2 = \int_{x_1}^{x_2} |s_r(m, x, \theta)|^2 n(x) dx. \quad (2.61)$$

Note that the integrated phase functions are no longer a function of x since this dependency has been integrated out. As a result, the integrated DLP for a particle size distribution (PSD) is now a function of the scattering angle θ and the index of

³ Several methods of multiple scattering have been developed. An excellent overview of the so-called doubling method is available in the article by Hansen (1971).

refraction m and can be expressed by

$$DLP(m, \theta) = -\frac{|S_r(m, \theta)|^2 - |S_l(m, \theta)|^2}{|S_r(m, \theta)|^2 + |S_l(m, \theta)|^2}. \quad (2.62)$$

The relative simplicity of equation (2.62) to calculate the DLP of the atmosphere makes it an attractive parameter for attempting to discriminate between different types of aerosols.

CHAPTER 3

IMPLEMENTATION AND RESULTS

The implementation of equation (2.62) to find the DLP for a particle size distribution (PSD) was done using a translation of the FORTRAN Mie scattering code published by Bohren and Huffman (2008). A python version of this code was developed by Kaiser (2012) and is available as a free download at <http://code.google.com/p/scatterlib/>.

3.1 Validation: Comparison of Calculation with Previous Results

In order to validate the code, we compared results against some of the work of Hansen and Hovenier (1974) and Hansen and Travis (1974) that were successful in planetary atmosphere analysis. As a start, the Mie scattering code solving equation (2.62) numerically was successful in reproducing some of the results of Hansen and Travis (1974). In this case, the index of refraction was fixed at $m = 1.33$, and a theoretical PSD was assumed. The distribution used by Hansen and Travis (1974) is described by

$$n(x) = x^6 \exp\left(\frac{-9x}{x_{eff}}\right), \quad (3.1)$$

where x_{eff} is the effective size parameter which can be set fixed. Using various values of x_{eff} they generated the curves shown in Figure 3.1. Note that the bottom two curves are for $x_{eff} = 37.5$ and $x_{eff} = 150$. For comparison, Figure 3.2 and Figure 3.3 were obtained using our code for $x_{eff} = 150$ and $x_{eff} = 37.5$ respectively. As the reader can easily notice, the main characteristics of this plots such as the peaks and valleys are accurate in both position and magnitude of polarization.

In a similar fashion, the code developed for this thesis was able to reproduce the results of Hansen and Hovenier (1974). Similarly to the previous case, a theoretical distribution has been assumed. In this case, the particle size distribution is a function of the particle radius R and a fixable effective radius R_{eff} . The parameter R_{eff} and the effective size parameter x_{eff} are related by a relationship similar to (2.45),

$$x_{eff} = \frac{2\pi R_{eff}}{\lambda}. \quad (3.2)$$

A size distribution chosen by Hansen and Hovenier (1974) for the clouds of Venus can be expressed by the equation

$$n(R) = \text{constant} \times R^{17} \exp\left(\frac{-R}{0.05R_{eff}}\right). \quad (3.3)$$

By varying the effective size parameter from 0 to 35, they obtained the contour figure of DLP shown in Figure 3.4. We used the same PSD keeping the index of refraction fixed at $m = 1.33$ and determined the DLP as a function of the scattering angle. Our results are presented in Figure 3.5. The same results are presented as a 3-D surface in Figure 3.6. The reader is invited to compare Figure 3.4 with 3.5 and notice the location of the prominent contours including the zero contour which has been highlighted for clarity in Figure 3.5. It is easy to verify that in both cases, the calculations we performed matched those of Hansen and Travis (1974) and Hansen and Hovenier (1974). These results gave us confidence that our code would be valid for implementation of polarization calculations for aerosol size distributions obtained by measurements in Earth's atmosphere.

3.2 Obtaining Data of Particle Size Distributions

In section 2.2.4, it was shown that the index of refraction and the size distribution were required to calculate the degree of polarization using Mie

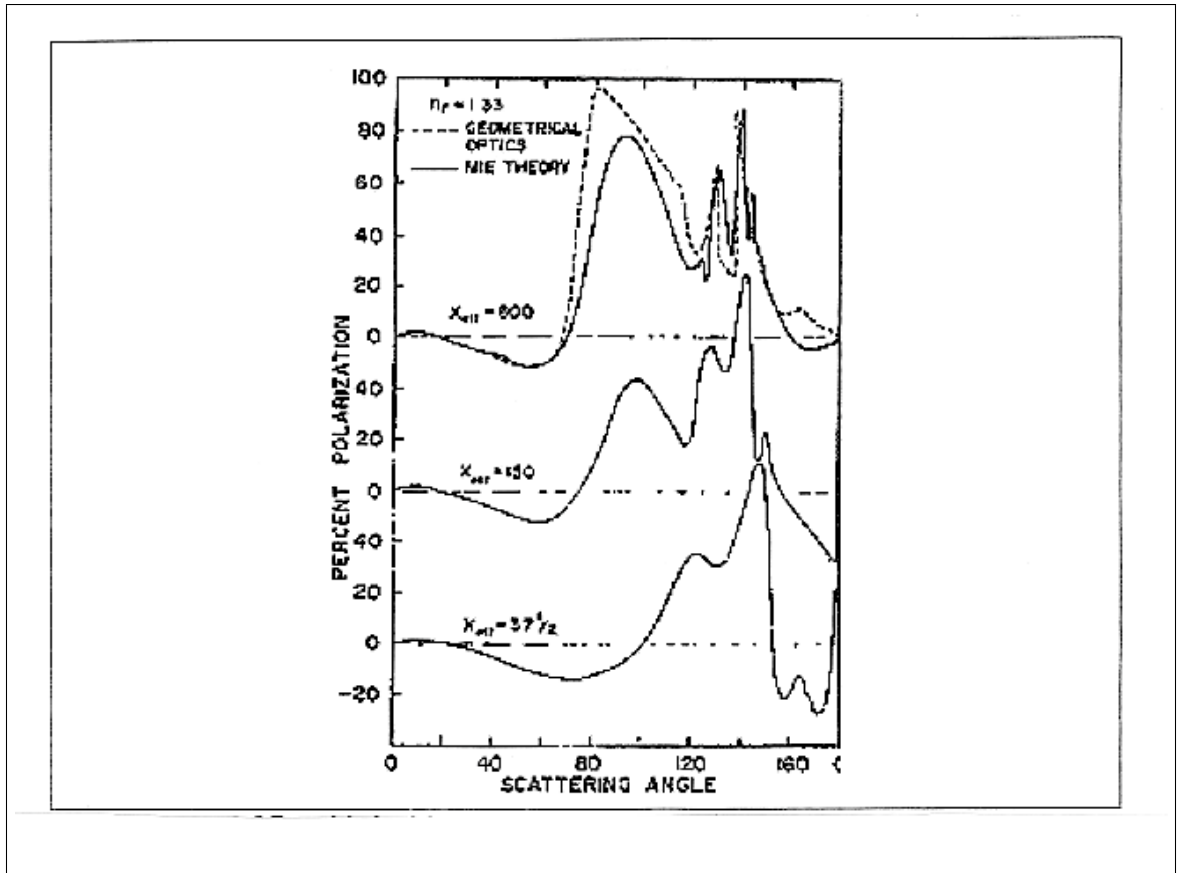


Figure 3.1: DLP vs. scattering angle published by Hansen and Travis (1974) for a theoretical PSD given by $n(x) = x^6 \exp(\frac{-9x}{x_{eff}})$, the effective size parameter is given by $x_{eff} = 37.5, 150, 600$. Figure reprinted by courtesy of J. Hansen.

scattering as an approximation. The index of refraction and the PSD are obtained from the Aerosol Robotic Network (AERONET) (Holben et al., 1998). This network of photometers obtains retrievals of size distributions and complex index of refraction by passive surveys of the sky. The data from hundreds of photometers worldwide are available for download at <http://aeronet.gsfc.nasa.gov/>.

One of the parameters reported by AERONET is the logarithmic volume concentration distribution (VCD). The VCD, defined by $\frac{dV}{d \ln R}$, represents the total volume per unit volume of air occupied by particles having a logarithmic radius R between $\ln R$ and $\ln R + d(\ln R)$. This quantity allows one to infer the particle size

distribution (PSD) by the simple fact that the total volume dV occupied by dN particles having volumes given by $v(R)$ are related by the expression

$$dV = v(R)dN. \quad (3.4)$$

The inverted VCD's in the AERONET data set are presented as a set of 21 logarithmically equidistant volume concentrations measurements for radii $R = 0.5 \mu m$ to $R = 15 \mu m$. The inversion process assumes a bimodal VCD, and it is obtained by an algorithm described by Dubovik and King (2000). The units of VCD are $\mu m^3/\mu m^2$, and the relationship between the VCD and the PSD is given by¹

$$\frac{dV}{d \ln R} = v(R) \frac{dN}{d \ln R}, \quad (3.5)$$

where $v(R)$ is the volume of a particle of radius R , and $\frac{dN}{d \ln R}$ is the logarithmic particle size distribution. Now, using the identity $d(\ln R) = \frac{1}{R}dR$ in (3.5), the result is

$$\frac{dV}{d \ln R} = Rv(R) \frac{dN}{dR} \quad (3.6)$$

Finally, solving for $\frac{dN}{dR} = n(R)$ and substituting $v(R) = \frac{4}{3}\pi R^3$, we obtain the desired PSD given by

$$n(R) = \frac{3}{4\pi R^4} \frac{dV}{d \ln R}. \quad (3.7)$$

Using the radius R as the variable of the particle size distribution, equations (2.60) and (2.61) can be expressed as

$$|S_j(\theta)|^2 = \int_{R_1}^{R_2} |s_j(m, \frac{2\pi R}{\lambda}, \theta)|^2 n(R) dR. \quad (3.8)$$

Therefore, if the index of refraction of a particular VCD is known, the PSD given by (3.7) can be used to calculate the phase functions $|S_l(\theta)|^2$ and $|S_r(\theta)|^2$ using equations (2.60) and (2.61) respectively. This implementation allows us to determine the DLP given by equation (2.62).

¹ An excellent discussion of the PSD has been written by Zender (2008).

3.3 Curve-fitting the Particle Size Distribution

This section describes the process of curve fitting the volume concentration distribution obtained from AERONET to an analytic function. AERONET measurements of VCD are given in a set of twenty one logarithmically equidistant particle radii. Since the calculation of the DLP described in section 2.2.5 requires numerical integration, it is convenient to fit the discrete AERONET data to a smooth curve. The analytic volume concentration distribution can then be easily converted into a particle size distribution by applying equation (3.7).

Fitting the VCD of a bi-modal distribution to an analytic expression is a problem that has already been explored (Dallavalle et al., 1951). The two modes of the bi-modal VCD are known as the fine and coarse mode. Each log-normal VCD can be fit by the log-normal relationships

$$\frac{dV_f}{d \ln R} = \frac{V_f}{\sqrt{2\pi}\sigma_f} \exp \left[-\frac{(\ln R - \ln \bar{R}_f)^2}{2(\sigma_f)^2} \right] \quad (3.9)$$

and

$$\frac{dV_c}{d \ln R} = \frac{V_c}{\sqrt{2\pi}\sigma_c} \exp \left[-\frac{(\ln R - \ln \bar{R}_c)^2}{2(\sigma_c)^2} \right], \quad (3.10)$$

where V_f and V_c represent the total volume concentration of each mode. Similarly, σ_f and σ_c correspond to the standard deviation of each mode, and \bar{R}_f and \bar{R}_c are their respective mean radii.

Finally, the total logarithmic VCD is obtained from adding (3.9) with (3.10); this means that

$$\frac{dV}{d \ln R} = \frac{dV_f}{d \ln R} + \frac{dV_c}{d \ln R}. \quad (3.11)$$

As an illustration, Figure 3.7 presents the VCD data set from AERONET (a set of twenty one logarithmically spaced points) and a theoretical VCD fit by equation (3.11).

3.4 Polarization: Data versus Theory

Some AERONET photometers are equipped to take measurements of the polarization of light scattered by aerosols. It is possible to approximate that polarization using Mie scattering theory and the application of equation (3.8) for a given particle size distribution. The level of agreement of the Mie scattering calculation of DLP with actual measurements of DLP will validate our application of Mie theory. The AERONET DLP measurements are taken by scanning in a plane containing the sun's position, the zenith and the photometer. An upward directed arc in this plane is tracked by the photometer. The photometer takes measurements of DLP from -85 to 85 degrees with steps of 5 degrees and with the origin defined by the zenith. The positive angular direction is defined by the direction of the solar zenith angle α (see Figure 3.8) so that the sun's zenith angle is always positive. An illustration of this relationship is shown in Figure 3.9. The Mie scattering angle, that is, the angle between the direction of forward scattering and the detector, is given by

$$\theta = |\beta - \alpha|. \quad (3.12)$$

The implementation of equation (3.8) for a given PSD at a particular date and time can be compared against actual DLP measurements. The measurements were taken at a given solar zenith angle.

3.4.1 Definition of a Coincidence and Evaluation of Agreement

In order to evaluate the agreement of theory and experiment, the concept of a coincidence must be introduced. In this thesis, the term "coincidence" refers to the occurrence of a direct measurement of the DLP within 90 minutes of an AERONET measurement for which the index of refraction and size distribution have been

inverted. This allows us to calculate the DLP at that location and time.

We now consider the agreement of theory and experiment. We evaluate the value of χ^2 defined by

$$\chi^2 = \frac{1}{n-1} \sum_i^n [DLP(\beta_i)^{\text{measured}} - DLP(\beta_i)^{\text{calculated}}]^2, \quad (3.13)$$

where β_i stands for the angle of the measurement taken by the photometer. The quantity n represents the total number of angular measurements, in this case $n = 35$.

In what follows, we present comparisons of theoretical DLP calculations and polarization measurements for various AERONET sites, specifically Beijing (China), Djougou (Benin), Ras Al-Khaimah (UAE), Barcelona (Spain), and Osaka (Japan). We have carried out numerous calculations for each of these locations and present here a small sample of the curves generated.

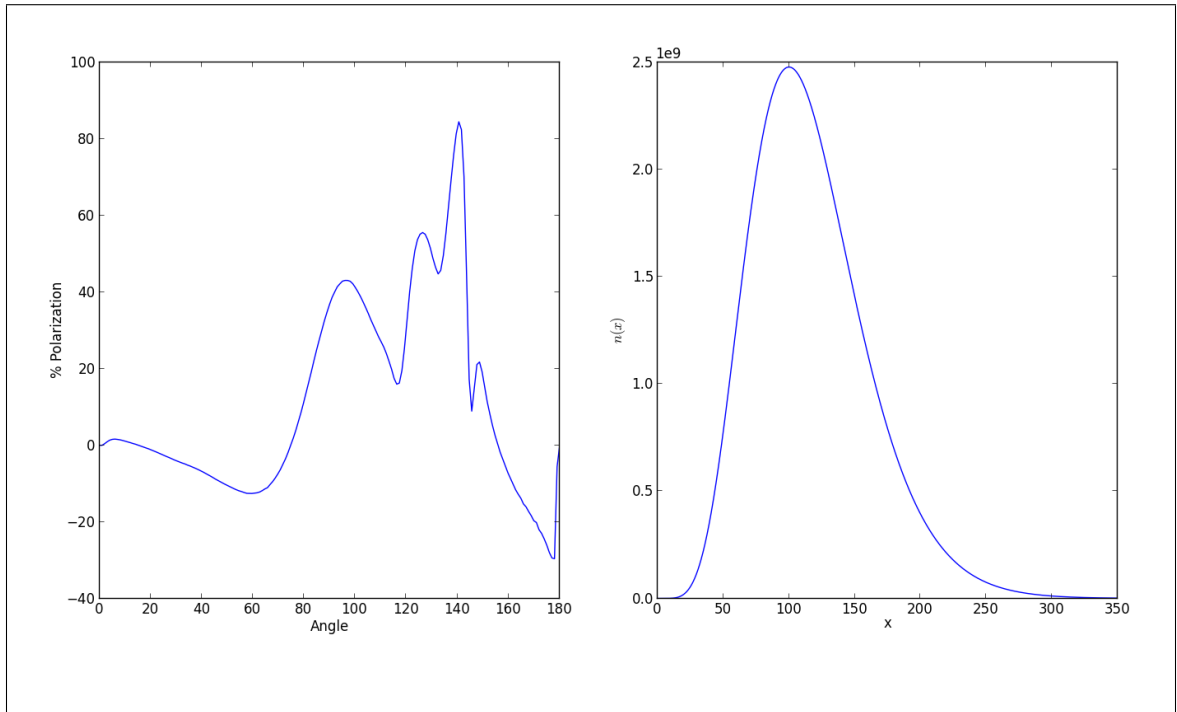


Figure 3.2: Reproduction of the results of figure 3.1 for $x_{eff} = 150$. This calculation was performed by Mie scattering routine used for this thesis. The DLP as a function of the phase angle is shown accompanied by its respective PSD given by $n(x) = x^6 \exp(\frac{-9x}{x_{eff}})$.

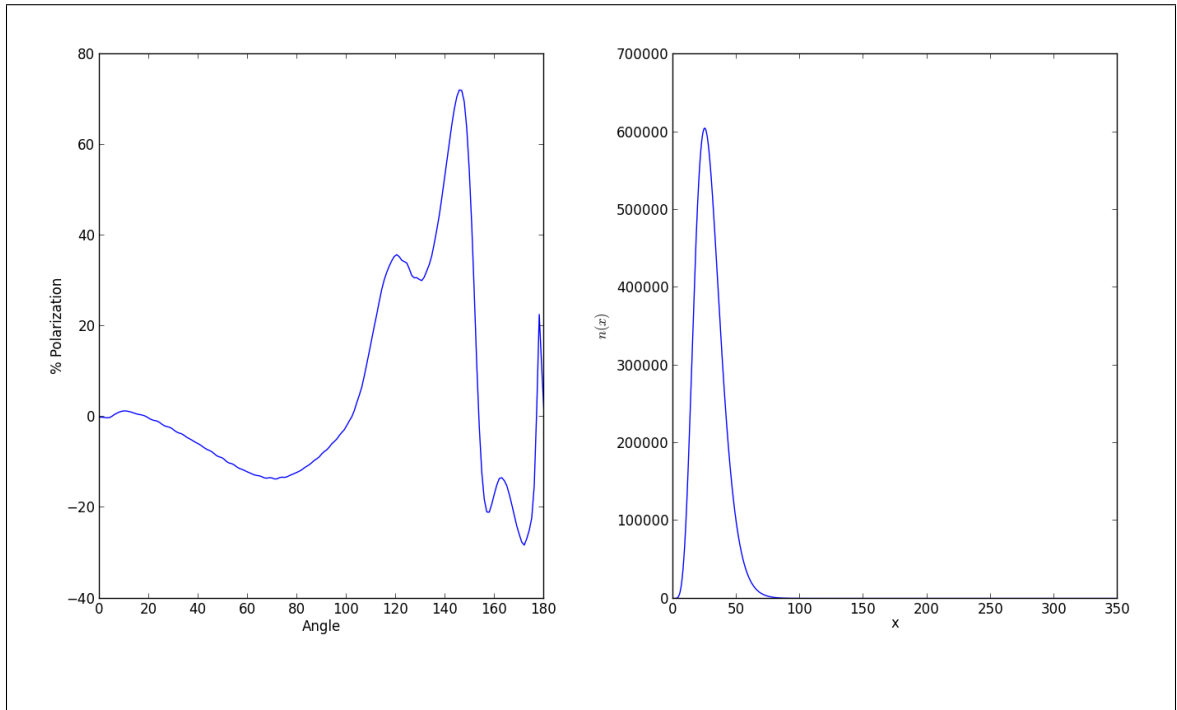


Figure 3.3: Reproduction of the results of Figure 3.1 for $x_{eff} = 37.5$. This calculation was performed by Mie scattering routine used for this thesis. The DLP as a function of the phase angle is shown accompanied by its respective PSD given by $n(x) = x^6 \exp(\frac{-9x}{x_{eff}})$.

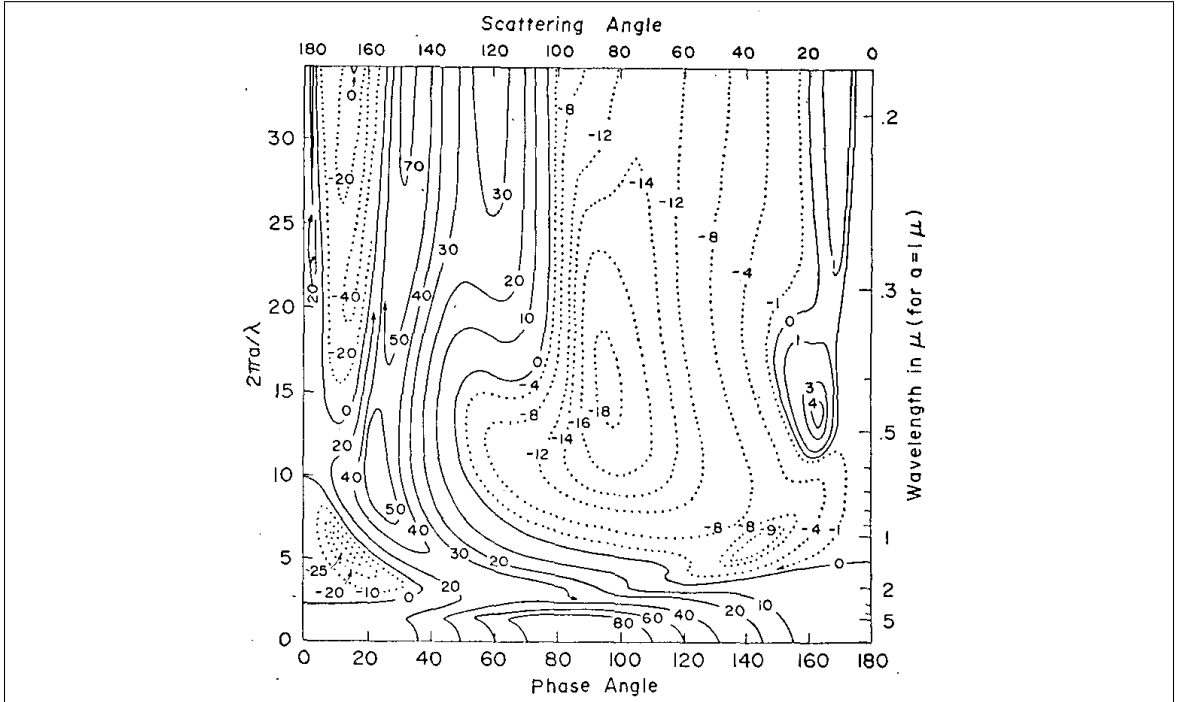


Figure 3.4: Contour figure published by Hansen and Hovenier (1974) for $n = 1.33$ and for values of effective size parameter x_{eff} ranging from 0–35, where $x_{eff} = \frac{2\pi R_{eff}}{\lambda}$ is given in terms of an effective radius R_{eff} . The PSD was given by the equation $n(R) = constant \times R^{17} \exp(\frac{-R}{.05 R_{eff}})$. For consistency, in the notation of this thesis $a = R_{eff}$. Reprinted by courtesy of J. Hansen.

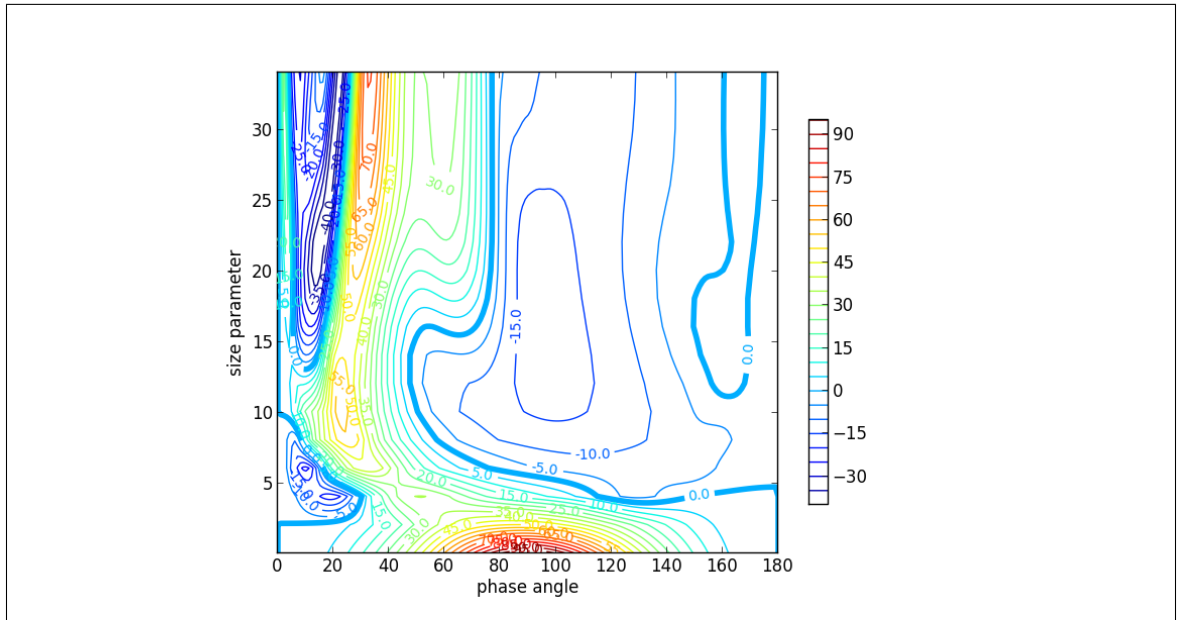


Figure 3.5: Reproduction of contour plot published by Hansen and Hovenier (1974) as shown in figure 3.4. The zero contour has been darkened for clarity. This figure has been calculated by the python code used to implement equation (2.62) in this thesis.

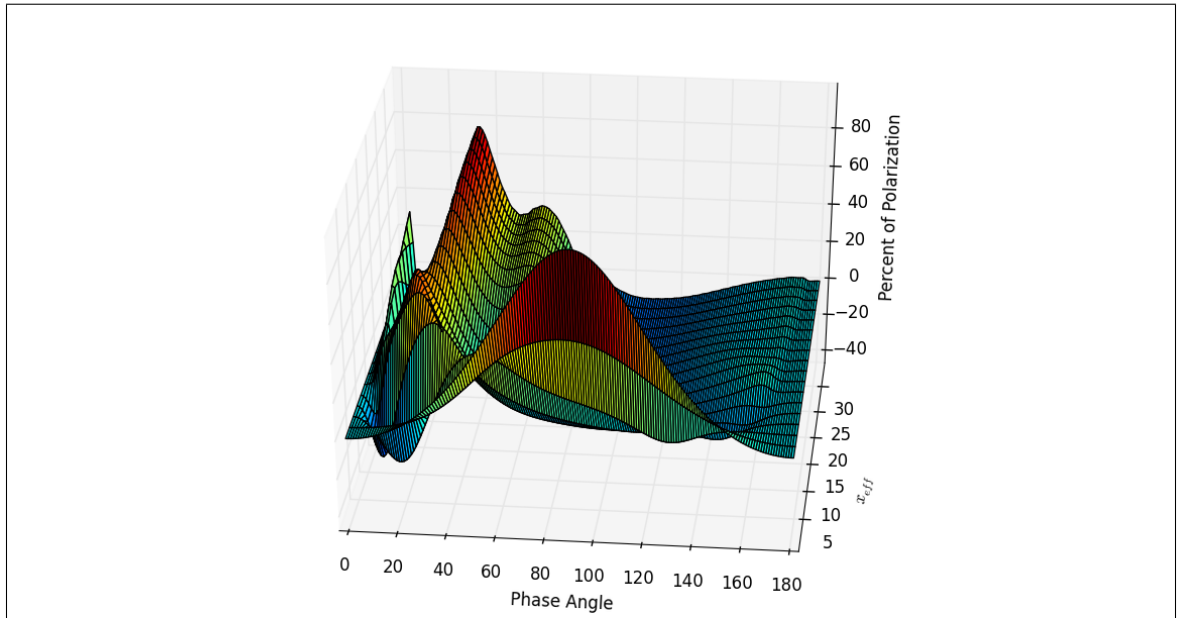


Figure 3.6: Three dimensional representation of the contour plot of Figure 3.5.

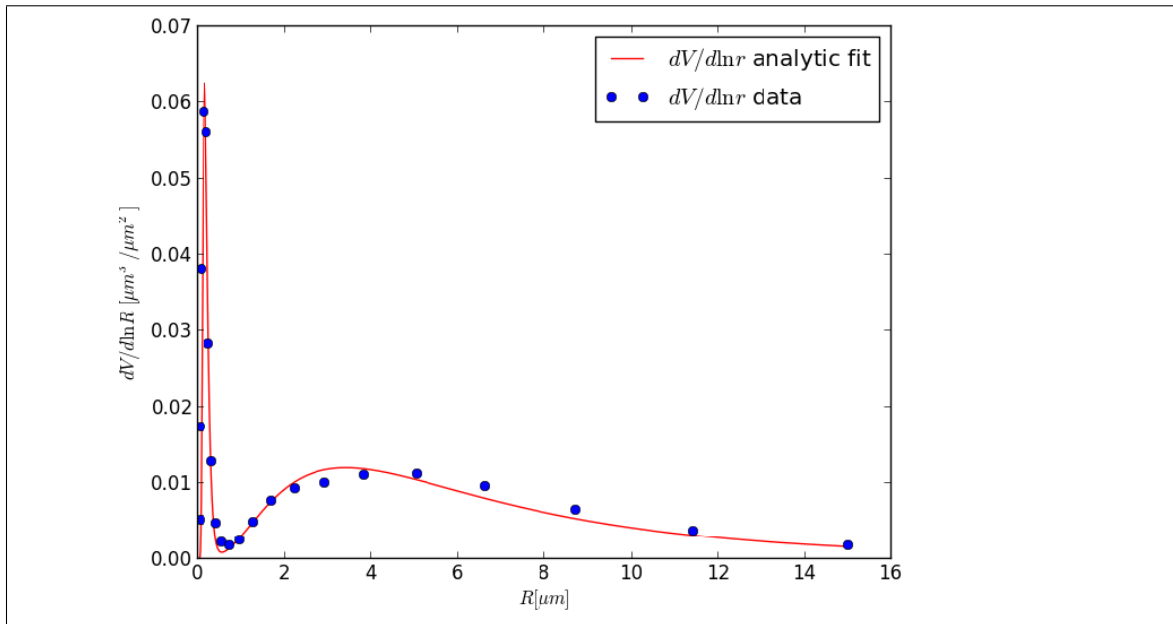


Figure 3.7: Comparison of data of VCD taken from AERONET against analytic log-normal curve. This sample VCD was taken from a data set from a photometer located at the Goddard Space Flight Center (GSFC) near Washington DC.

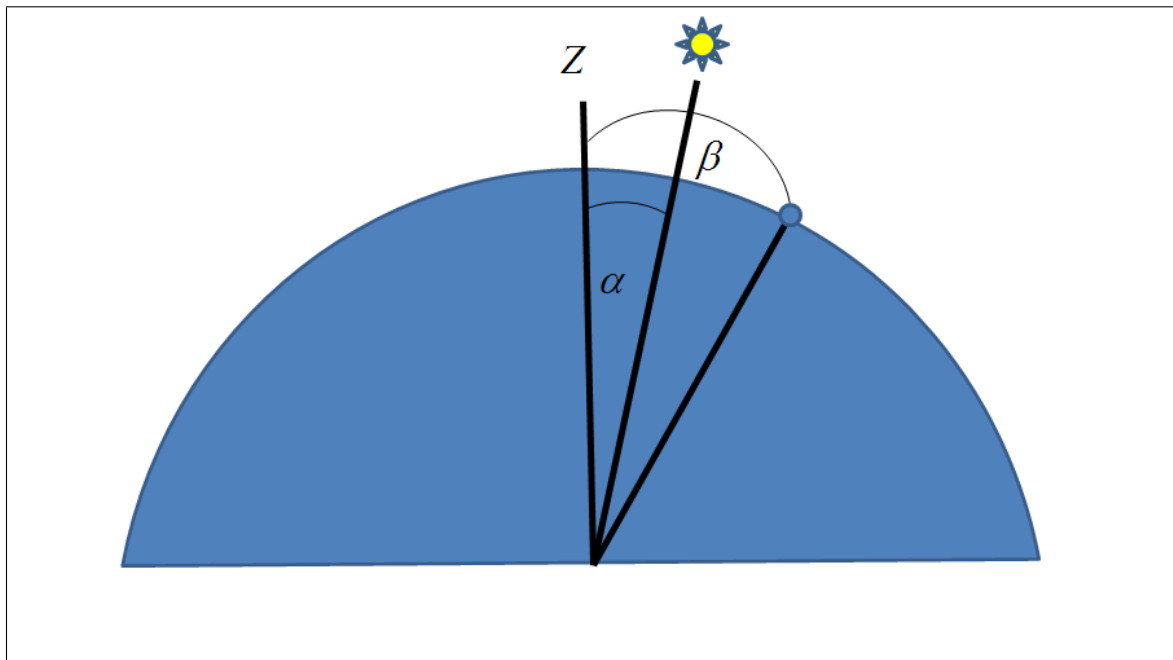


Figure 3.8: Illustration of the DLP measured by AERONET in the principal plane. The plane contains the zenith, the sun's angle with respect to the zenith and the instrument's position. The sun's position traces an angle α with respect to the zenith. The photometer points at the angle β from the zenith.

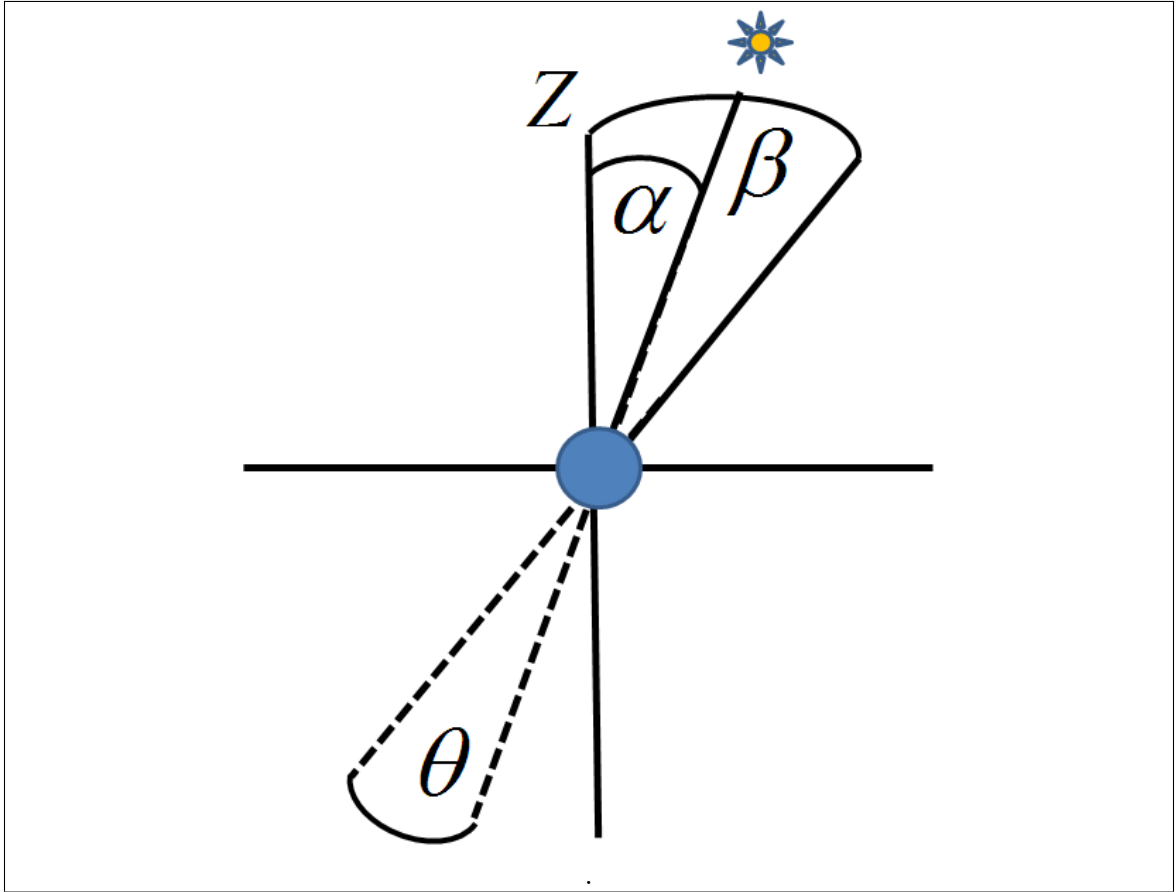


Figure 3.9: The orientation of forward scattering is in the direction of the incoming sunlight. The scattering angle is traced from the direction of forward scattering towards the position of the detector. The scattering angle is given by $\theta = |\beta - \alpha|$.

3.4.2 Beijing, China

Figures 3.10 and 3.11 illustrate a comparison between direct measurements of DLP against the calculation of DLP using the index of refraction and the particle size distribution. The selection of the time and site has been done depending on the availability of data. In order to compare theory and experiment, measurements of polarization, index of refraction and particle size distribution must be available within a time interval of at most ninety minutes. As mentioned in section 3.4.1, this is referred to as a coincidence. Figure 3.10 and Figure 3.11 display the calculated value of χ^2 on top. Figure 3.12 displays the χ^2 value of all the coincidences found at this site. The scatter plot indicates that a large majority of coincidences fall within the range $0.001 \lesssim \chi^2 \lesssim 0.01$ which corresponds to the χ^2 values found in Figure 3.10 and Figure 3.11. This result indicates that the agreement found in both coincidences is typical. The Beijing aerosol is an example of “mixed” aerosol, usually assumed to be a mixture of dust and urban pollution. Figure 3.10 (April, 22, 2008) generally shows a very good agreement between theory and measurement except at the highest values of β . Figure 3.11 (November 29, 2003) shows less agreement near the maximum of the DLP curve but agrees very well at the highest and lowest values of β .

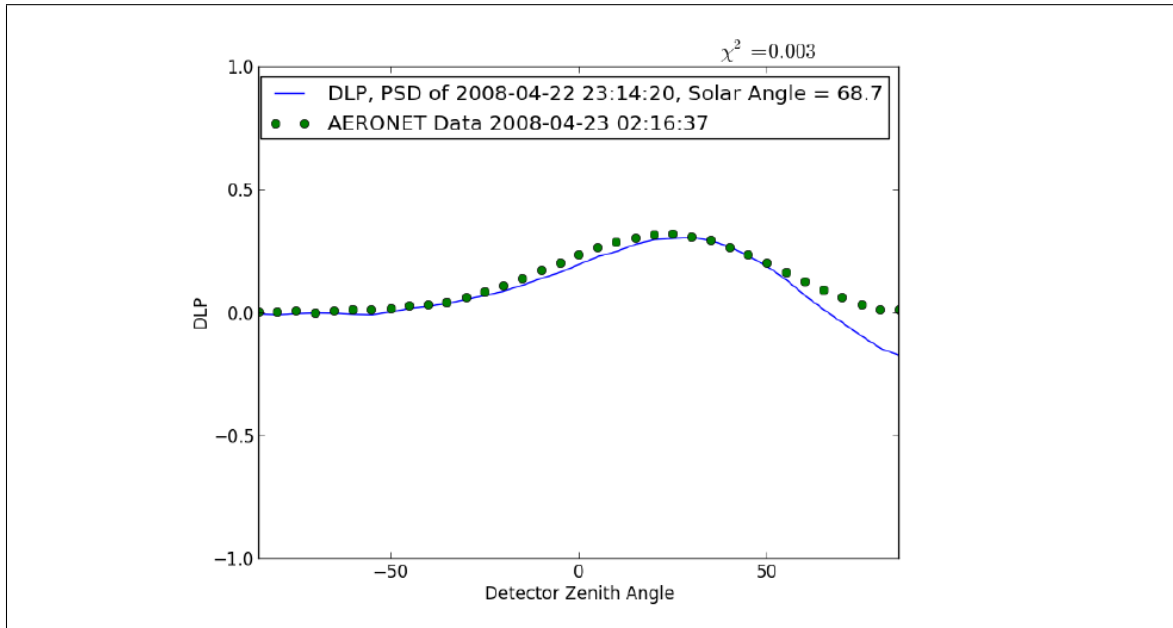


Figure 3.10: Coincidence found in Beijing. The date, time and $\chi^2 = 0.003$ values of the coincidence are shown in the figure. The calculated DLP versus the photometer zenith angle is displayed as a solid line. The measurements are shown as small circles. The DLP measurement was taken a few minutes later. The evaluation of χ^2 is done by equation (3.13).

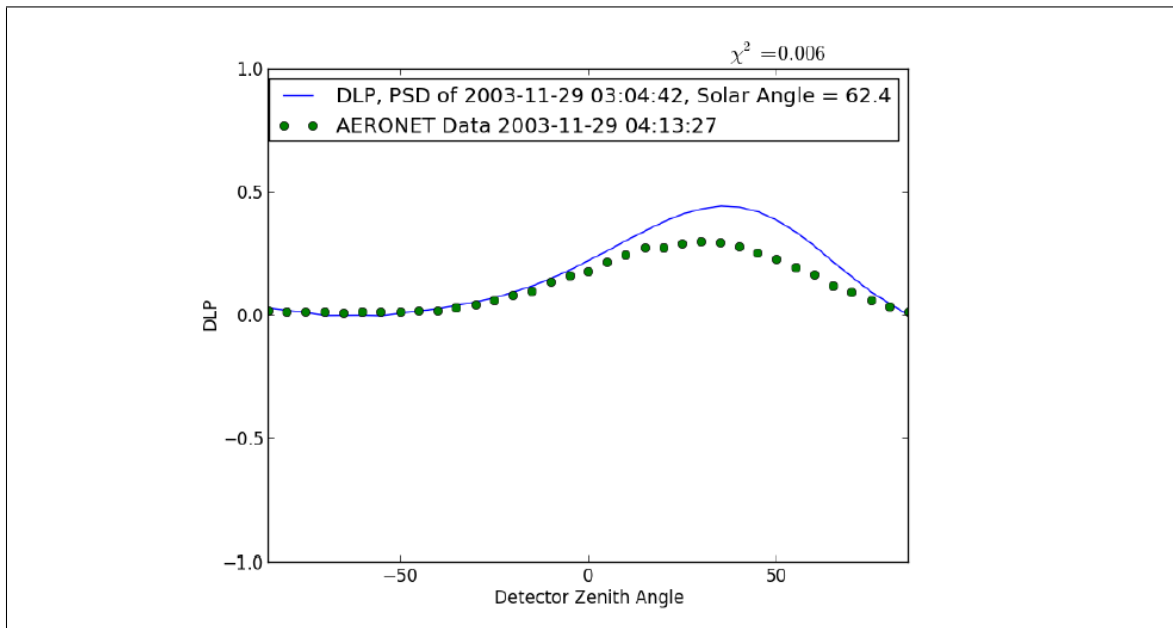


Figure 3.11: Coincidence found in Beijing. The calculated DLP versus the photometer zenith angle is displayed as a solid line. The measurements are shown as small circles. The agreement is indicated by the value $\chi^2 = 0.006$ displayed on top.

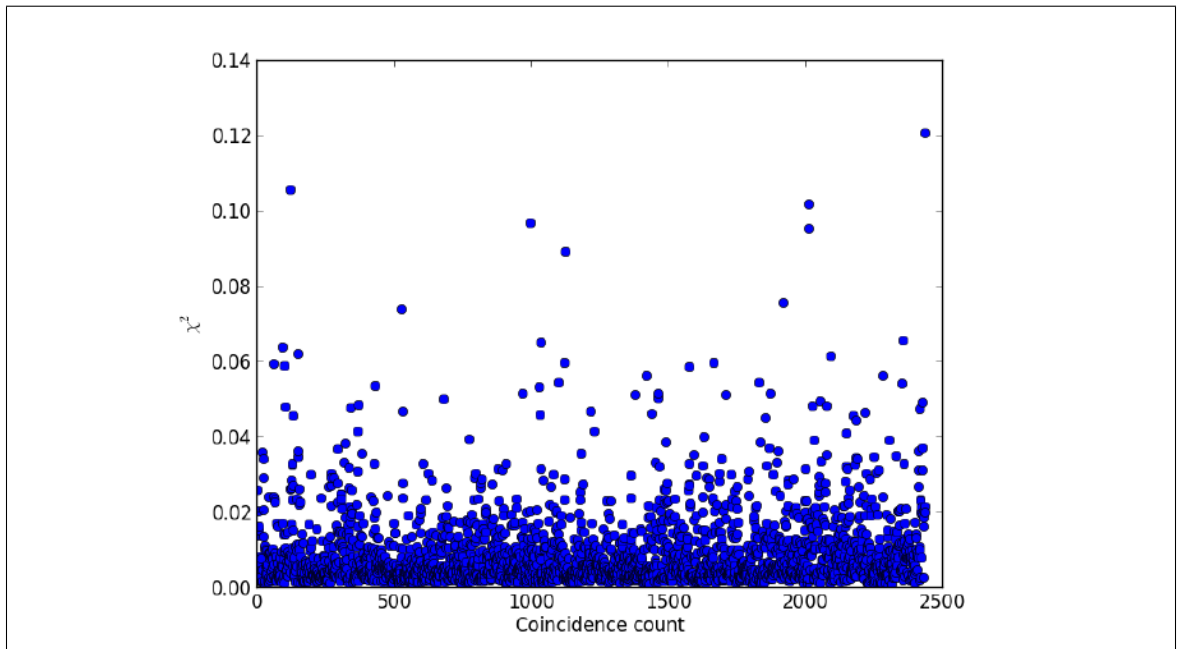


Figure 3.12: The occurrence of both a measurement of DLP and a combined measurement of index of refraction and PSD within ninety minutes at the same location is defined as a “coincidence.” The DLP is calculated using the index of refraction, solar angle, and PSD. The comparison of theory and measurement yields the χ^2 value described by equation (3.13). Although some anomalous coincidences have values of $\chi^2 > 0.3$, the bulk of the comparisons falls within $0.01 \lesssim \chi^2 \lesssim 0.1$ which are similar to the χ^2 values of Figure 3.10 and Figure 3.11.

3.4.3 Djougou, Benin

As in the previous section, the figures of this section illustrate the comparison between theory and experiment for Djougou, Benin. Figure 3.13 and Figure 3.14 illustrate the comparison of theory and experimental values of the DLP versus detector zenith angle. A complete overview of all the coincidences found at this site is displayed in Figure 3.15 in the form of a scatter plot.

Figure 3.13 (May 24, 2004) shows that the measured values of the DLP are somewhat larger than the theoretical values. Nevertheless, the agreement is fairly reasonable.

Figure 3.14 (March 15, 2006) shows a good agreement in the magnitude of the DLP but the measurements do not indicate the features that are present in the theoretical curve.

Figure 3.15 shows values of χ^2 for the nearly 1,000 coincidences found at this site. The range of χ^2 values is primarily between 0.001 and 0.01.

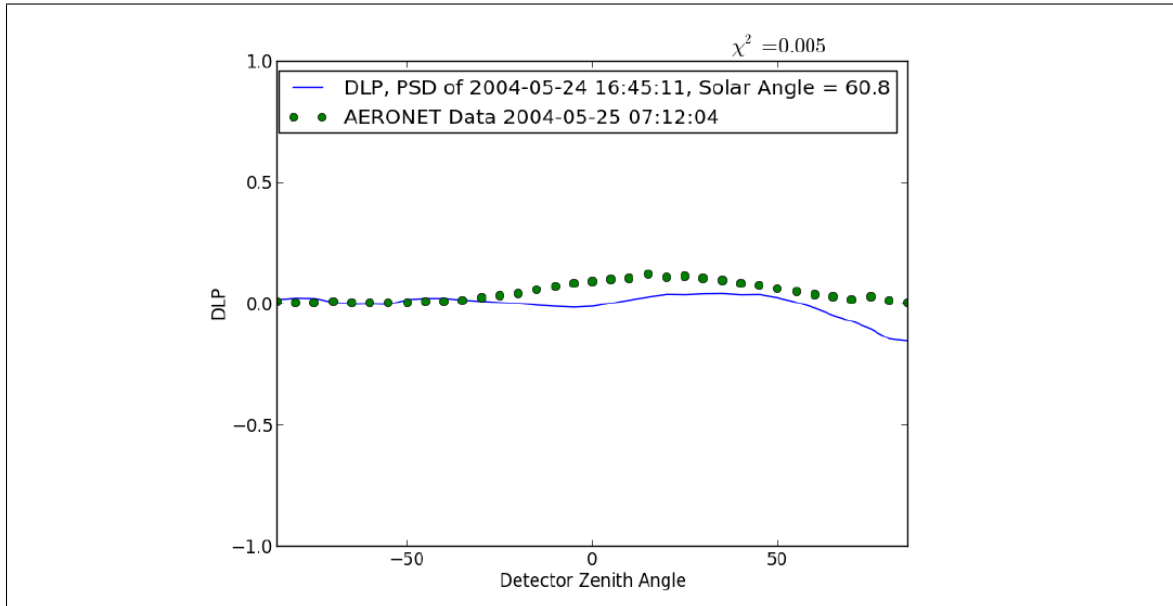


Figure 3.13: Djougou, the predicted DLP is displayed as a solid line. DLP actual measurements which are displayed as small circles were taken within a few minutes of PSD measurement. The evaluation of the agreement is given by its value of $\chi^2 = 0.005$.

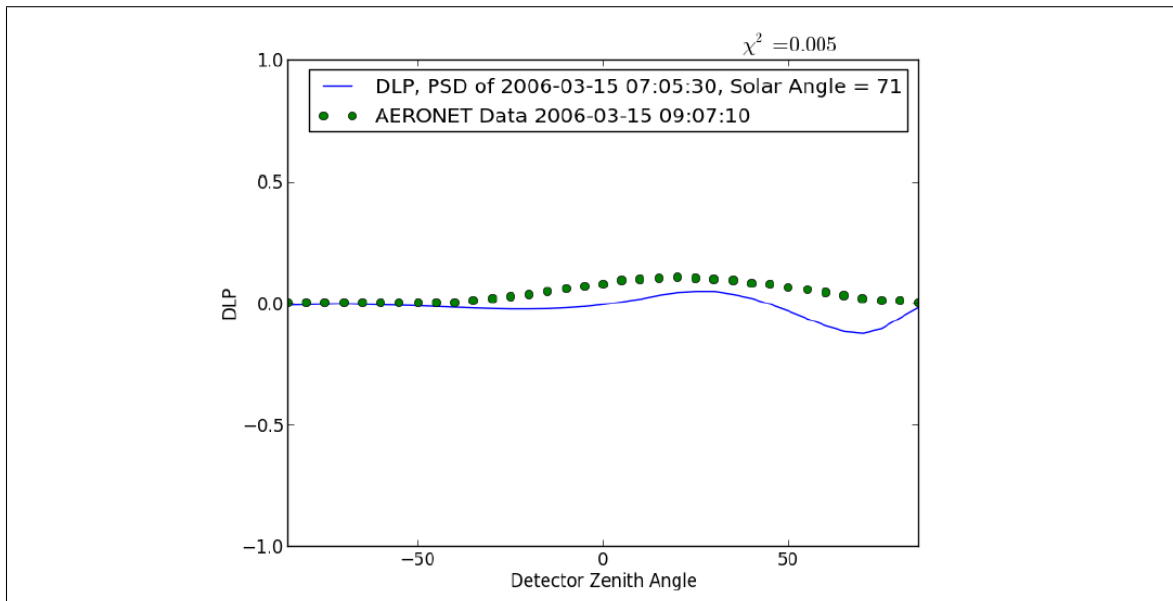


Figure 3.14: Coincidence found in Djougou. The date, time, and $\chi^2 = 0.005$ are displayed in the figure.

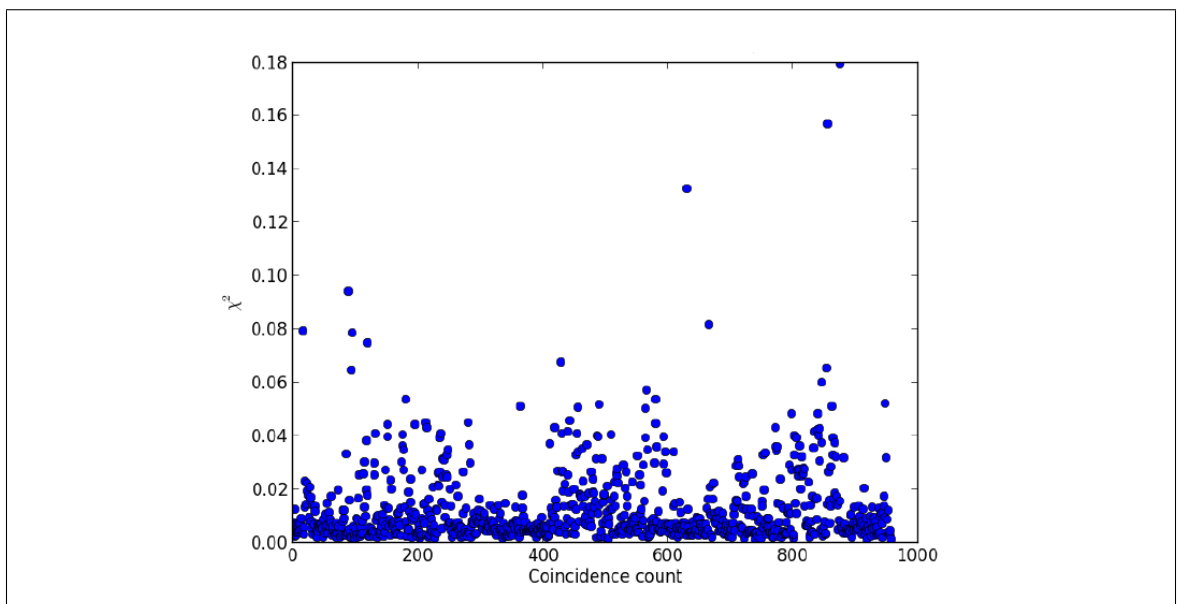


Figure 3.15: The χ^2 values of all the coincidences found in AERONET data from Djougou have been evaluated. A large number of coincidences fall within the range $0.001 \lesssim \chi^2 \lesssim 0.01$ which encloses the χ^2 values of Figure 3.13 and Figure 3.14.

3.4.4 Ras Al-Khaimah, United Arab Emirates

Ras Al-Khaimah is a city near Dubai. Due to its proximity to the desert, we expect this site to be dominated by dust-type aerosols. An illustration of two coincidences found at this site is displayed below in Figure 3.16 and Figure 3.17. The complete analysis of all the coincidences found in this site from the AERONET data is shown in Figure 3.18. A large concentration of coincidences fall within the range $0.001 \lesssim \chi^2 \lesssim 0.008$ which encloses the values of χ^2 of Figure 3.16 but does not enclose the χ^2 value of Figure 3.17. The small concentration of coincidences whose χ^2 is above 0.01 indicates that the poor agreement of Figure 3.17 is anomalous.

Figure 3.16 (August 20, 2004) shows a good agreement between calculated and measured DLP's. The main feature at $\beta \approx 30^\circ$ is well reproduced in the theoretical curve.

Figure 3.17 (September 12, 2004) was randomly selected from the 75 coincidences. Its agreement with theory is not as good as the one in Figure 3.16, nevertheless the feature at $\beta \approx 30^\circ$ is present in the theoretical curve.

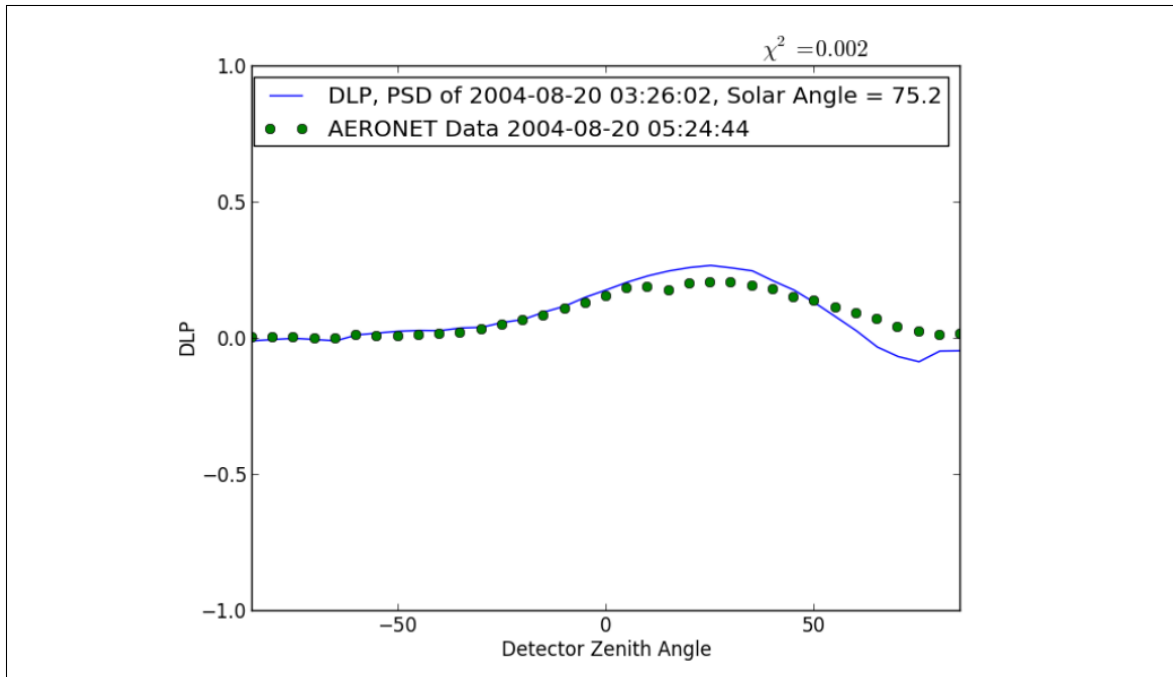


Figure 3.16: AERONET Photometer denoted “Smart” near Dubai. The predicted DLP versus detector zenith angle is shown. The DLP actual measurements were taken within a few minutes.

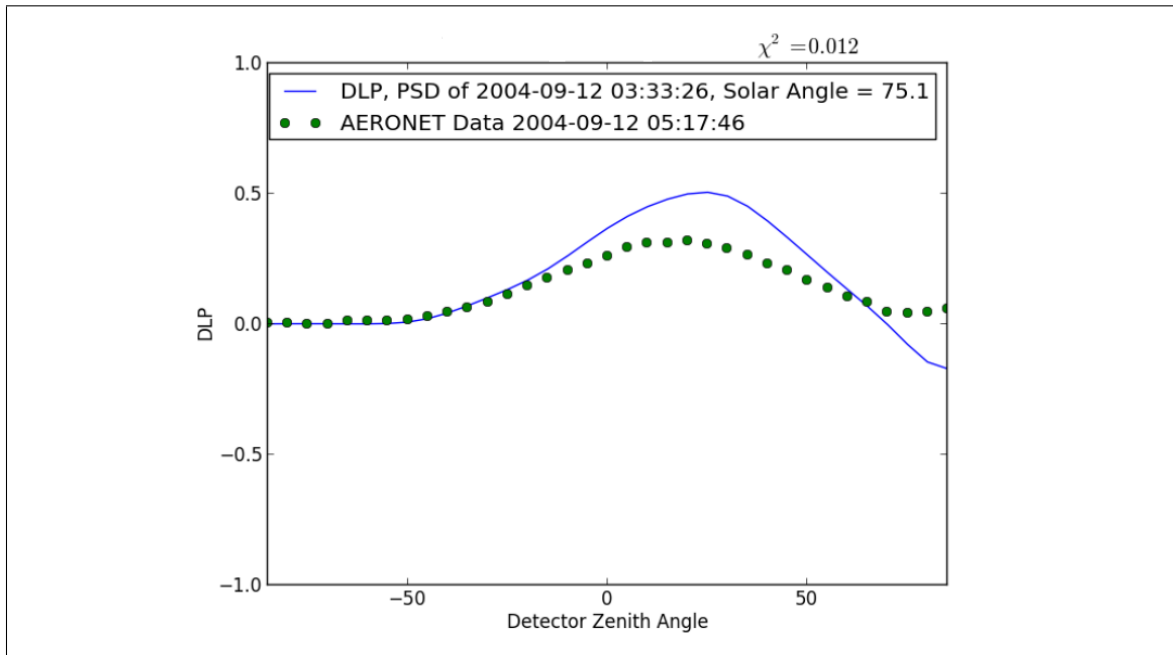


Figure 3.17: AERONET Photometer near Dubai. The predicted DLP versus detector zenith angle is shown. The DLP actual measurements were taken within 90 minutes. The χ^2 value is displayed at the top and the agreement is seen to be lower than that of Figure 3.16.

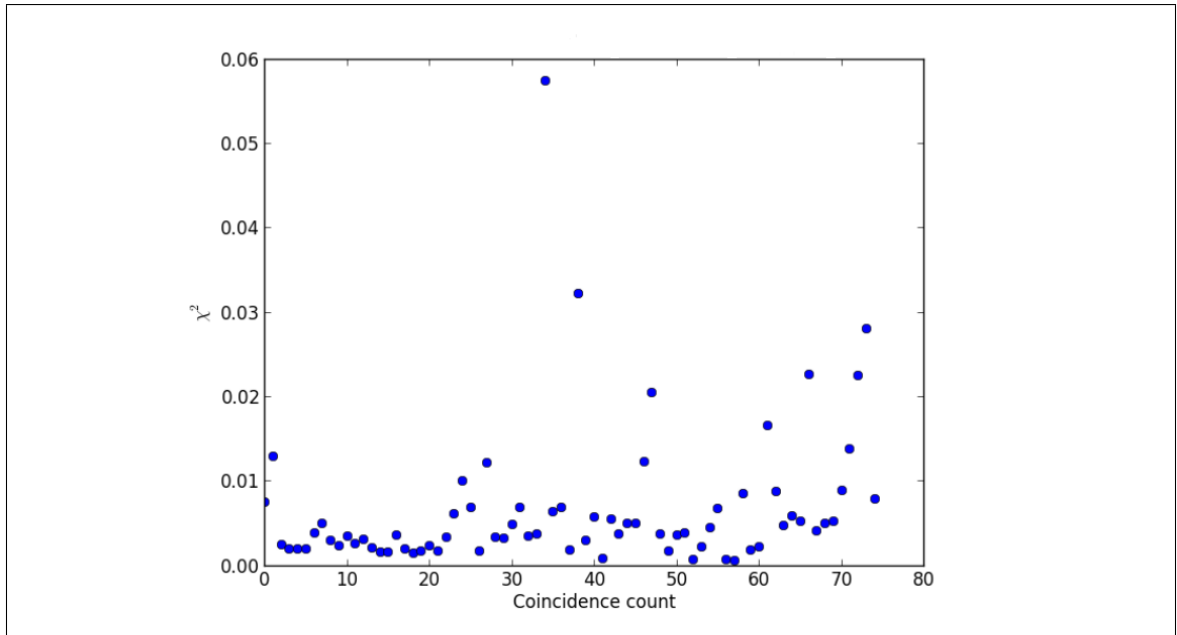


Figure 3.18: The analysis of all the coincidences found in AERONET data for Ras Al-Khaimah is displayed. Most coincidences are found to have values of $0.001 \lesssim \chi^2 \lesssim 0.008$ which are values similar to those of Figure 3.16. Notice the χ^2 value of Figure 3.17 is 0.012 which does not correspond to the majority. This means that the poor agreement of Figure 3.17 is an anomaly for this particular site.

3.4.5 Barcelona, Spain

The same analysis as in the previous sections is displayed for Barcelona, Spain. We present both a direct measurement of DLP and a calculation of DLP by Mie theory. The agreement of theory and measurement is given by χ^2 which is defined by equation (3.13). A significant number of coincidences are found to fall within the range $0.001 \lesssim \chi^2 \lesssim 0.01$ which encloses the χ^2 values of Figure 3.19 and Figure 3.20.

Figure 3.19 (April 4, 2009) shows an excellent agreement in generating the features of the measured DLP, although the height of the peak of the DLP is somewhat higher for the theoretical curve.

Figure 3.20 (September 26, 2009) also shows very good agreement between theory and measurement although once again the theoretical curve is somewhat higher at the peak.

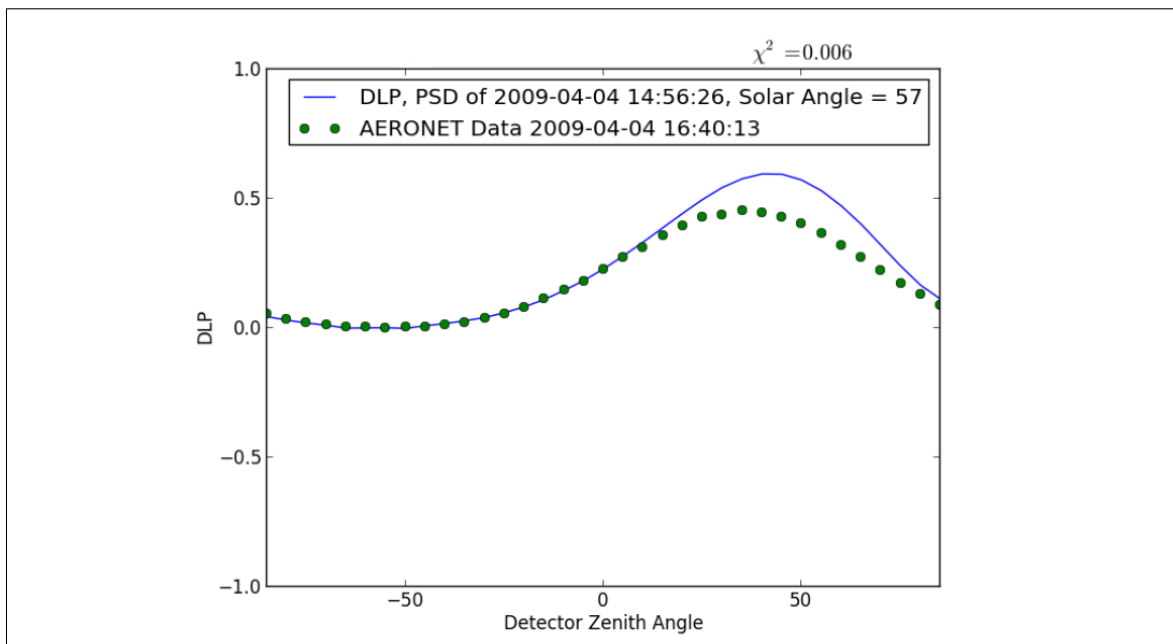


Figure 3.19: AERONET Photometer in Barcelona, Spain. The predicted DLP for a given solar zenith angle is shown. The actual measurements of DLP were taken within ninety minutes of PSD. The χ^2 value of this coincidence is displayed on top of the figure.

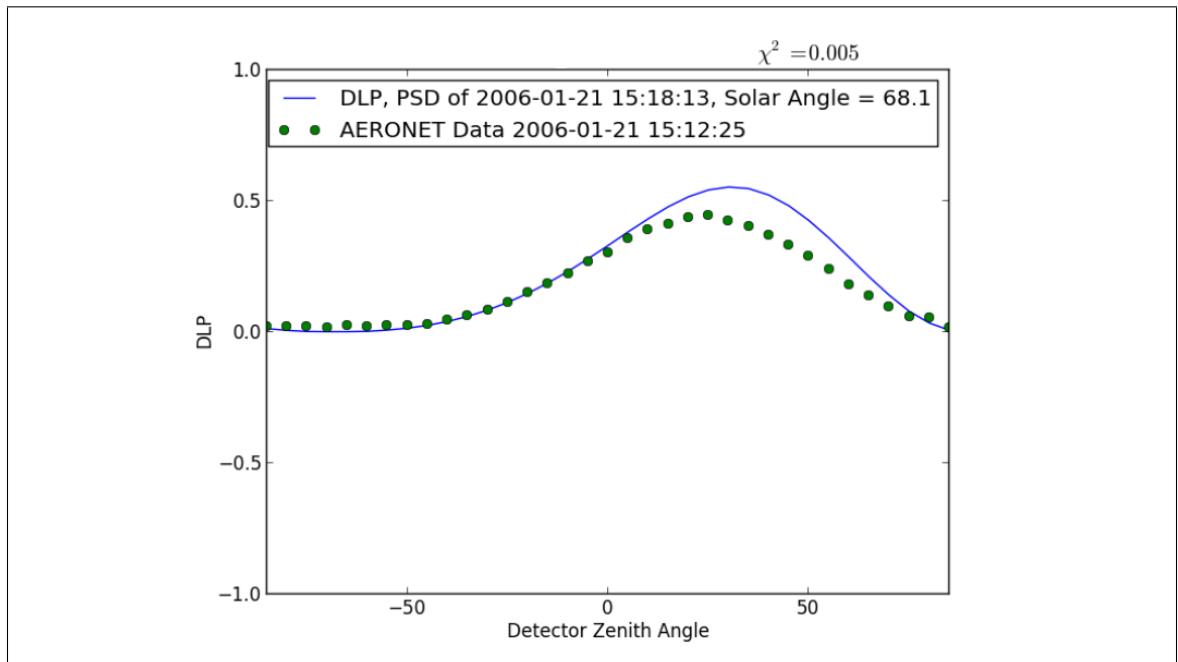


Figure 3.20: AERONET Photometer in Barcelona, Spain. The predicted DLP for a given solar zenith angle is shown. The actual measurements of DLP were taken within a few minutes of PSD. The χ^2 value of this coincidence is displayed on top of the figure.

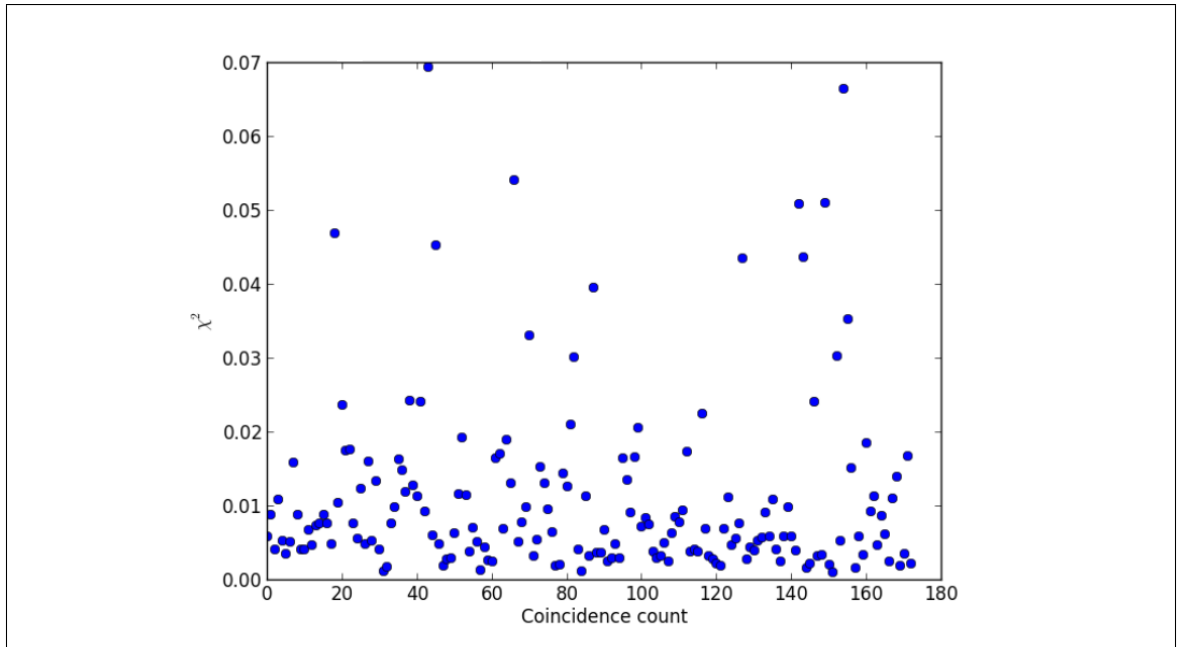


Figure 3.21: All found coincidences from AERONET data have been evaluated by the χ^2 value given by equation (3.13). The values are displayed as a scatter plot and it is noticeable that the greatest concentration of χ^2 values from this site fall within $0.001 \lesssim \chi^2 \lesssim 0.01$. This range corresponds to the χ^2 values found in Figure 3.19 and Figure 3.20.

3.4.6 Osaka, Japan

In this section, as in the analysis of the previous sites, we present two comparisons of the measured DLP versus the calculated DLP. The illustrations of these coincidences are shown in Figure 3.22 and Figure 3.23. As in the previous cases, the agreement of these comparisons is given by their χ^2 values which are displayed at the top of each figure. For completeness, Figure 3.24 displays a scatter plot of all the coincidences found from the AERONET data. From the scatter plot, we can appreciate that the majority of coincidences are found within the range $0.001 \lesssim \chi^2 \lesssim 0.008$ which corresponds to the values of Figure 3.22 and Figure 3.23.

Figure 3.22 (November 7, 2004) has generally good agreement between measurement and theory but the peak of the theoretical curve is shifted somewhat to larger β .

Figure 3.23 (April 2, 2004) shows a reasonably good agreement between theoretical DLP and measured DLP, although the theoretical value is somewhat too high at the peak and a bit low at $\beta = 85^\circ$.

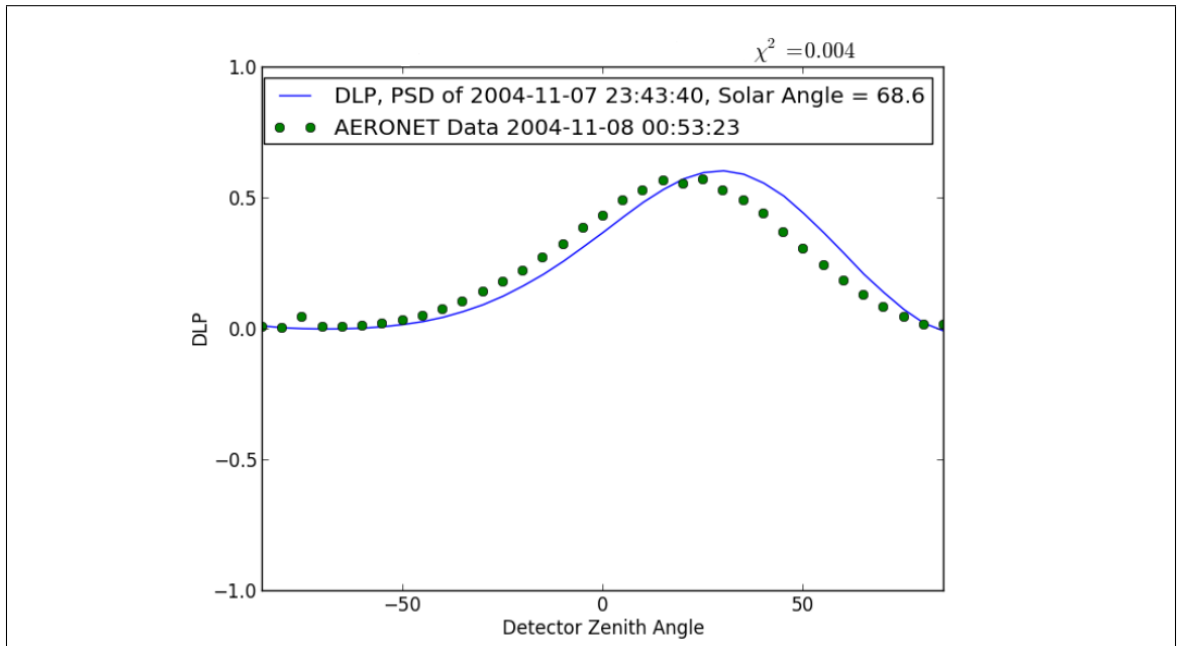


Figure 3.22: AERONET Photometer in Osaka, Japan. The predicted DLP for a given sun zenith angle is shown. DLP actual measurements were taken within a few minutes of PSD. The χ^2 displayed on top evaluates the agreement of measurement with calculation.

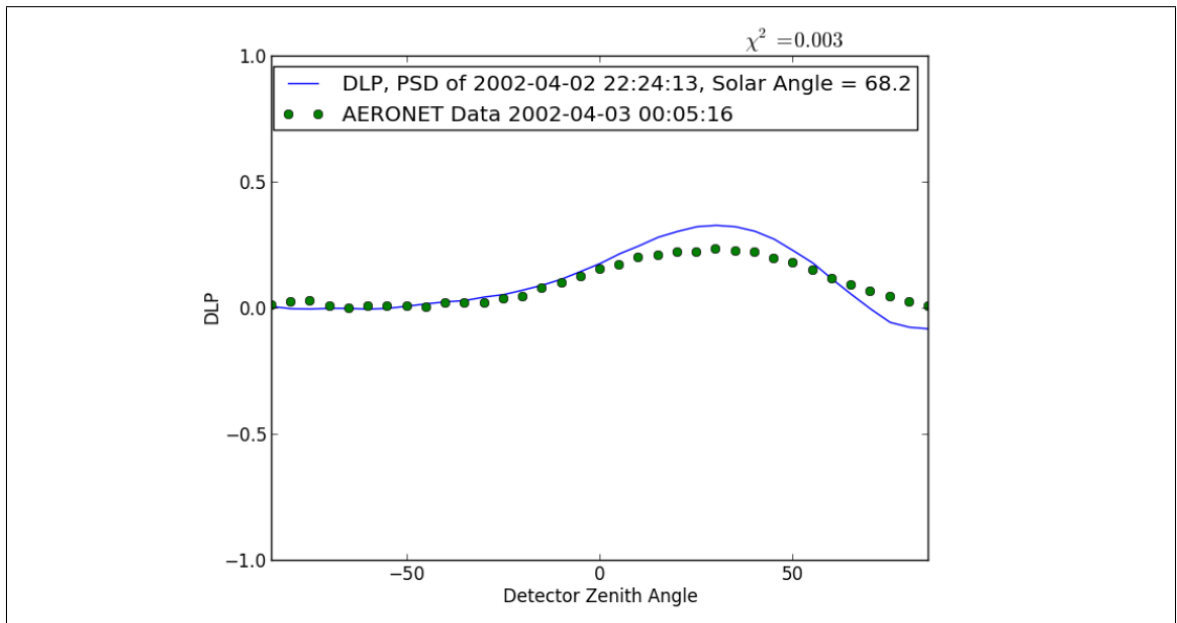


Figure 3.23: AERONET Photometer in Osaka, Japan. The predicted DLP for a given solar zenith angle α is shown. DLP actual measurements were taken within a few minutes of PSD. The evaluation of the agreement is stated on top by the figure's χ^2 value.

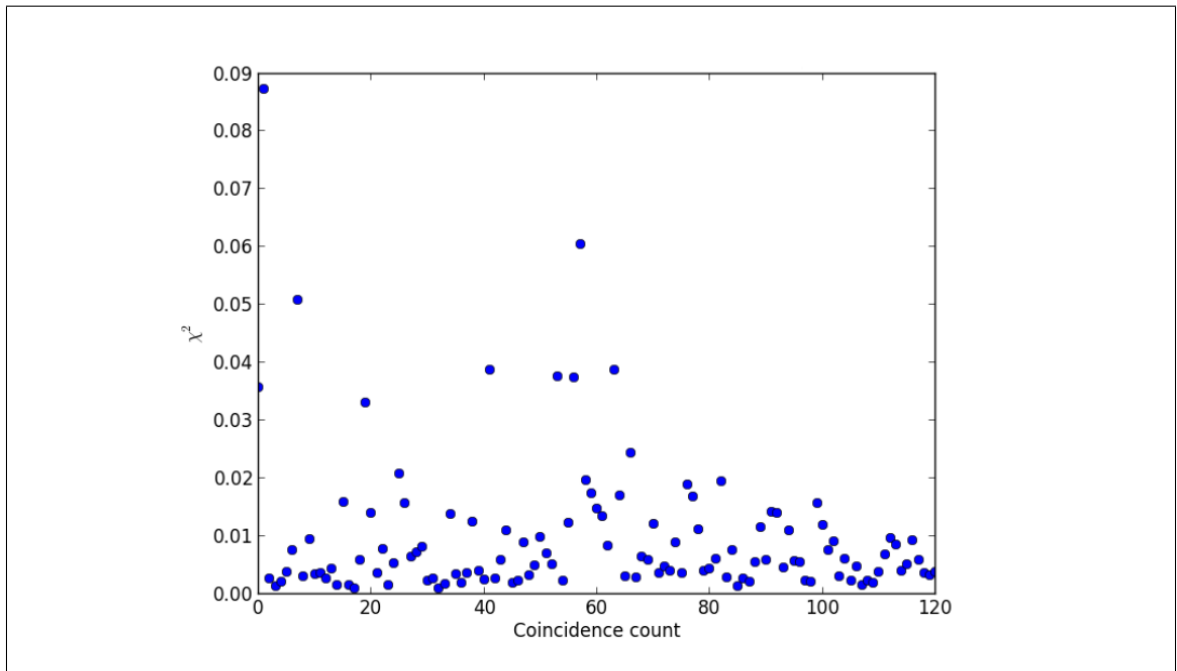


Figure 3.24: All found coincidences of data provided by AERONET have been evaluated by the χ^2 value given by equation 3.13. The values have been represented as a scatter plot and it is easy to see that majority of the coincidences fall within $0.001 \lesssim \chi^2 \lesssim 0.008$. This range corresponds to the χ^2 values displayed in Figure 3.22 and Figure 3.23, demonstrating that their agreement is typical and not anomalous.

3.5 Data Analysis of Representative Aerosol Sites

Certain locations have aerosols that are predominantly composed of a given type. For example, a desert location can be expected to have aerosols that are predominantly sand. A jungle location will have biomass aerosols, and a large city would be characterized by urban-industrial aerosols. Hamill et al. (2014) have assumed that the main aerosol types are urban-industrial, biomass, dust, “mixed,” and maritime. The “mixed” category is believed to be composed of soot and sulfates. In this section, we shall consider the theoretical calculations of DLP to see if one can use it to distinguish one type of aerosols from another.

As mentioned in section 3.2, the logarithmic volume concentration distribution (VCD) rather than the particle size distribution (PSD) is given by AERONET. Before the numerical integration of equation (3.8) can be done, the VCD was curve-fit to an analytic function by using equation (3.11). The technique for curve-fitting the VCD is explained in section 3.3. The mean radius and standard deviation of the fine mode and the coarse mode were also obtained from AERONET.

The evaluation of the accuracy of the curve fit was done according to the method of least squares χ^2 . This quantity has been used before in the evaluation of agreement of theory and experiment of section 3.4 by using equation (3.13). Once again, the agreement of the analytic curve fit and the measured value of the PSD is evaluated numerically according to the formula

$$\chi^2 = \frac{1}{n-1} \sum_j^n (Y_{fit}(R_j) - Y_{data}(R_j))^2, \quad (3.14)$$

where $Y_{fit}(R_j)$ and $Y_{data}(R_j)$ are respectively the analytic and experimental value of the VCD evaluated at R_j . The quantity n is the number of data points in the sample, in this case $n = 21$. We randomly collected sixty PSD’s with their corresponding indexes of refraction from all available VCD inversions. The

calculation of DLP by the method of equation (2.62) was performed using $\lambda = 873 \text{ nm}$ and the respective refractive index. This particular value of wavelength was chosen because polarization measurements by AERONET are taken using wavelengths close to this value (Holben et al., 1998). The sixty randomly selected DLP data sets yielded the average DLP for each site.

3.5.1 Site: Goddard Space Flight Center (GSFC)

Goddard Space Flight Center (GSFC) is located near Washington, DC and is usually assumed to be an example of urban-industrial aerosol. The VCD was curve-fit using equation (3.11), and an illustration is shown in the bottom panel of Figure 3.25. It is interesting to note that the size distribution shows a large peak in the fine mode. The accuracy of all available curve-fits from the sample is summarized in the top panel of Figure 3.25. Sixty of those PSD's displayed in Figure 3.25 were selected at random to calculate the DLP. The top panel of Figure 3.26 shows an overview of all 60 calculated DLP's as a surface plot, while the bottom panel shows the average DLP and the standard deviation. In section 3.6, the sensitivity of the DLP to the change in parameters of the PSD and the index of refraction will be explored. Figure 3.27 displays a histogram of the index of refraction from this site.

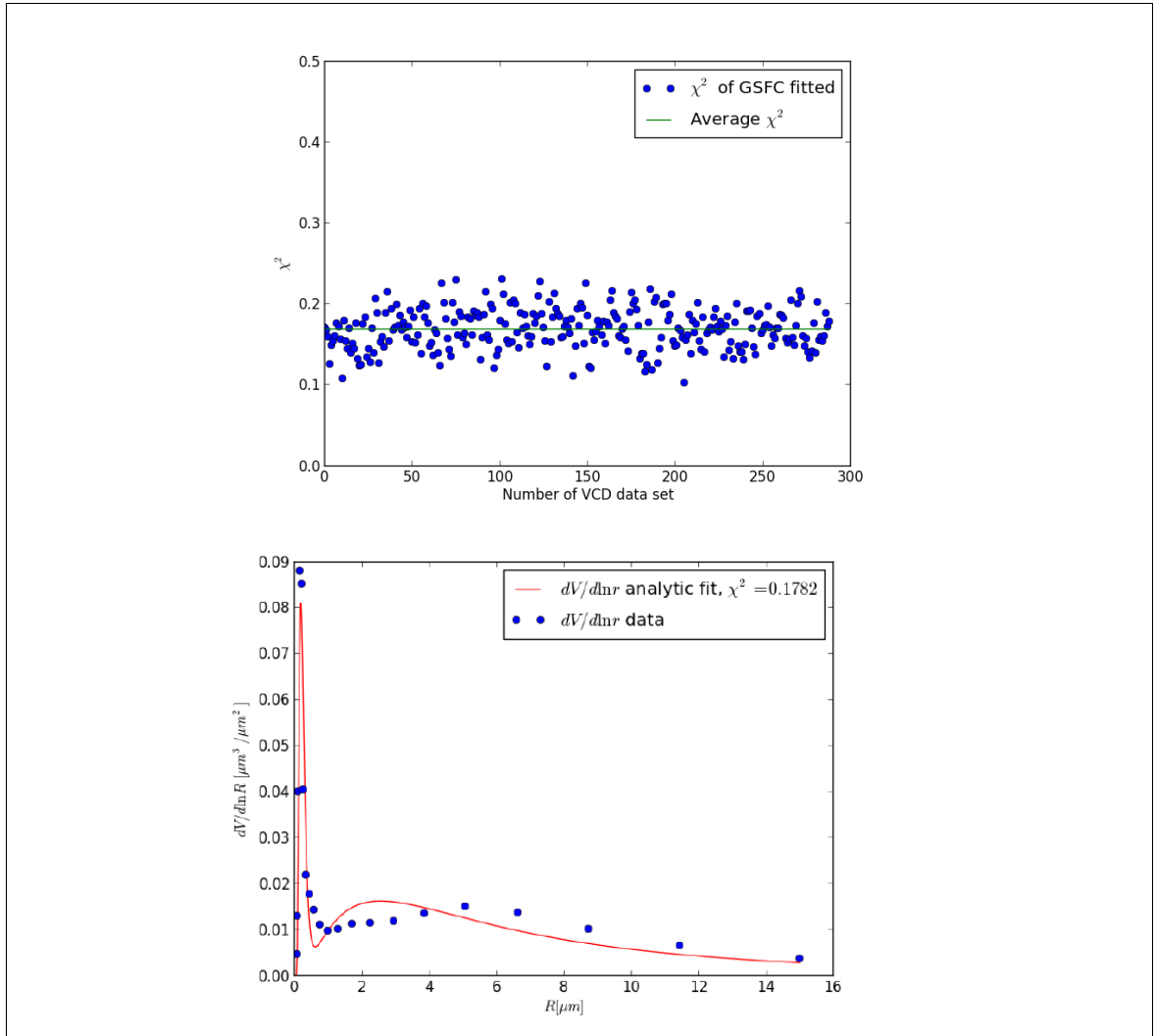


Figure 3.25: Top: all PSD's from GSFC whose index of refraction was available were curve-fit using equation (3.11). Each fit yielded a value for χ^2 by the use of equation (3.14). The scatter plot displays the χ^2 value of all the available VCD that were curve-fitted. Bottom: illustration of a VCD from GSFC chosen at random. The AERONET data is shown as a set of 21 circles. The curve-fit is shown as a solid line.

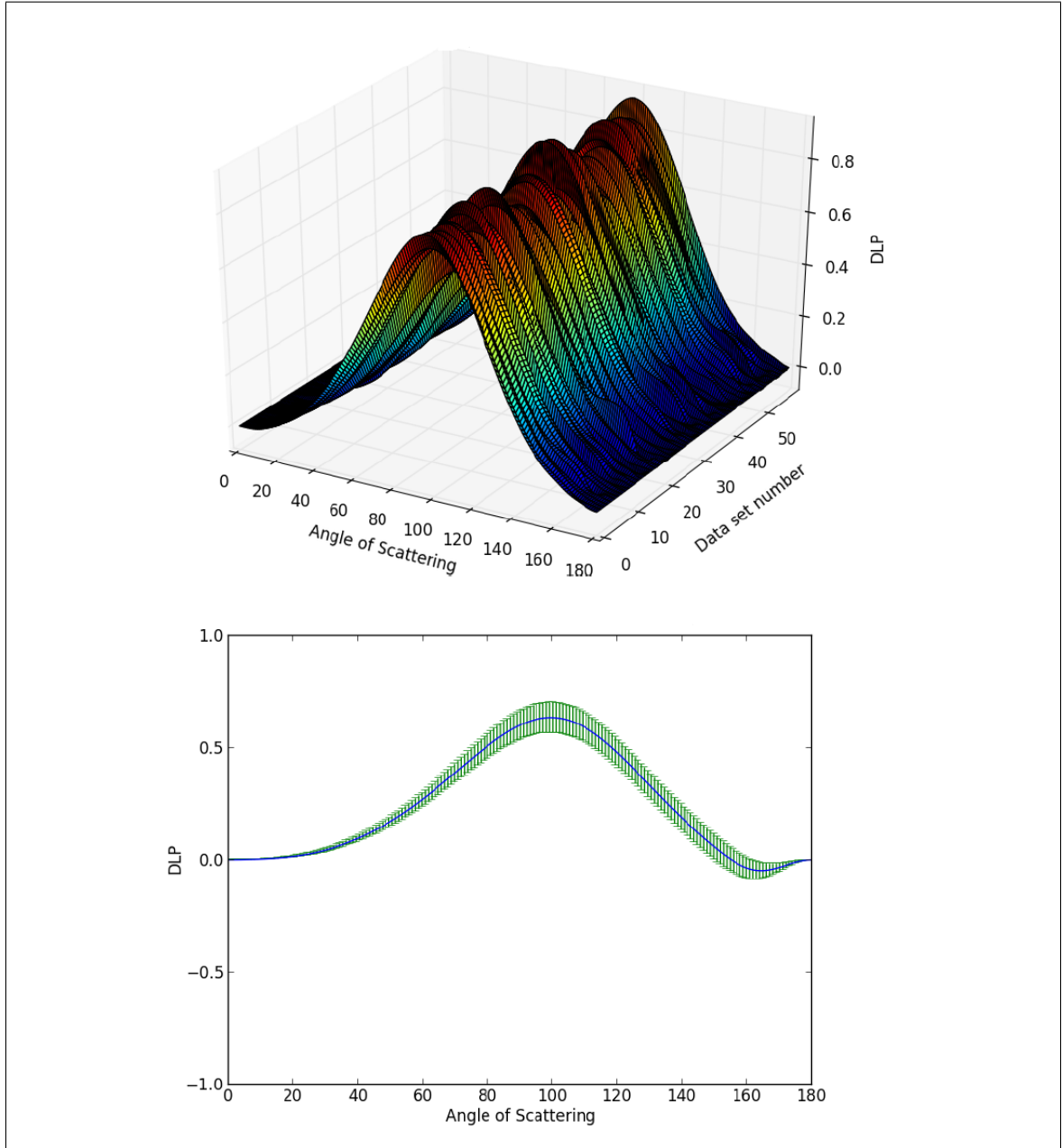


Figure 3.26: Top: Overview of sixty randomly chosen PSD from GSFC whose index of refraction was known. The $DLP(\theta)$ has been calculated by equation (2.62). Bottom: average $DLP(\theta)$ the sixty calculated from GSFC

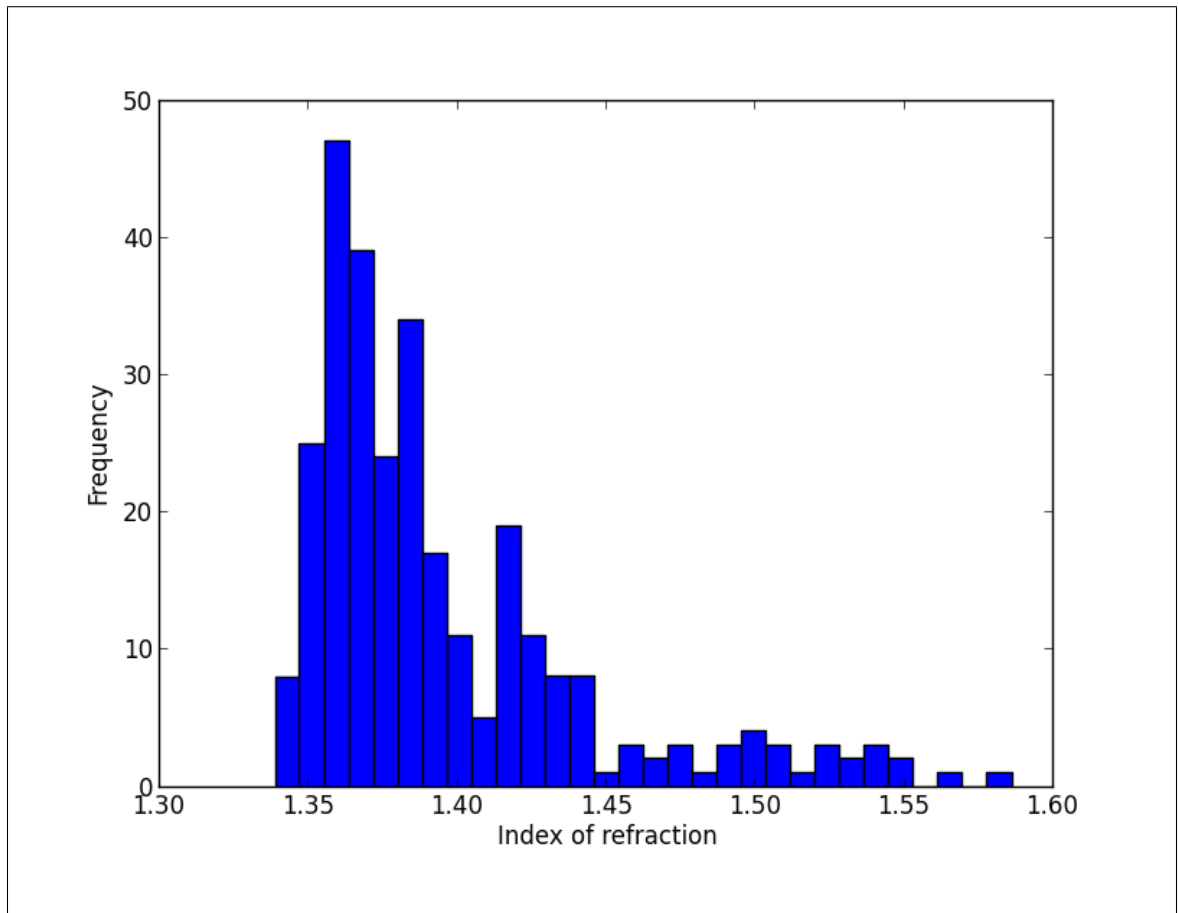


Figure 3.27: Histogram of all the AERONET available index of refraction measurements taken from GSFC between May 1993 and July 2012.

3.5.2 Site: Solar Village

Solar Village is located in Saudi Arabia, and the aerosol at that site is normally dust. In Figure 3.28, an illustration of a typical particle size distribution is shown. This size distribution is accompanied by a scatter plot which displays the χ^2 value of all available particle size distributions from this site that had an inverted value of index of refraction. From this set of PSD's, we selected sixty at random. The DLP was calculated for all 60 selections and is displayed both as a surface plot and as an average in Figure 3.29.

In Figure 3.28 the bottom panel shows a typical theoretical VCD fit (solid line) and the AERONET data used to generate it. The top panel shows the χ^2 value of the nearly 5,000 size distributions given at Solar Village.

In Figure 3.29, we present the DLP as a function of angle of scattering. The top panel is a 3-D surface of all of the data and the bottom panel shows the average value and its respective standard deviation. Note the difference between the average DLP in Figure 3.29 and the DLP for GSFC in Figure 3.26.

Furthermore, comparing Figure 3.30 with Figure 3.27, we note that histogram of the index of refraction at solar village is significantly different from the histogram of the index of refraction at GSFC.

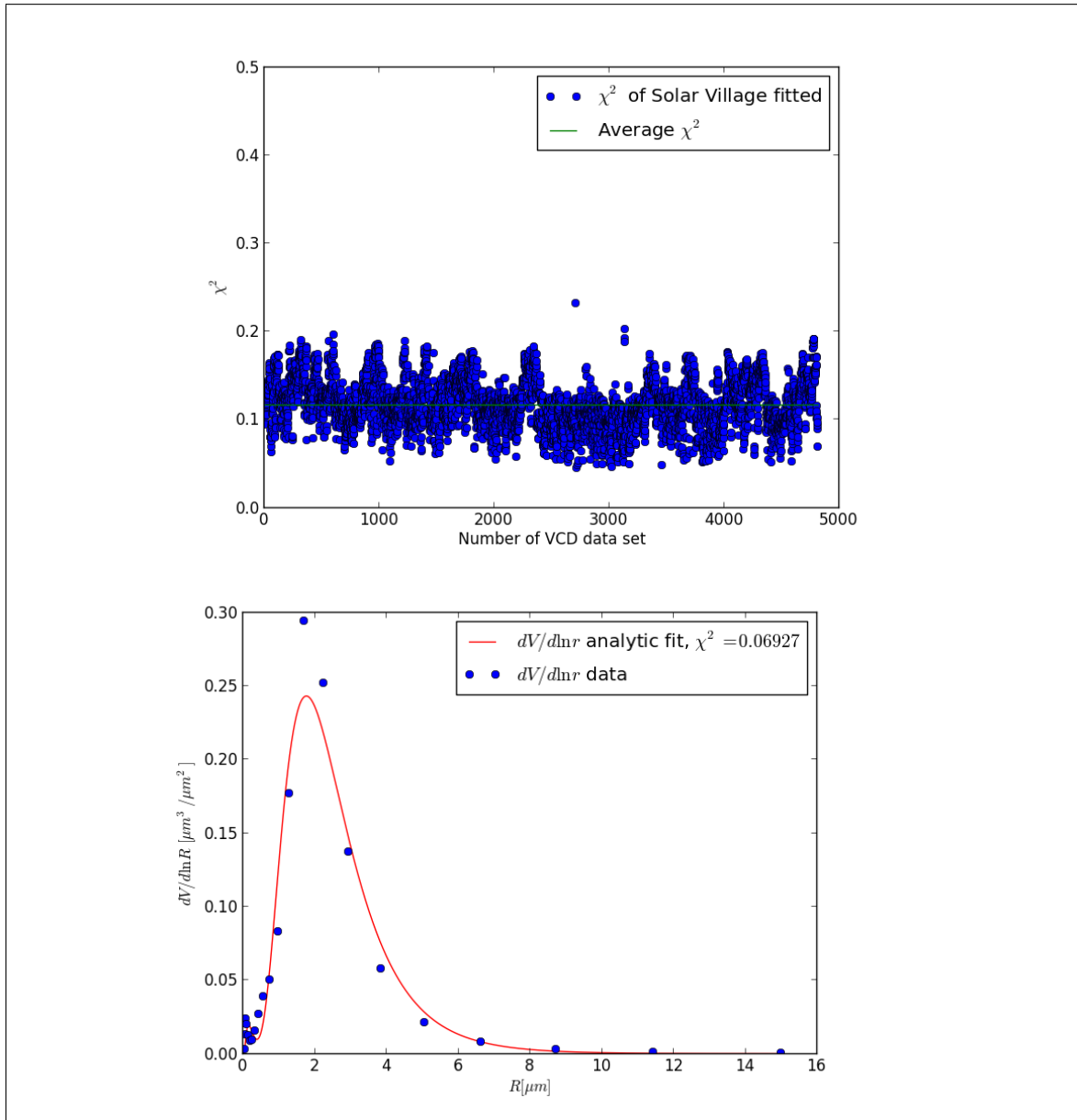


Figure 3.28: Top: all curve-fitted VCD's from Solar Village have been evaluated by equation (3.14). The χ^2 value of all data set has been plotted and its average value is displayed as a solid line. Sixty of those curve-fits have been selected at random to calculate the DLP of Figure 3.29. Bottom: sample of a VCD from Solar Village curve-fit by equation (3.11).

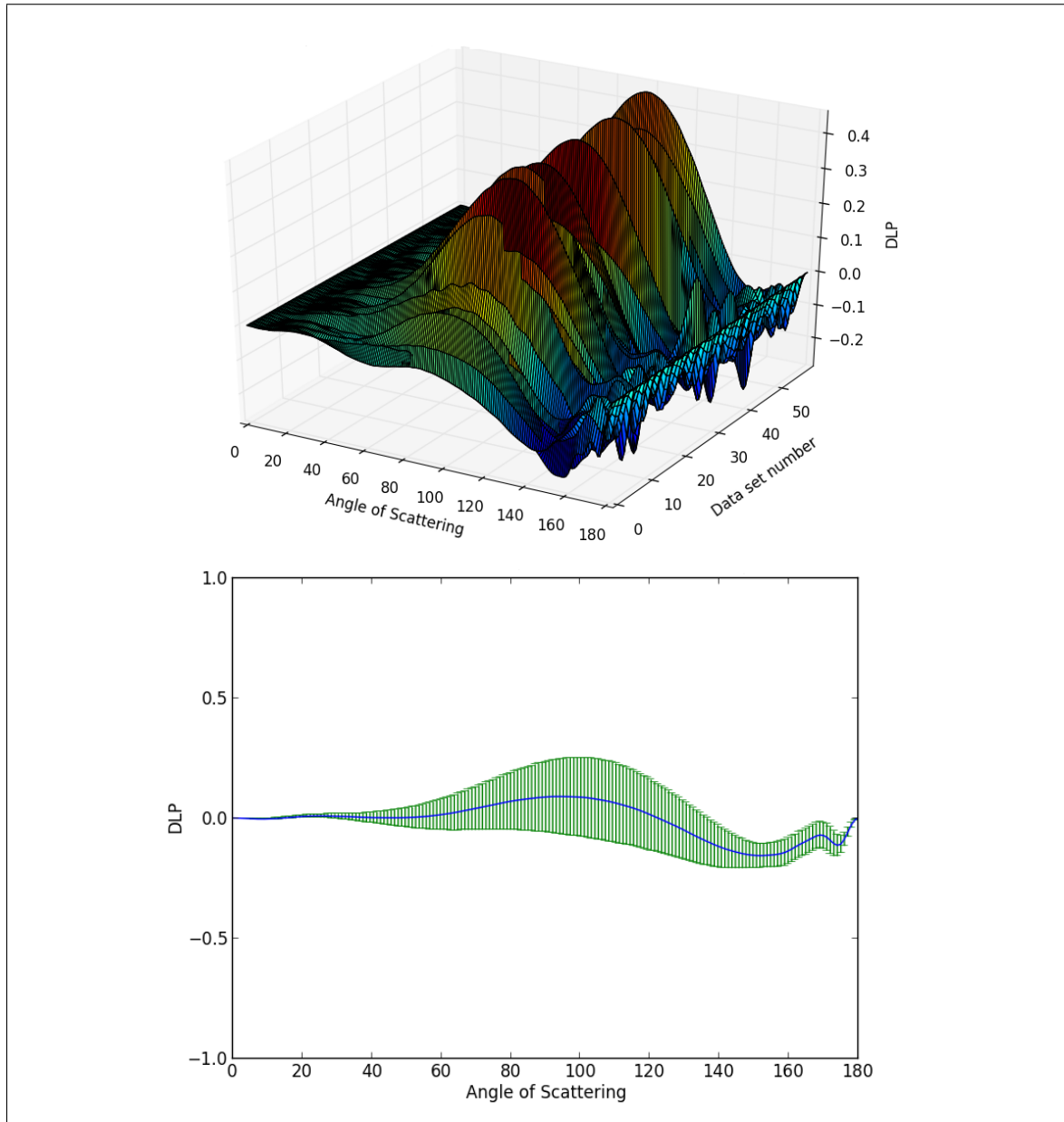


Figure 3.29: Top: overview of sixty randomly selected PSD's from Solar Village whose DLP has been calculated. The index of refraction was given in the data set. Bottom: average DLP for all sixty selected PSD. The error bars represent the standard deviation.

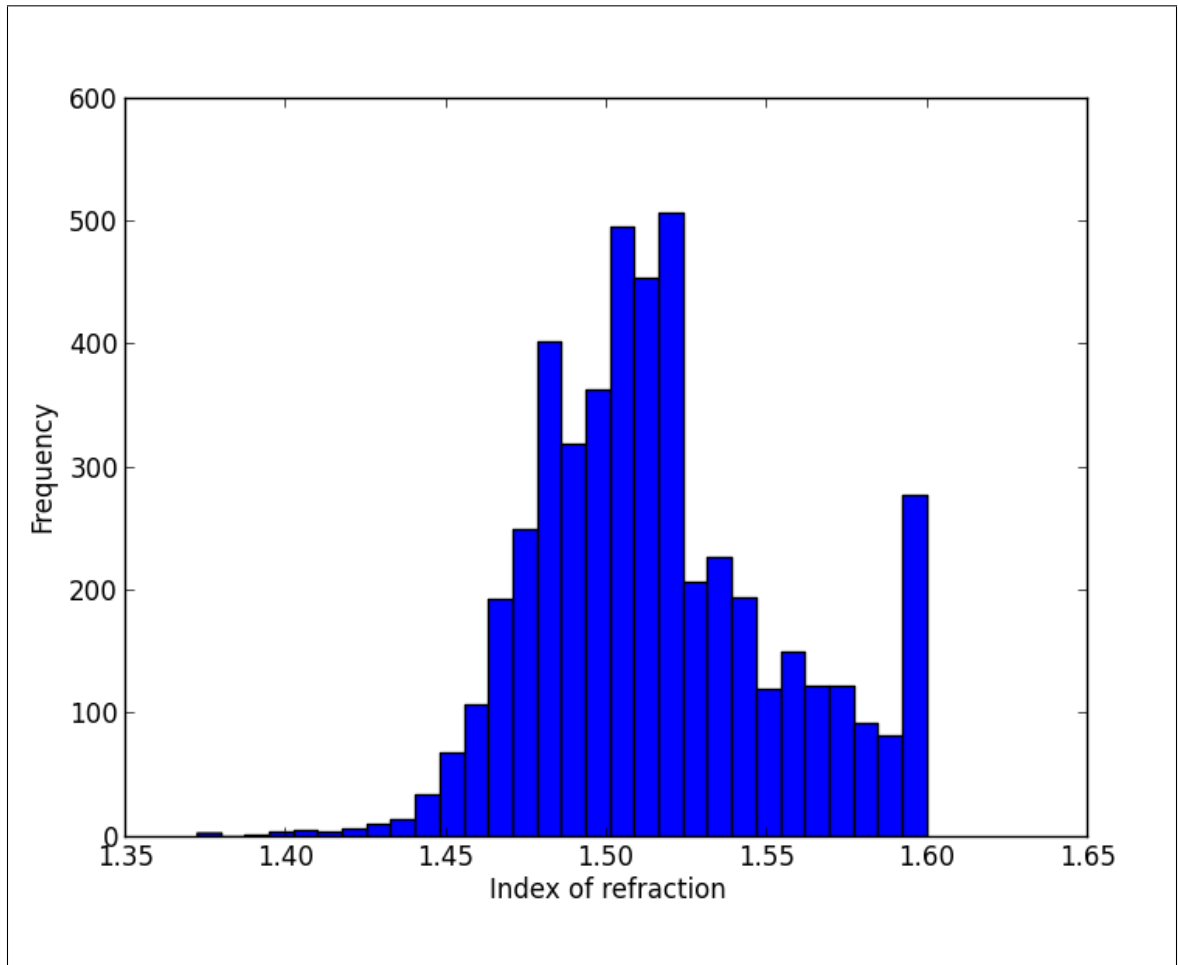


Figure 3.30: Histogram of all the AERONET available index of refraction measurements taken from Solar Village from February 1999 to December 2012.

3.5.3 Site: Mongu

Mongu is located in Zambia, Africa and it is known as a location of biomass aerosol. In this section, we present the same sort of analysis as in the previous sections for urban-industrial and dust aerosols. Figure 3.31 shows the calculated and AERONET derived VCD (bottom panel) and the corresponding values of χ^2 (top panel). We find that the biomass aerosol's DLP is in many respects quite similar to that of urban-industrial. Note that unlike Solar Village, the fine mode is clearly visible. However, the VCD has the general appearance of that of GSFC. Figure 3.32 gives the surface plot for 60 randomly selected PSD's (top panel) and the average DLP with its corresponding standard deviation (bottom panel). It should be noted that the DLP is quite similar to the DLP for the urban-industrial site shown in Figure 3.26. However, the histogram of the index of refraction displayed in Figure 3.33 is quite different from the histogram of the index of refraction of the urban industrial site shown in Figure 3.27. In addition, this figure displays the χ^2 value calculated for all the measurements of VCD from AERONET that also included a measurement of index of refraction. We have selected 60 VCD's at random and calculated the DLP which is displayed in Figure 3.32 both as a surface and as an average. For completeness, Figure 3.33 presents a histogram of all values of index of refraction found in the Mongu data set.

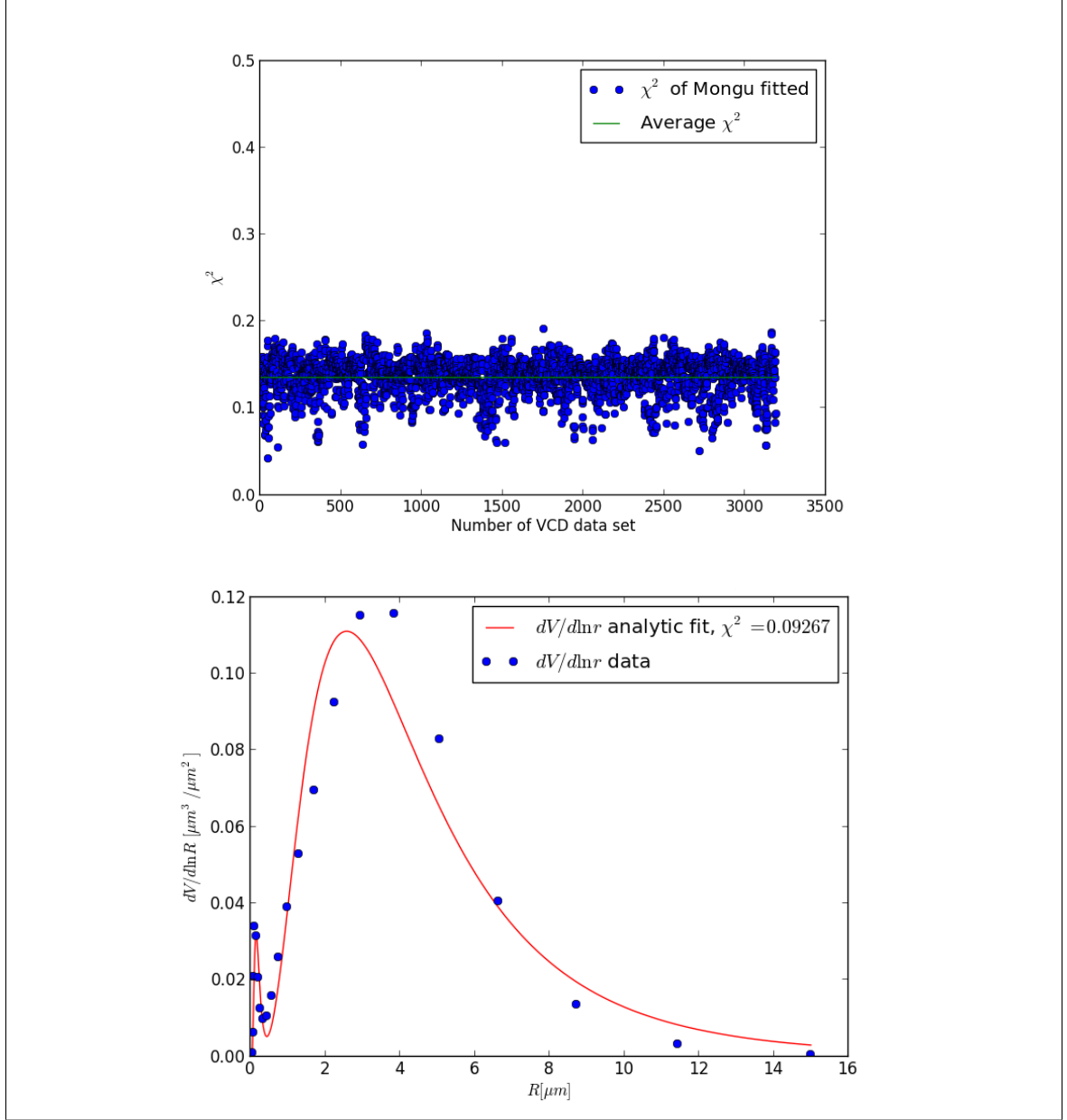


Figure 3.31: Top: all the curve-fitted VCD's from Mongu whose index of refraction was given in the data set have been evaluated by equation (3.14). The χ^2 values of this data set have been plotted as a scatter figure and its average value is displayed as a solid line. Bottom: a sample of Mongu's VCD data fitted by equation (3.11).

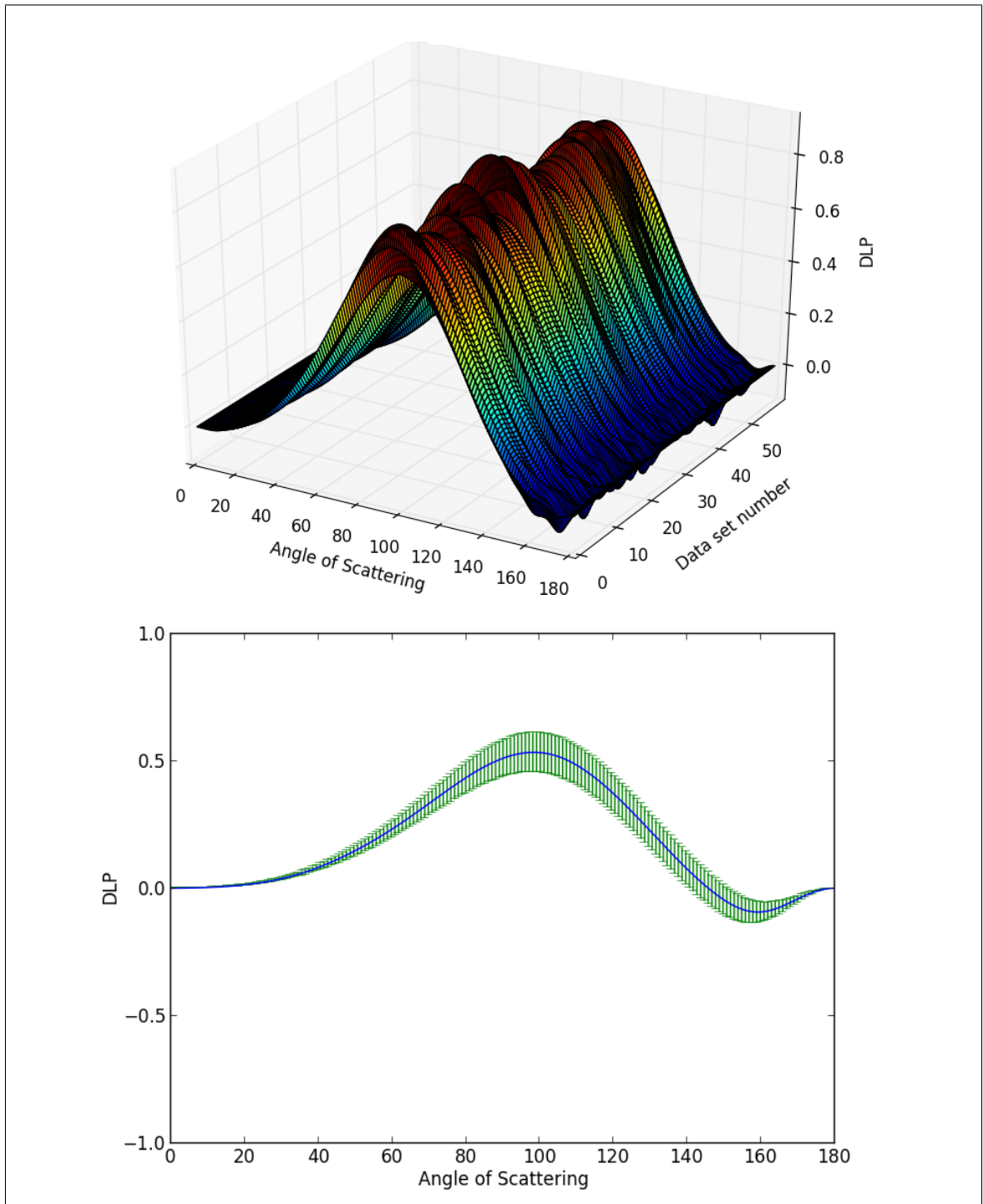


Figure 3.32: Top: overview of sixty Monte-Carlo selected PSD whose DLP has been calculated. The index of refraction was given by AERONET. Bottom: average DLP for all sixty selected PSD's. The error bars represent the standard deviation.

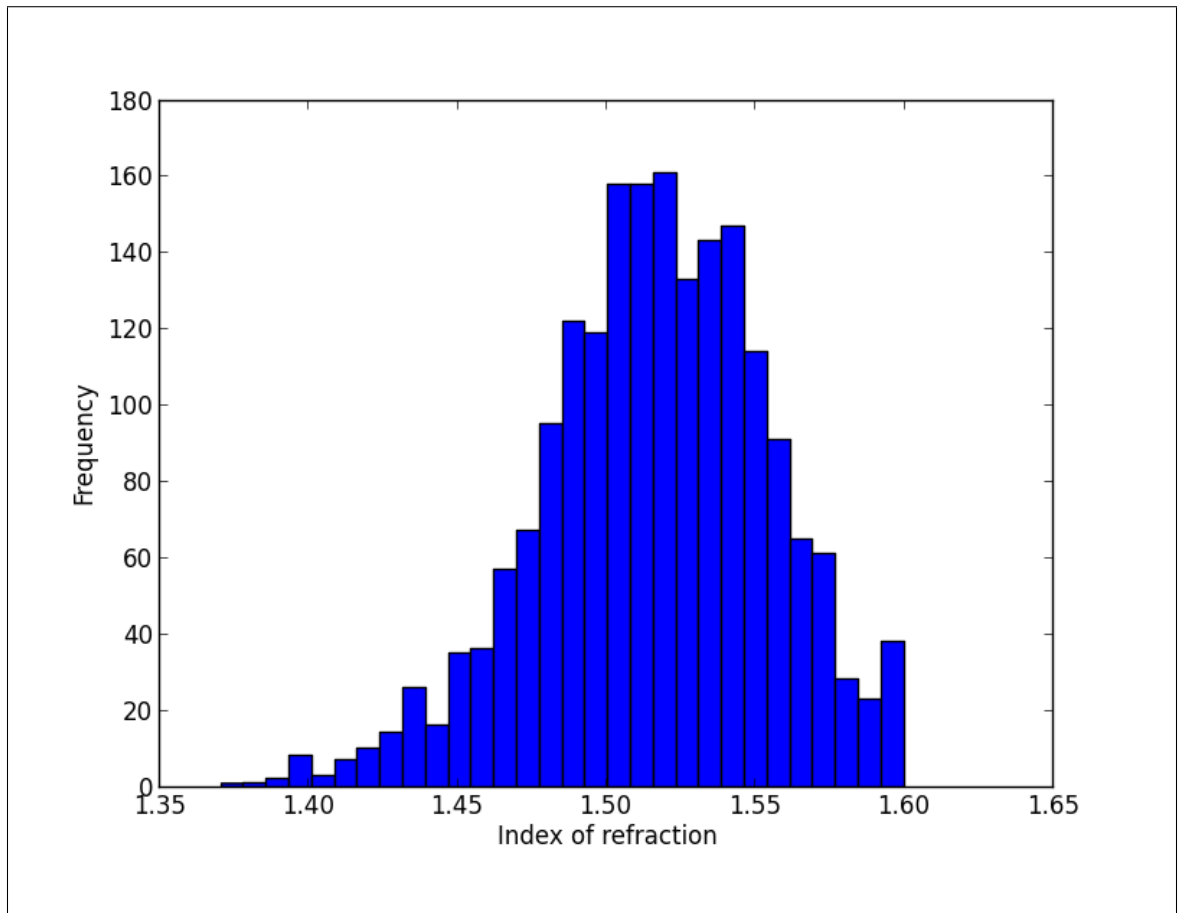


Figure 3.33: Histogram of all the AERONET available index of refraction measurements taken from Mongu from June 1995 to December 2009.

3.5.4 Site: Beijing

Beijing, China is a site where one usually finds mixed aerosols. In analogy to the analysis presented in the preceding sections, an illustration of a curve-fitted VCD is displayed in Figure 3.34. The illustration also includes a scatter plot of all VCD's from this site which also had a measurement of index of refraction. We selected 60 VCD's at random and calculated the DLP of each sample. The DLP of all 60 samples is displayed in Figure 3.35 both as a surface plot and as an average. As a final element of analysis, we display a histogram of all the index of refraction measurements found in this site in Figure 3.36.

The VCD plot is similar to that of Mongu. The DLP plot has the same shape as that of Mongu but the peak is at a higher value. Finally, the histogram of the index of refraction is similar in both cases.

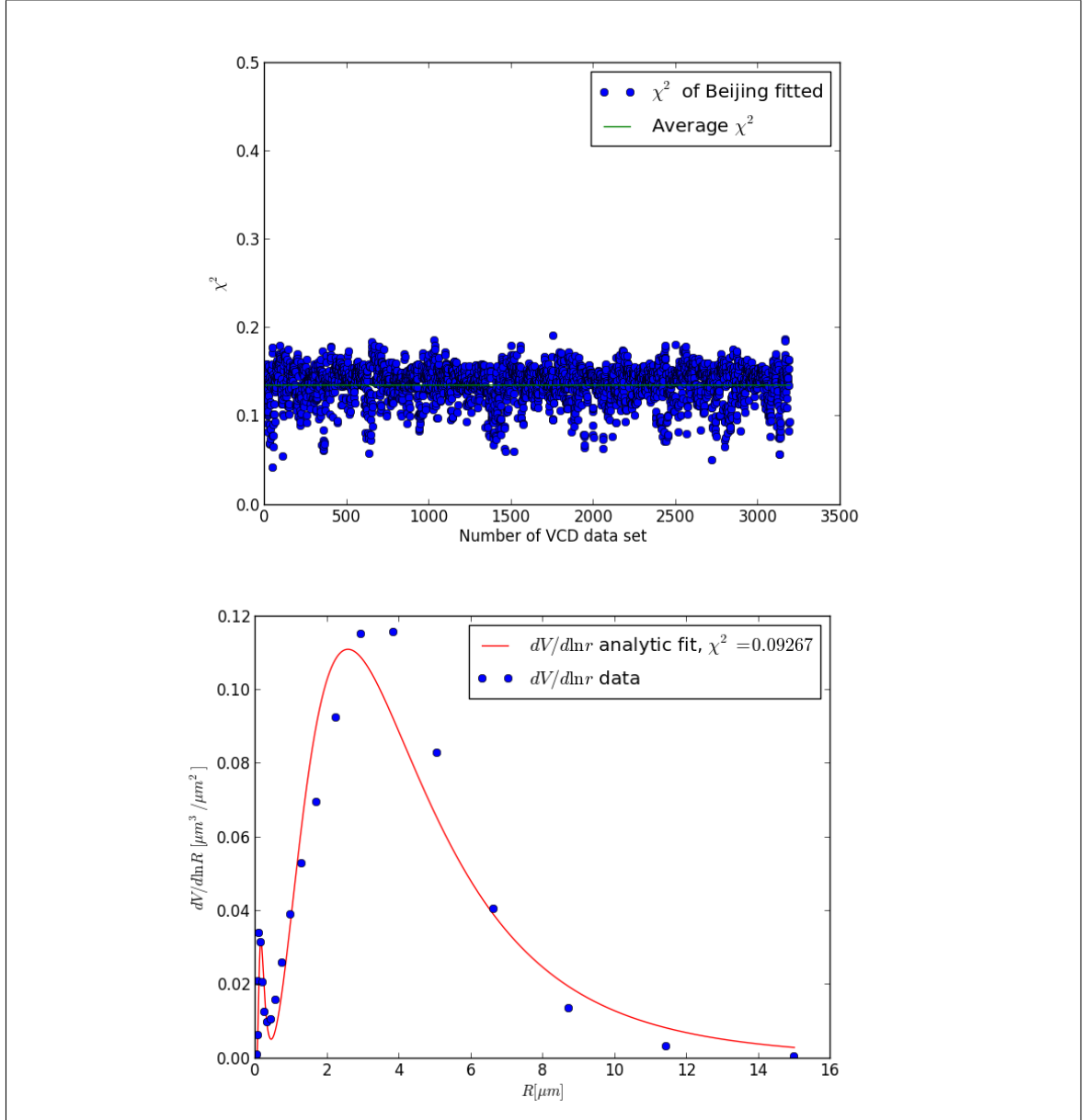


Figure 3.34: Top: all fitted VCD's from Beijing whose index of refraction was retrieved were evaluated by equation (3.14). The χ^2 value of all data set has been plotted and its average value is displayed as a solid line. Bottom: sample of a Beijing's VCD fitted by equation (3.11).

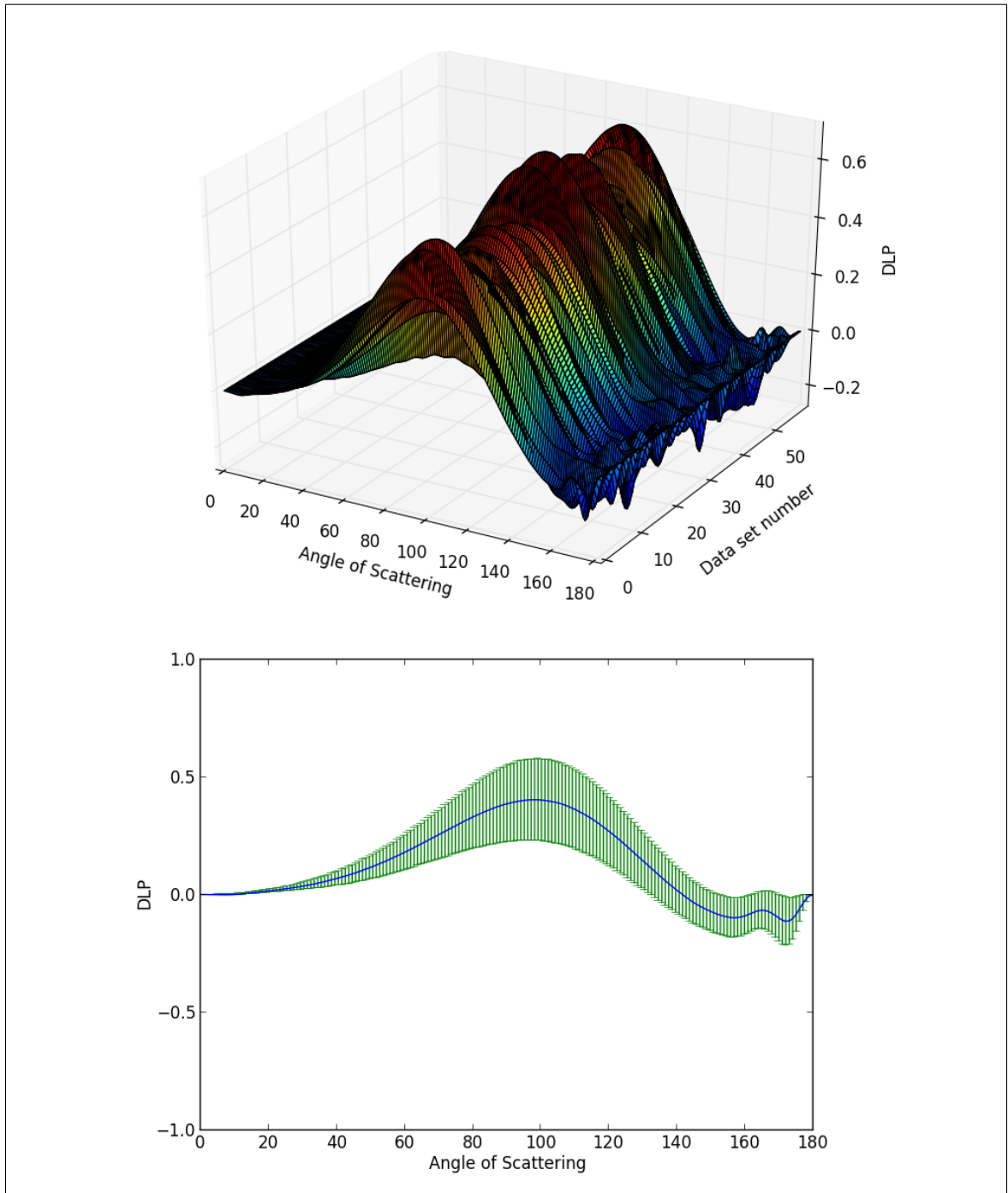


Figure 3.35: Top: overview of sixty randomly selected PSD's from Beijing. The index of refraction of each VCD was included in the data and the DLP has been calculated. Bottom: average DLP for all sixty selected VCD's. The error bars represent the standard deviation.

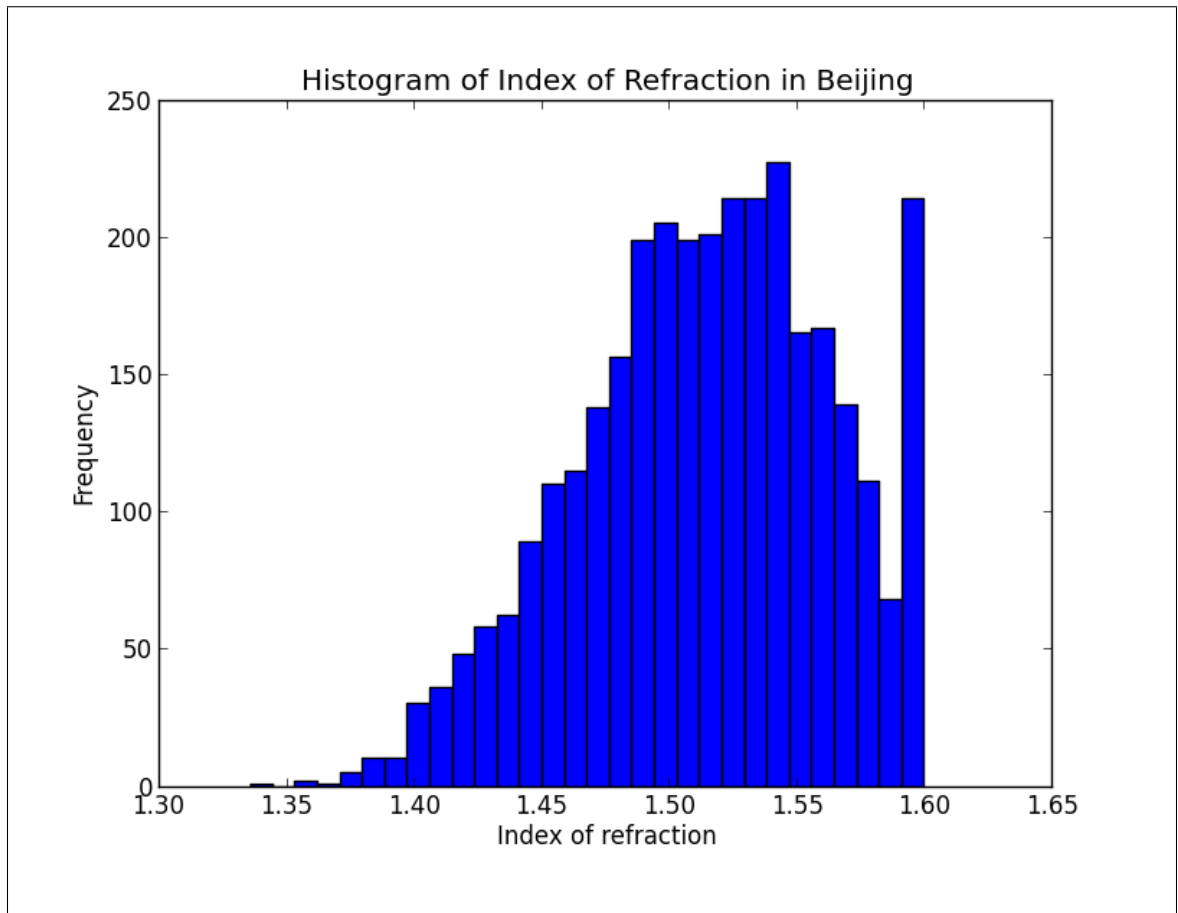


Figure 3.36: Histogram of all the AERONET available index of refraction measurements taken from Beijing from March 2001 to August 2012.

3.5.5 All Combined

Figure 3.37 summarizes the analysis of the DLP versus angle of scattering for all four sites: GSFC, Mongu, Solar Village and Beijing. Each site corresponds to a particular type of aerosol, urban-industrial, biomass, dust and mixed aerosol respectively. The figure shows that all four curves reach a maximum at the same scattering angle, a little less than 100° . The curve for urban-industrial aerosol (GSFC) is the highest and the curve for dust (Solar Village) is the lowest. The dust and the mixed aerosol (Beijing) show a small secondary peak at somewhat less than 170° and a small dip at about 175° . Overall, however, the four curves have similar shapes suggesting would be difficult to use the shape of the DLP curves as a technique for distinguishing between the four aerosol types.

3.6 Sensitivity of the DLP to the PSD and the Index of Refraction

In this section, we explore the sensitivity of the DLP to changes in the parameters of the particle size distribution (PSD) and the index of refraction. We assume a bi-modal volume concentration distribution (VCD) as described by equation (3.11). We did not carry out an analysis of the effect of changes in the standard deviation σ_f and σ_c . The DLP is calculated in two ways. First, the the mean fine radius and the mean coarse radius are changed one at a time while keeping the other fixed. Second, the mean fine radius and the mean coarse radius are fixed while changing the index of refraction. As mentioned in section 3.2, the VCD can then be converted into a PSD by using equation (3.7). Furthermore, the PSD allows us to calculate the DLP by applying equation (2.62).

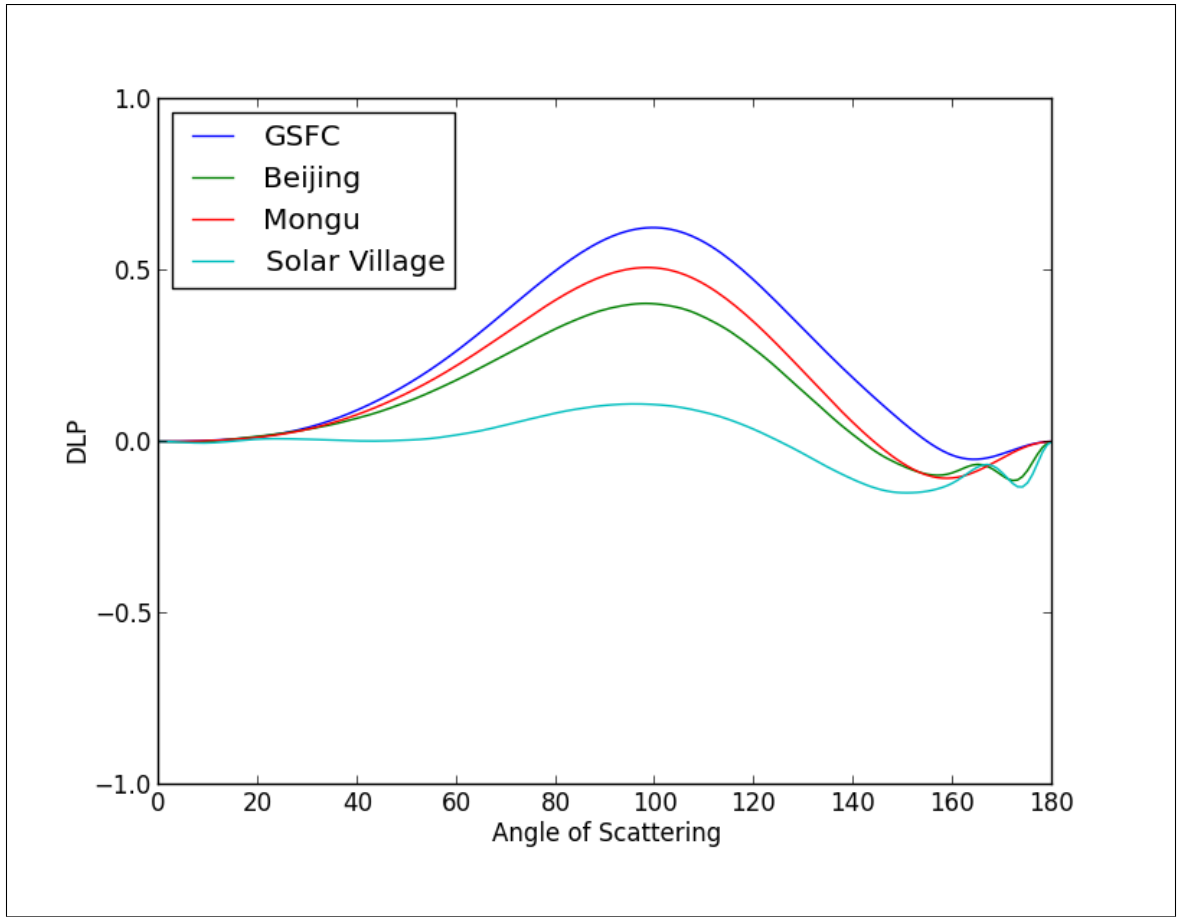


Figure 3.37: DLP for all four sites which are considered to be composed of different types of aerosols.

3.6.1 Effect on DLP of Changing the Fine Median Radius of the VCD

Recall that the VCD is given by equation (3.5), which we curve-fit to a bi-modal log-normal distribution by using equation (3.11). In this part of our analysis, the solar angle is left fixed at 65 degrees. This angle was selected because extensive studying of AERONET data sets revealed that histograms of DLP measurements from numerous sites peaked near this value. The two panels of Figure 3.38 are examples of the solar angle histograms at Barcelona and Beijing. In addition, the coarse median radius was fixed at $2.46 \mu m$ because histograms of this

parameter peaked near this value (for example, see Figure 3.39). Keeping the index of refraction fixed at $m = 1.44$ (the average index of refraction of Barcelona), we varied the range of fine median radii from $0.1 \mu m$ to $0.25 \mu m$. Changing R_f produced a change in the maximum value of DLP from 0.8 to 0.4, as can be appreciated from the surface plot in Figure 3.40.

3.6.2 Effect on DLP of Changing the Coarse Mean Radius of VCD

In order to study the effect of changing the coarse median radius, we kept the fine median radius constant at $R_f = 0.18 \mu m$. The solar angle was maintained at 65° and the index of refraction remained constant at $m = 1.44$. Figure 3.41 reveals that the maximum DLP varies from approximately 0.35 to nearly 0.58 for different values of median coarse radii ranging from $1.5 \mu m$ to $3.0 \mu m$.

3.6.3 Effect on DLP of Changing the Index of Refraction

In this section, the median fine and coarse radii have been fixed to $R_f = 0.18 \mu m$ and $R_c = 2.46 \mu m$. The solar angle is still 65 degrees and the index of refraction is varied in the range $1.30 < m < 1.70$ corresponding to typical ranges of the index of refraction of aerosols. The variation of the maximum value of the DLP decreases with increasing m as shown in Figure 3.42.

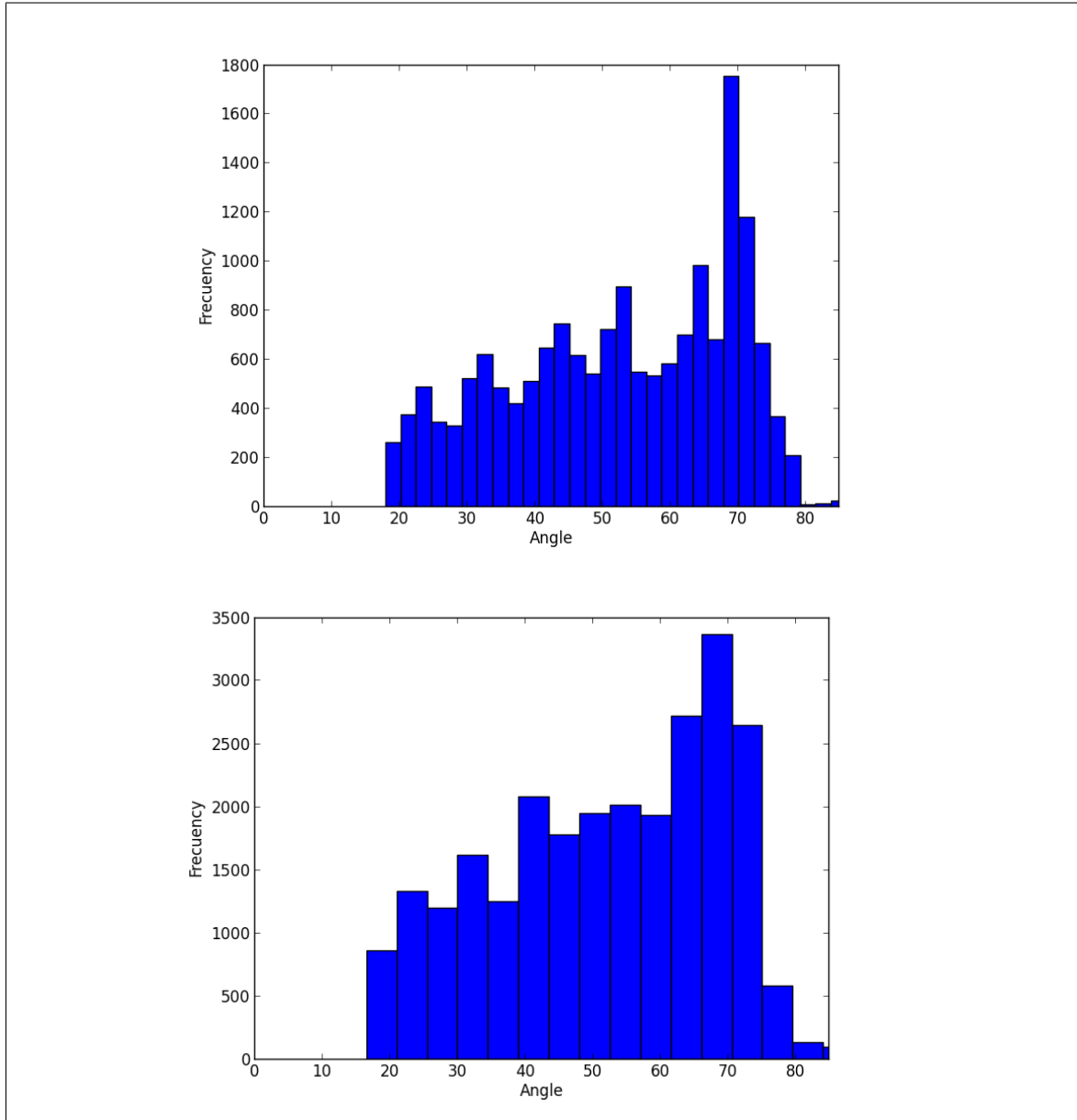


Figure 3.38: Top: histogram of solar zenith angle for all AERONET polarization measurements taken at Barcelona from December 2004 to April 2014. Bottom: histogram of solar zenith angle for Beijing from April 2002 to March 2014.

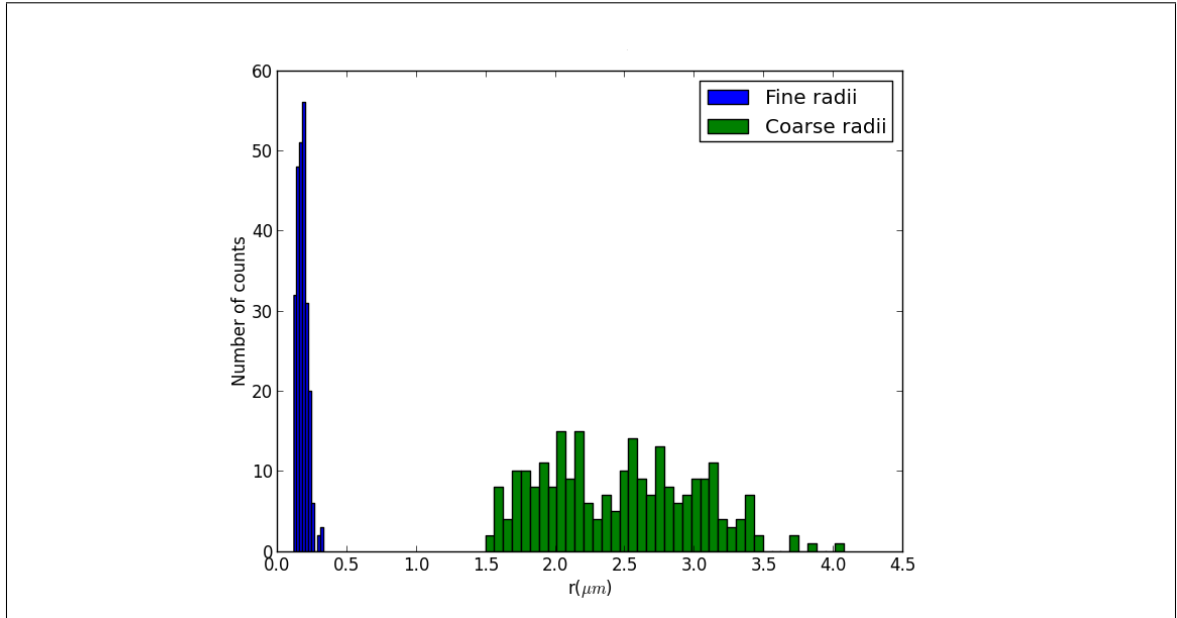


Figure 3.39: Illustration of the distribution of fine and coarse mean radii for the AERONET measured VCD's of Barcelona from 2004 to 2014

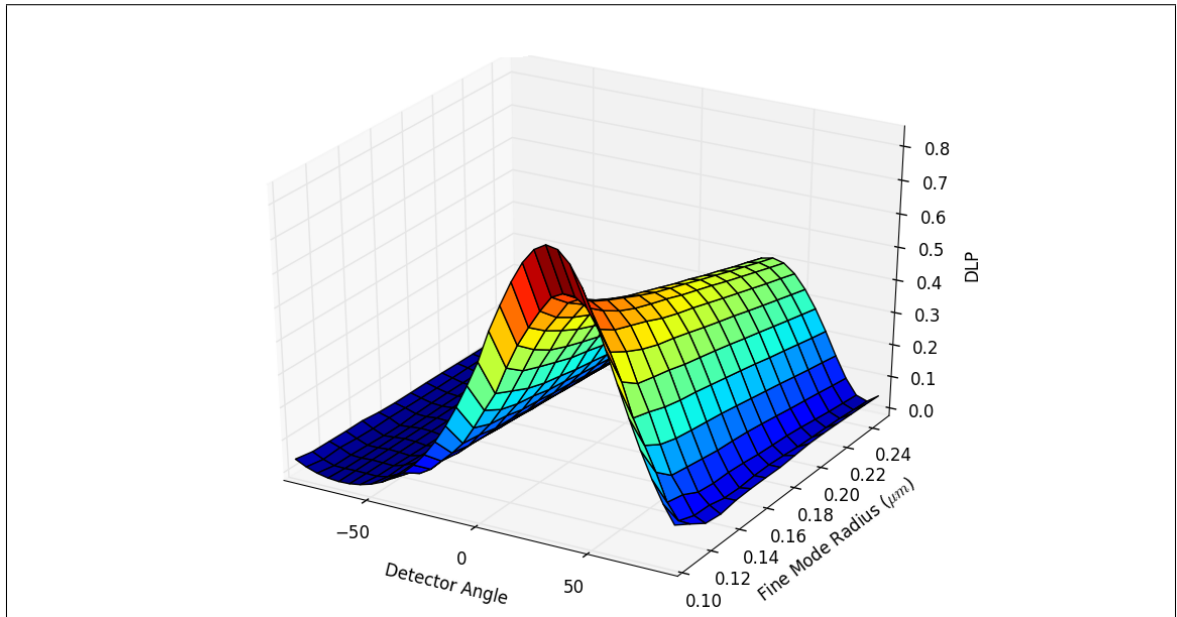


Figure 3.40: Variation in calculated polarization for the fixed parameters: $m = 1.44$, $R_c = 2.46\mu m$ and $\alpha = 65^\circ$. The mean fine mode radius R_f is allowed to change from $0.1\mu m$ to $0.25\mu m$. It is observed that the maximum DLP decreases from 0.8 to 0.4.

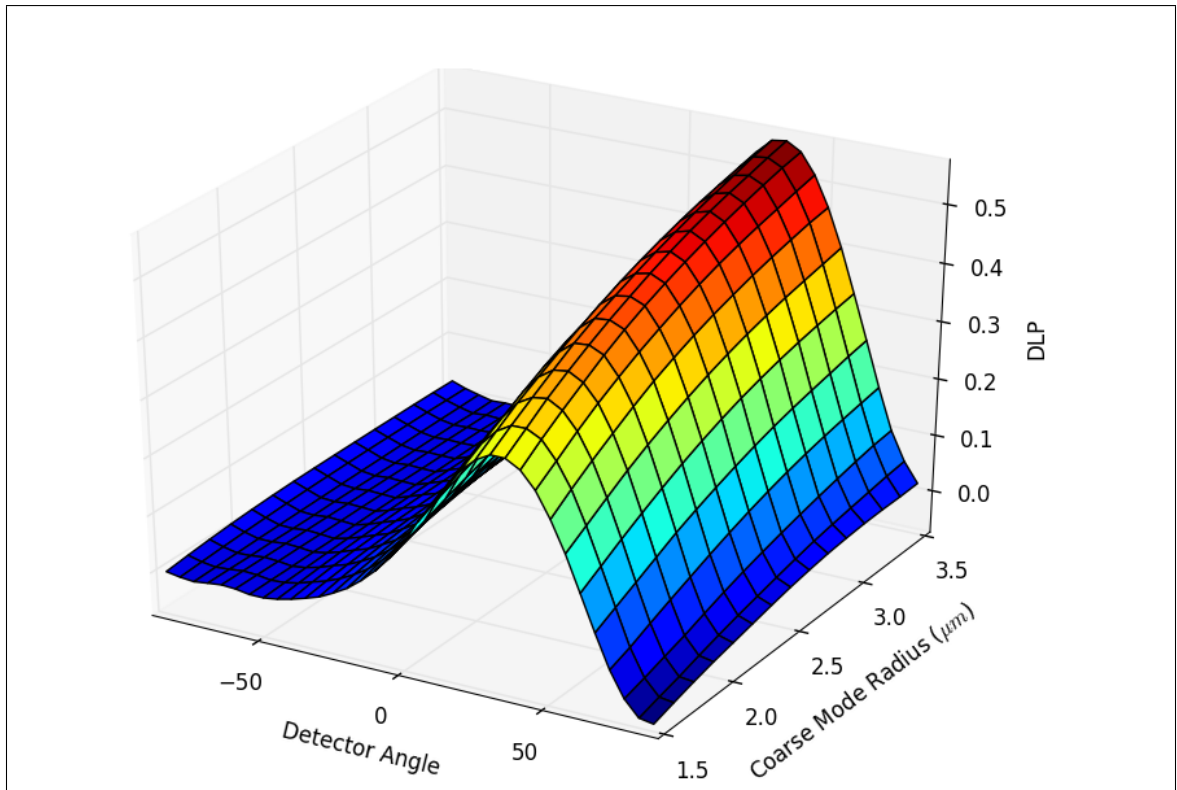


Figure 3.41: Variations in predicted DLP for fixed values of fine mean radius $R_f = 0.18\mu m$, index of refraction $m = 1.44$ and solar angle $\alpha = 65^\circ$. The mean coarse mode radius R_c is changed from $1.5\mu m$ to $3.5\mu m$.

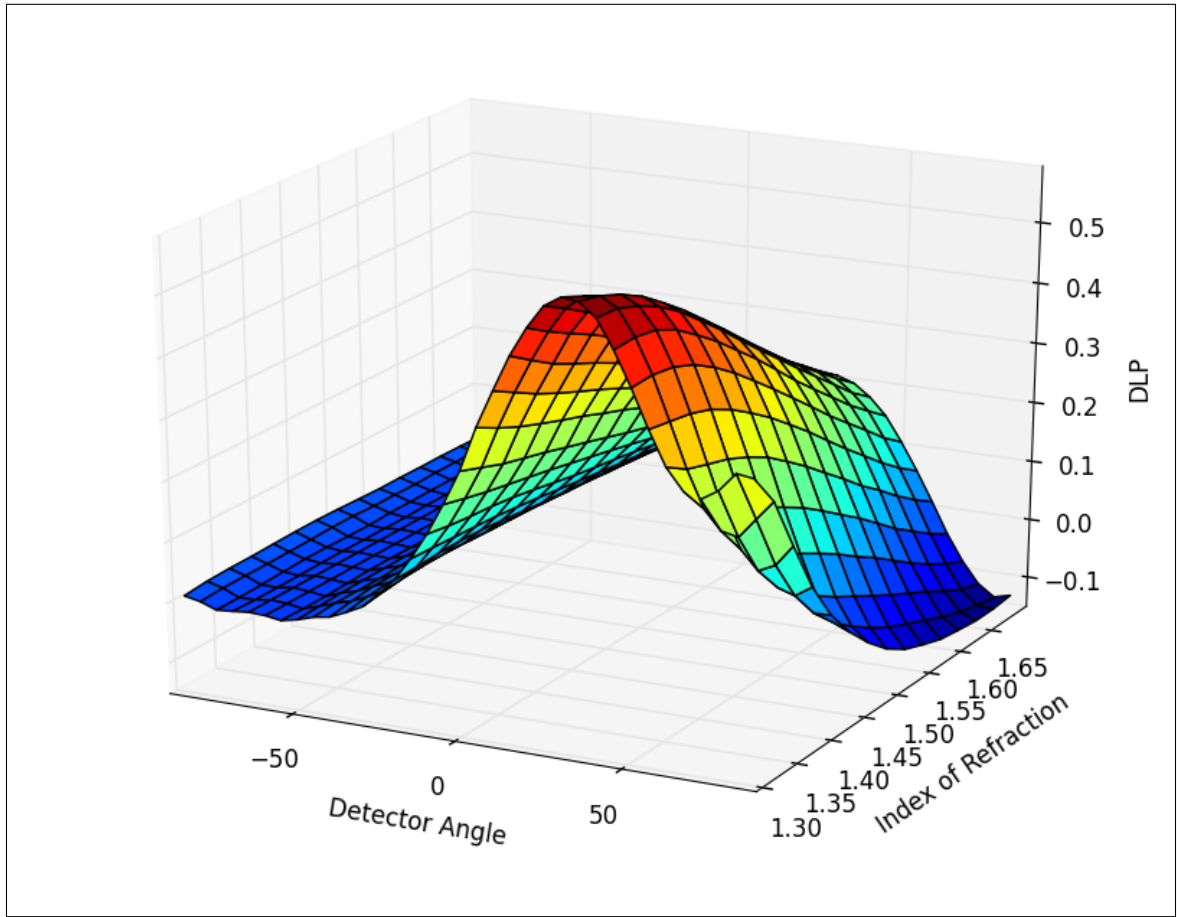


Figure 3.42: DLP for a range of values of index of refraction between $1.3 < m < 1.7$. The mean fine and coarse radii have been fixed to $R_f = 0.18\mu m$ and $R_c = 2.46\mu m$ respectively. It can be seen that the maximum DLP decreases with increasing index of refraction.

CHAPTER 4

CONCLUSIONS

In this thesis, we explored the degree of linear polarization as a parameter for distinguishing different aerosols types. We expected that distinct types of aerosols would be distinguishable by their polarization properties. However, within the limitations of this study, it was difficult to find strong differences between the DLP of the various aerosol types.

In order to develop a comprehensive theoretical framework to calculate the DLP, a brief introduction to the Jones vectors and the Stokes parameters was presented in section 2.1. In section 2.2, a far-field treatment of aerosol scattering simplified the mathematical model and introduced the complex phase function (CPF) which depends on the scattering amplitude. Then, the CPF was obtained by approximating the aerosol particles as spheres and using Mie scattering theory. To find the CPF for light scattering from many particles, section 2.2.5 shows how the CPF for a distribution can be obtained by integrating over all the available particle radii using a particle size distribution. Finally, an expression for DLP as a function of the scattering angle was given by equation (2.62).

In the final stage of this work, section 3 starts by presenting a validation of the numerical code developed to obtain the DLP. The verification consisted of comparing the results of this thesis with some of the work of Hansen and Travis (1974) and Hansen and Hovenier (1974). Successful duplication of such analyses gave us confidence to calculate the DLP for particle size distributions obtained from measurements in the Earth's atmosphere by polarizing sun photometers. In section

3.3, we discussed how the process of calculating the DLP was somewhat complex because the numerical integration of equation (2.60) and (2.61) required a quasi-continuous size distribution. As a result, the volume concentration distribution (VCD) from AERONET needed to be curve-fit to an analytic function and converted to a particle size distribution (PSD). The VCD was curve-fit to a bi-modal log-normal distribution by using equation (3.11).

In order to compare theory with experiment, in section 3.4, actual data of DLP taken by AERONET was compared against numerical calculations. The measurements of DLP are taken on a plane that contains the zenith, the position of the sun and the detector. To account for this geometry, it was necessary to calculate the angle of scattering from equation (3.12). Our calculations were successful in replicating actual polarized principal plane measurements of DLP. A few illustrations of these results are displayed in sections 3.4.2 to 3.4.5.

Section 3.5 analyzes theoretically the DLP as a function of all scattering angles from 0 to 180 degrees at four sites whose atmospheres are known to be frequently composed of urban-industrial, dust, biomass, and mixed aerosols. Figure 3.37 is a summary of such an analysis and permits one to visualize distinctions in DLP for these four types of aerosols. The results do not show clear distinctions of the DLP curves for the different aerosol types.

Finally, section 3.6 explores the sensitivity of the DLP to changes in the parameters of the VCD. The median fine radius R_f , the median coarse radius R_c , and the index of refraction are changed one at a time while keeping the position of the sun fixed at 65 degrees. The study shows that the DLP is somewhat dependent on R_f and R_c within the ranges $0.1\mu m < R_f < 0.24\mu m$ and $1.5\mu m < R_c < 3.5\mu m$. If the parameter R_f increases, the maximum DLP decreases from about 0.9 to 0.4. If R_c is changed, the DLP increases from about 0.35 to 0.58, and if the index of

refraction is changed the DLP decreases from 0.7 to 0.2.

4.1 Final Comment

In closing, considering the “big picture,” we can appreciate better the motivation for this thesis. Monitoring aerosols carefully is urgent since they are a significant factor in radiation transfer affecting global climate. Given the continuous disposal of massive amounts of anthropogenic aerosols in the atmosphere during the past few decades, it is important to understand their atmospheric effects.

Preventive action taken well in advance can prevent global catastrophes and save millions of lives. This last statement might sound like a hyperbole to some, but the fact is that atmospheric global catastrophes have already been avoided. For example, in the nineties, Nobel laureate F. S. Rowland postulated that chlorofluorocarbons contributed significantly to ozone layer depletion (Rowland, 1990). His findings led to the Montreal protocol, a treaty where world leaders took action to legislate the prohibition of production of chlorofluorocarbons. By now, some of the most important environmental agencies of the world recognize the Montreal protocol as a “landmark agreement” that prevented the proliferation of substances that could affect radiative forcing and global climate (Velders et al., 2007). In the context of monitoring substances that could have climate forcing effects, the importance of aerosol identification can not be understated. Every method of aerosol discrimination yields important clues to the identity of aerosols in our atmosphere. The methods of aerosol characterization presented in this thesis suggest an alternative method for determining aerosol properties in large scale surveys by satellites or photometers.

BIBLIOGRAPHY

- Anderson, T. L., R. J. Charlson, S. E. Schwartz, R. Knutti, O. Boucher, H. Rodhe, and J. Heintzenberg (2003). Climate forcing by aerosols—a hazy picture. *Science* 300, 1103.
- Bickel, W. S. and W. M. Bailey (1985). Stokes vectors, mueller matrices, and polarized scattered light. *Am.J.Phys.* 53, 468–478.
- Bohren, C. F. and D. R. Huffman (2008). *Absorption and scattering of light by small particles*. John Wiley & Sons, 544 pp.
- Burton, S., R. Ferrare, C. Hostetler, J. Hair, R. Rogers, M. Obland, C. Butler, A. Cook, D. Harper, and K. Froyd (2012). Aerosol classification using airborne high spectral resolution lidar measurements—methodology and examples. *Atmos. Meas. Tech.* 5, 73–98.
- Charlson, R. J., S. E. Schwartz, J. M. Hales, R. D. Cess, J. A. Coakley, J. E. Hansen, and D. J. Hofmann (1992). Climate forcing by anthropogenic aerosols. *Science* 255, 423–430.
- Cox, P. M., R. A. Betts, C. D. Jones, S. A. Spall, and I. J. Totterdell (2000). Acceleration of global warming due to carbon-cycle feedbacks in a coupled climate model. *Nature* 408, 184–187.
- Dallavalle, J., C. Orr, and H. Blocker (1951). Fitting bimodal particle size distribution curves. *Ind. Eng. Chem.* 43, 1377–1380.
- Dubovik, O. and M. D. King (2000). A flexible inversion algorithm for retrieval of aerosol optical properties from sun and sky radiance measurements. *J. Geoph. Res. Atm.* 105(D16), 20673–20696.
- Gillespie, P. (1992). An analytic phase function for cylindrical particles. *D.T.I.C.* (ASL-TR-0318), 46 pp.
- Gobbi, G. P., Y. J. Kaufman, I. Koren, and T. F. Eck (2007). Classification of aerosol properties derived from AERONET direct sun data. *Atmos. Chem. Phys.*, 453–458.
- Hamill, P. J., M. Giordano, C. Ward, D. Giles, and B. Holben (2014). An AERONET-based global classification using the mahalanobis distance. *In Preparation*.

- Hansen, J., L. Nazarenko, R. Ruedy, M. Sato, J. Willis, A. Del Genio, D. Koch, A. Lacis, K. Lo, S. Menon, et al. (2005). Earth's energy imbalance: Confirmation and implications. *Science* 308, 1431–1435.
- Hansen, J. E. (1971). Multiple scattering of polarized light in planetary atmospheres. Part I. The doubling method. *J. Atmos. Sci.* 28, 120–125.
- Hansen, J. E. and J. Hovenier (1974). Interpretation of the polarization of venus. *J. Atmos. Sci.* 31, 1137–1160.
- Hansen, J. E. and L. D. Travis (1974). Light scattering in planetary atmospheres. *Space Science Reviews* 16, 527–610.
- Holben, B., T. Eck, I. Slutsker, D. Tanre, J. Buis, A. Setzer, E. Vermote, J. Reagan, Y. Kaufman, T. Nakajima, et al. (1998). AERONET, a federated instrument network and data archive for aerosol characterization. *Rem. Sensing of Env.* 66, 1–16.
- Jackson, J. D. (1998). *Classical electrodynamics, 3rd Edition*, Volume 1. John Wiley and Sons, pp. 832.
- Jones, R. C. (1941). A new calculus for the treatment of optical systems. *JOSA* 31, 488–493.
- Kaiser, H. (2012). bhmie: Python translation of mie scattering code in fortran. <http://code.google.com/p/scatterlib/wiki/Spheres>.
- Mischenko, M., L. Travis, and A. Lacis (1991). *Scattering, Absorption and Emission of Light by Small Particles*. Cambridge University Press, 462 pp.
- Mishchenko, M. I., B. Cairns, J. E. Hansen, L. D. Travis, R. Burg, Y. J. Kaufman, J. Vanderlei Martins, and E. P. Shettle (2004). Monitoring of aerosol forcing of climate from space: analysis of measurement requirements. *J.Q.S.R.T.* 88, 149–161.
- Mishchenko, M. I. and L. D. Travis (1994). Light scattering by polydisperse, rotationally symmetric nonspherical particles: Linear polarization. *J.Q.S.R.T.* 51, 759–778.
- Omar, A. H., D. M. Winker, C. Kittaka, M. A. Vaughan, Z. Liu, Y. Hu, C. R. Trepte, R. R. Rogers, R. A. Ferrare, K.-P. Lee, et al. (2009). The CALIPSO automated aerosol classification and lidar ratio selection algorithm. *J. Atmos. Ocean. Tech.* 26, 1994–2014.
- Pedrotti, F. L., L. M. Pedrotti, and L. S. Pedrotti (1993). *Introduction to optics, 3rd edition*, Volume 2. Prentice-Hall Englewood Cliffs, 656 pp.

- Rowland, F. S. (1990). Stratospheric ozone depletion by chlorofluorocarbons. *Ambio* 19, 281–292.
- Schwartz, S. E. and M. O. Andreae (1996). Uncertainty in climate change caused by aerosols. *Science* 272, 1121–1122.
- Tomasko, M. G. and P. H. Smith (1982). Photometry and polarimetry of titan: Pioneer 11 observations and their implications for aerosol properties. *Icarus* 51, 65–95.
- van de Hulst, H. C. (2012). *Light scattering by small particles*. Dover Publications, 470 pp.
- Velders, G. J., S. O. Andersen, J. S. Daniel, D. W. Fahey, and M. McFarland (2007). The importance of the montreal protocol in protecting climate. *Proc. Nat. Acad. Sci.* 104, 4814–4819.
- West, R. A., L. R. Doose, A. M. Eibl, M. G. Tomasko, and M. I. Mishchenko (1997). Laboratory measurements of mineral dust scattering phase function and linear polarization. *J. Geophys. Res.: Atmos.* 102(D14), 16871–16881.
- Zender, C. (2008). Particle size distributions: theory and application to aerosols, clouds, and soils. <http://dust.ess.uci.edu/facts/psd/psd.pdf>.

APPENDIX A

PYTHON SUBROUTINE TO CALCULATE THE DEGREE OF POLARIZATION

```

from linpoltools import *
import bhmie

#inputs: x_range: the range of size parameters
        #nx: the number distribution for each x in x_range
        #n: the index of refraction of the distribution
        #nang: the number of angles to calculate

#outputs:
        #LP.real: the degree of polarization for all angles from
                #0 to 180 for the number of angles nang
        #theta: an array from 0 to 180 in the same size as LP.real
def linpol_optimized(x_range, nx, n, nang):
    s1_col = []
    s2_col = []
    i = 0
    nmax = nx.max()
    index_max = nx.argmax()

    for x_i in x_range:
        if 1000000*nx[i] > nmax or i < index_max:
            s1, s2, qext, qscat, qback, gasym = bhmie(x_i, n, nang)

```

```

        s1_sq = s1*conjugate(s1)
        s2_sq = s2*conjugate(s2)
        s1_w = nx[i]*s1_sq
        s2_w = nx[i]*s2_sq
        s1_col.append(s1_w)
        s2_col.append(s2_w)
        i=i+1
s1_col, s2_col = array(s1_col), array(s2_col)
S1 = []
S2 = []

for column in s1_col.T:
    s1_theta = int_trapezoid(column.real, x_range)
    S1.append(s1_theta)
for column in s2_col.T:
    s2_theta = int_trapezoid(column.real, x_range)
    S2.append(s2_theta)

S1, S2 = array(S1), array(S2)
P11 = S2+S1
P12 = S2-S1
LP = -P12/P11
theta = linspace(0, 180, len(LP))
return LP.real, theta

```

APPENDIX B

PYTHON CODE USED TO IMPLEMENT MIE SCATTERING

```

from numpy import *

def bhmie(x,refrel,nang):
# This file is converted from mie.m, see http://atol.ucsd.edu/scatlib/in
# Bohren and Huffman originally published the code in their book on light scattering
# Calculation based on Mie scattering theory
# input:
#       x       - size parameter =  $k \cdot \text{radius} = 2\pi / \text{lambda} * \text{radius}$ 
#               (lambda is the wavelength in the medium around the sphere)
#       refrel  - refraction index (n in complex form for example:
#               1.5+0.02*i;
#       nang    - number of angles for S1 and S2 function in range from 0 to 2pi
# output:
#       S1, S2 - funtion which correspond to the (complex) phase functions
#       Qext   - extinction efficiency
#       Qsca   - scattering efficiency
#       Qback  - backscatter efficiency
#       gsca   - asymmetry parameter

```

```
nmxx=150000
```

```
s1_1=zeros(nang,dtype=complex128)
```

```
s1_2=zeros(nang,dtype=complex128)
```

```
s2_1=zeros(nang,dtype=complex128)
```

```
s2_2=zeros(nang,dtype=complex128)
```

```
pi=zeros(nang)
```

```
tau=zeros(nang)
```

```
if (nang > 1000):
```

```
    print ('error: nang > mxnang=1000 in bhmie')
```

```
    return
```

```
# Require NANG>1 in order to calculate scattering intensities
```

```
if (nang < 2):
```

```
    nang = 2
```

```
pii = 4.*arctan(1.)
```

```
dx = x
```

```
drefrl = refrel
```

```
y = x*drefrl
```

```
ymod = abs(y)
```

```

#      Series expansion terminated after NSTOP terms
#      Logarithmic derivatives calculated from NMX on down

xstop = x + 4.*x**0.3333 + 2.0
nmx = max(xstop,ymod) + 15.0
nmx=fix(nmx)

# BTd experiment 91/1/15: add one more term to series and compare re
#      NMx=AMAX1(XSTOP,YMOD)+16
# test: compute 7001 wavelen>hs between .0001 and 1000 micron
# for a=1.0micron SiC grain. When NMx increased by 1, only a single
# computed number changed (out of 4*7001) and it only changed by 1/8
# conclusion: we are indeed retaining enough terms in series!
nstop = int(xstop)

if (nmx > nmxx):
    print ( "error: nmx > nmxx=%f for |m|x=%f" % ( nmxx, ymod) )
    return

dang = .5*pii/ (nang-1)

amu=arange(0.0,nang,1)
amu=cos(amu*dang)

```

```

pi0=zeros(nang)
pi1=ones(nang)

# Logarithmic derivative D(J) calculated by downward recurrence
# beginning with initial value (0.,0.) at J=NMX

nn = int(nmx)-1
d=zeros(nn+1)
for n in range(0,nn):
    en = nmx - n
    d[nn-n-1] = (en/y) - (1./ (d[nn-n]+en/y))

#*** Riccati-Bessel functions with real argument X
#    calculated by upward recurrence

psi0 = cos(dx)
psi1 = sin(dx)
chi0 = -sin(dx)
chi1 = cos(dx)
xi1 = psi1-chi1*1j
qsca = 0.
gsca = 0.
p = -1

for n in range(0,nstop):

```

```

en = n+1.0

fn = (2.*en+1.)/(en* (en+1.))

# for given N, PSI = psi_n          CHI = chi_n
#          PSI1 = psi_{n-1}        CHI1 = chi_{n-1}
#          PSI0 = psi_{n-2}        CHI0 = chi_{n-2}
# Calculate psi_n and chi_n
psi = (2.*en-1.)*psi1/dx - psi0
chi = (2.*en-1.)*chi1/dx - chi0
xi = psi-chi*lj

**** Store previous values of AN and BN for use
#   in computation of  $g=\langle \cos(\theta) \rangle$ 
if (n > 0):
    an1 = an
    bn1 = bn

**** Compute AN and BN:
an = (d[n]/drefrl+en/dx)*psi - psi1
an = an/ ((d[n]/drefrl+en/dx)*xi-xi1)
bn = (drefrl*d[n]+en/dx)*psi - psi1
bn = bn/ ((drefrl*d[n]+en/dx)*xi-xi1)

**** Augment sums for Qsca and  $g=\langle \cos(\theta) \rangle$ 
qsca += (2.*en+1.)* (abs(an)**2+abs(bn)**2)

```

```

gsca += ((2.*en+1.)/ (en* (en+1.)))*( real(an)* real(bn)+imag(an)

if (n > 0):
    gsca += ((en-1.)* (en+1.)/en)*( real(an1)* real(an)+imag(an1)

**** Now calculate scattering intensity pattern
#    First do angles from 0 to 90
pi=0+pi1      # 0+pi1 because we want a hard copy of the values
tau=en*amu*pi-(en+1.)*pi0
s1_1 += fn* (an*pi+bn*tau)
s2_1 += fn* (an*tau+bn*pi)

**** Now do angles greater than 90 using PI and TAU from
#    angles less than 90.
#    P=1 for N=1,3,...% P=-1 for N=2,4,...
#    remember that we have to reverse the order of the elements
#    of the second part of s1 and s2 after the calculation
p = -p
s1_2+= fn*p* (an*pi-bn*tau)
s2_2+= fn*p* (bn*pi-an*tau)

psi0 = psi1
psi1 = psi
chi0 = chi1
chi1 = chi

```



```

x1l = psi1-chi1*1j

**** Compute pi_n for next value of n
#   For each angle J, compute pi_n+1
#   from PI = pi_n , PI0 = pi_n-1
pi1 = ((2.*en+1.)*amu*pi- (en+1.)*pi0)/ en
pi0 = 0+pi    # 0+pi because we want a hard copy of the values

**** Have summed sufficient terms.
#   Now compute QSCA,QEXT,QBACK,and GSCA

#   we have to reverse the order of the elements of the second part
s1=concatenate((s1_1,s1_2[-2::-1]))
s2=concatenate((s2_1,s2_2[-2::-1]))
gsca = 2.*gsca/qsca
qsca = (2./ (dx*dx))*qsca
qext = (4./ (dx*dx))* real(s1[0])

# more common definition of the backscattering efficiency ,
# so that the backscattering cross section really
# has dimension of length squared
qback = 4*(abs(s1[2*nang-2])/dx)**2
#qback = ((abs(s1[2*nang-2])/dx)**2 )/pii  #old form

return s1,s2,qext,qsca,qback,gsca

```

APPENDIX C

**PYTHON SUBROUTINES USED FOR DATA ANALYSIS:
“LINPOLTOOLS.PY”**

```

def psd(r, rm, sigma):
#outputs the log-normal distribution of a given mean
#radius rm and a standard deviation sigma
    const = 1/(sqrt(2*pi)*sigma)
    psd = exp(-0.5*(log(r)-log(rm))**2/(sigma)**2)
    return const*psd

def is_number(s):
#determines whether a given set of data
#is a number or not
    try:
        float(s)
        return True
    except ValueError:
        return False

def averpoint(LP, N_desired):
#averages and array of length len(LP) into N_desired points
#returns:
    #the new array of angles
    #the averaged N_desired points

```

```

        #the standard deviation of the averaged points.
N = len(LP)
separation = N/N_desired
point = zeros(N_desired)
errbar = zeros(N_desired)
theta2 = linspace(0,180, len(point))
for n in range(N_desired):
    i = separation*n
    point[n] = average(LP[i: i + separation + 1])
    errbar[n] = LP[i:i+separation + 1].std()
return theta2, point, errbar

def int_trapezoid(fx,x):
    #outputs the integration of an array
    #given the variable x and the function fx
    N = len(fx)
    a = zeros(N-1)
    for i in range(N-1):
        dx = x[i+1]-x[i]
        a[i] = 0.5*(fx[i]+fx[i+1])*dx
    return sum(a)

def averager(a):
    #outputs the average of each column vector and its
    #standard deviation given a matrix "a"

```

```
N = len(a.T)
av = zeros(N)
err = zeros(N)
for i in range(len(a.T)):
    av[i] = a.T[i].mean()
    err[i] = a.T[i].std()
return av, err
```

APPENDIX D

PYTHON PROGRAM TO FIND AND EVALUATE COINCIDENCES

```

from pylab import *
from linpoltools import *
from datetime import datetime, date, time, timedelta
from linpol_optimized import linpol_optimized as lp
import csv

#function used to evaluate the agreement of
#calculation and measurment
def chi(Y_analytic, Y_obtained):
    CHI_tot = sum((Y_analytic-Y_obtained)**2)
    chi_red = CHI_tot/(len(Y_obtained)-1)
    return chi_red

#all databases of PSD have been standarized to have the
#name as 'site_refined.csv' for the AERONET files.
#The AERONET files have been filtered to include only those
#PSD's that do not have that index of refraction as 'N/A'

site = 'Osaka'
filename = './'+site+'/' + site.lower()+'_refined.csv'
f = open(filename)

```

```

matrix = csv.reader(f, delimiter = ',')
matrix = array(list(matrix))
psd_dates = []
dr = .01
r = arange(0.001, 15, dr)
r_data = [float(n) for n in matrix[0,62:84]]
X = 2*pi*r/.873
detect_ang = arange(-85,86,5)
chi_list = []

#The date and time of each PSD measurement is obtained
for i in range(1,len(matrix)):
    d = matrix[i,0].split('/')
    t = matrix[i,1].split(':')
    d = date(int(d[2]),int(d[0]),int(d[1]))
    t = time(int(t[0]), int(t[1]),int(t[2]))
    datepsd = datetime.combine(d,t)
    psd_dates.append(datepsd)

#All data bases have been standardized to have the
#name 'site_pol.csv' for data of DLP measurements
filename2 = './'+site+'/' + site.lower()+'_pol.csv'
g = open(filename2)
mat = csv.reader(g, delimiter = ',')

```

```

mat = array(list(mat))
pol_dates=[]

#the date and time of each DLP measurement is obtained
for j in range(1,len(mat)):
    date2 = mat[j,0].split('/')
    time2 = mat[j,1].split(':')
    date2= date(int(date2[2]),int(date2[0]),int(date2[1]))
    time2= time(int(time2[0]), int(time2[1]),int(time2[2]))
    datepol = datetime.combine(date2,time2)
    pol_dates.append(datepol)

x_data = array(mat[0,109:144])
x_fixed = zeros(len(x_data))
for k in range(len(x_data)):
    x_fixed[k] = x_data[k].split(' ')[0]

# input a psd date with index m
# attempts to find a measurement within 90 minutes of psd
for w in range(1,len(psd_dates)):
    m=w #starting index of psd measure
    n=1
    nr = matrix[m,44]
    ni = matrix[m,48]

```

```

for a_date in pol_dates:
    i = m
    j = n
    delay = psd_dates[m]-a_date
    if abs(delay) < timedelta(minutes=90):

        refr = complex(float(nr),float(ni))
        n_data = [float(k) for k in matrix[i,62:84]]
        vf = float(matrix[i,89])
        rm_f = float(matrix[i,91])
        sigma_f = float(matrix[i,92])
        vc = float(matrix[i,93])
        rm_c = float(matrix[i,95])
        sigma_c = float(matrix[i,96])
        fine = vf*psd(r,rm_f,sigma_f)
        coarse = vc*psd(r,rm_c,sigma_c)
        VCD = fine + coarse
        PSD = (3/(4*pi*r**4))*VCD

    #finds the DLP of that particular date
    #for all scattering angles
    LP = lp(X,PSD,refr,90)
    ang = range(1,180)

```



```

#constructs the DLP for the detector
#by obtaining the solar zenith angle
LP_construct = zeros(len(ang))
solang = float(mat[j,3])
scat_ang = around(detect_ang-solang)
scat_ang = [abs(int(n)) for n in scat_ang]
LP_construct = LP[0][scat_ang]
chi_red = chi(LP_construct[:, -1], lp_data)
chi_list.append(chi_red)

break

if n == len(pol_dates):
    print 'None found'
    break

n+=1

figure()
plot(range(len(chi_list)), chi_list, 'o')
title('Evaluation of Theory and Experiment by its  $\chi^2$  Value')
ylabel('$\chi^2$')
xlabel('Coincidence count')
f.close()
g.close()
show()

```